

博士學位 請求論文  
指導教授 兪 印 泰

CDF 실험에서의  
 $B(B^+ \rightarrow J/\psi\pi^+)/B(B^+ \rightarrow J/\psi K^+)$ 의 측정

Measurement of  
 $B(B^+ \rightarrow J/\psi\pi^+)/B(B^+ \rightarrow J/\psi K^+)$  at  
the Collider Detector at Fermilab

成均館大學校 大學院  
物理學科  
核 및 粒子物理學專攻  
李 載 承

博士學位 請求論文  
指導教授 俞 印 泰

CDF 실험에서의  
 $B(B^+ \rightarrow J/\psi\pi^+)/B(B^+ \rightarrow J/\psi K^+)$ 의 측정

Measurement of  
 $B(B^+ \rightarrow J/\psi\pi^+)/B(B^+ \rightarrow J/\psi K^+)$  at  
the Collider Detector at Fermilab

이 論文을 理學 博士學位請求論文으로 提出합니다

2005年 10月 日

成均館大學校 大學院

物理學科

核 및 粒子物理學專攻

李 載 承

이 論文을 李載承의 理學  
博士學位 論文으로 認定함

2005年 12月 日

審査委員長 崔 英 日 *Youngil Choi*  
審査委員 Ting Miao *Ting Miao* 11-30  
-2005  
審査委員 김 수 봉 *Kim Su Bong*  
審査委員 김 윤 배 *Kim Yun Bae*  
審査委員 유 인 태 

---

Thesis for the Degree of Doctor of Philosophy

Measurement of  
 $\mathcal{B}(B^+ \rightarrow J/\psi\pi^+)/\mathcal{B}(B^+ \rightarrow J/\psi K^+)$  at  
the Collider Detector at Fermilab

Jaison Lee

Department of Physics, Major in Particle Physics  
The Graduate School

December 2005

The Graduate School  
SungKyunKwan University

Thesis advisor  
Intae Yu

Author  
Jaison Lee

Measurement of  
 $\mathcal{B}(B^+ \rightarrow J/\psi\pi^+)/\mathcal{B}(B^+ \rightarrow J/\psi K^+)$  at  
the Collider Detector at Fermilab

Abstract

This thesis reports on a measurement of the ratio of branching fractions,  $\mathcal{B}(B^+ \rightarrow J/\psi\pi^+)/\mathcal{B}(B^+ \rightarrow J/\psi K^+)$ , where  $J/\psi \rightarrow \mu^+\mu^-$ . The data were collected by the Collider Detector at Fermilab between February 2002 and August 2003 and corresponds to an integrated luminosity of  $220 \text{ pb}^{-1}$  in  $p\bar{p}$  collisions at  $\sqrt{s} = 1.96 \text{ TeV}$ . We determine the ratio of branching fractions,

$$\frac{\mathcal{B}(B^+ \rightarrow J/\psi\pi^+)}{\mathcal{B}(B^+ \rightarrow J/\psi K^+)} = 4.86 \pm 0.82(\text{stat.}) \pm 0.14(\text{syst.})\% .$$

# Contents

<b>1</b>	<b>Introduction</b>	<b>1</b>
1.1	The effective Hamiltonian . . . . .	1
1.2	The factorization prescription . . . . .	4
1.2.1	Type-I decays . . . . .	4
1.2.2	Type-II decays . . . . .	6
1.2.3	Type-III decays . . . . .	7
1.3	Deviations from factorization . . . . .	7
1.4	Generalized factorization . . . . .	9
1.5	Generalized factorization . . . . .	10
1.5.1	Generalized factorization . . . . .	12
<b>2</b>	<b>CDF Experiment</b>	<b>17</b>
2.1	The Accelerator and Collider . . . . .	17
2.2	The CDF Detector . . . . .	19
2.2.1	Coordinate System . . . . .	20
2.2.2	Tracking System . . . . .	23
2.2.3	Muon System . . . . .	34
2.2.4	Other Systems . . . . .	40
2.2.5	General Triggering . . . . .	45
2.2.6	Dimuon Trigger . . . . .	50
2.3	Offline Data Handling . . . . .	52

---

<b>3</b>	<b>Data Sample and Signal Selection</b>	<b>55</b>
3.1	Data Sample . . . . .	56
3.2	Track Preparation . . . . .	57
3.3	Muon Preparation . . . . .	59
3.4	$J/\psi$ Reconstruction . . . . .	59
3.5	$B^+$ Reconstruction and Selection . . . . .	60
<b>4</b>	<b>Measurement of the Ratio of Branching Fractions</b>	<b>65</b>
4.1	Mass Shift Calculation . . . . .	66
4.2	Likelihood . . . . .	69
4.3	Fitting Range . . . . .	75
4.4	Fitting Results . . . . .	75
4.5	Cross Checks . . . . .	79
4.6	Likelihood including PID Information . . . . .	81
4.7	Calculation of the Relative Reconstruction Efficiency . . . . .	85
<b>5</b>	<b>Systematics</b>	<b>89</b>
5.1	Fitting Procedure . . . . .	89
5.2	Background Model for Mass Distribution . . . . .	92
5.3	Fitting Range . . . . .	93
5.4	PDF's parameterization . . . . .	93
5.5	$\epsilon_{rel}$ . . . . .	93
5.6	Systematics Summary . . . . .	94
<b>6</b>	<b>Conclusion</b>	<b>95</b>
	References . . . . .	97

# List of Figures

1.1	Tree diagram $b \rightarrow c\bar{u}d$ , with a spectator quark $\bar{d}$ , affected by gluon exchanges. . . . .	2
1.2	The tree diagram for the decay $\bar{B}^0 \rightarrow D^+\pi^-$ . . . . .	2
1.3	The tree diagram for the decay $\bar{B}^0 \rightarrow D^0\pi^0$ . . . . .	5
1.4	The tree diagram for the decay $B^- \rightarrow J/\psi\pi^-$ . . . . .	10
1.5	The gluonic penguin diagram ( $q = u, c, t$ ). . . . .	11
1.6	The electroweak penguin diagram ( $q = u, c, t$ ). . . . .	12
2.1	Cutaway view of the CDF detector. . . . .	18
2.2	Cutaway view of the CDF detector. . . . .	20
2.3	Cutaway view of the CDF detector. . . . .	21
2.4	Elevation view of the CDF detector. . . . .	22
2.5	The schematic view of the CDF tracking system. . . . .	24
2.6	The end view of the SVX system. . . . .	25
2.7	Side perspective views of $r-\phi$ side (top) and $r-z$ side (bottom) of Layer 0 ladder in the SVX system. . . . .	28
2.8	A quarter of the COT sense wires. . . . .	31
2.9	The cell layout for superlayer 2 at COT. . . . .	32
2.10	Muon coverage for Run I (left) and Run II (right). . . . .	34
2.11	The $r-\phi$ view of the CMP system looking at the end of the CDF detector. . . . .	37

2.12	The side view of the CDF showing the CMX coverage. The dark blocks spanning between $30^\circ - 40^\circ$ and $56^\circ$ are the CMX wedges. . . . .	39
2.13	The MiniSkirt portion of the CMX system. . . . .	39
2.14	A detailed section of the IMU Barrel. . . . .	40
2.15	The elevation view of the Imu Barrel (thick dark line). The Miniskirt part of the CMX is shown too. . . . .	41
2.16	The Time-of-Flight performance. . . . .	42
2.17	The cross-section of upper part of the end plug calorimeter. . . . .	44
2.18	The trigger and DAQ system functional block diagram. . . . .	47
2.19	The CDF trigger-system block diagram. . . . .	49
2.20	The block scheme of the Event Builder and Level-3 system. . . . .	51
2.21	The mass spectrum of muon pairs obtained via different triggers at CDF. The dimuon trigger used in this analysis is called "JPsi".	53
3.1	The topological $B^+ \rightarrow J/\psi K^+$ diagram of decay. . . . .	56
3.2	The invariant mass distribution of $J/\psi \rightarrow \mu^+ \mu^-$ with likelihood projection overlaid. Signal is modeled with two Gaussians and background is modeled with a 1st order polynomial function. . . . .	60
3.3	The invariant mass distributions of $M(\mu^+ \mu^- K^+)$ (top) and $M(\mu^+ \mu^- \pi^+)$ (bottom). The bottom plot is the invariant mass distribution when the third track is assumed as pion. . . . .	63
4.1	The invariant mass distributions of $B^+ \rightarrow J/\psi K^+$ (blue) and $B^+ \rightarrow J/\psi \pi^+$ (Red) when the kaon mass is assigned to the third track. These distributions are generated by Monte Carlo. . . . .	67
4.2	The distributions of mass difference, $M(\mu\mu K) - \mathcal{M}(\alpha)$ , in the cases of (a) $B^+ \rightarrow J/\psi K^+$ and (b) $B^+ \rightarrow J/\psi \pi^+$ signals which are generated by Monte Carlo. . . . .	70
4.3	The $\alpha$ distributions with the parameterizing function overlaid for (a) $B^+ \rightarrow J/\psi K^+$ and (b) $B^+ \rightarrow J/\psi \pi^+$ signals which are generated by Monte Carlo . . . . .	71

4.4	(a) The invariant mass distribution of $M(\mu\mu K)$ without $L_{xy}$ cut. The sidebands are marked as “B”. (b) The profile histogram of $M(\mu\mu K)$ versus $\alpha$ . (c) The profile histogram of $L_{xy}$ versus $\alpha$ . The red arrow represents $L_{xy}$ cut value. . . . .	73
4.5	The $\alpha$ distributions for the background events with the parameterizing function overlaid. . . . .	74
4.6	Invariant mass of $B^+ \rightarrow J/\psi K^+$ from realistic Monte Carlo overlaid with the reflection from $B^+ \rightarrow J/\psi \pi^+$ and partially reconstructed B-mesons. . . . .	76
4.7	Fitting results projected onto the invariant mass distribution of data. . . . .	77
4.8	Fitting results projected onto the $\alpha$ distribution of data. . . . .	78
4.9	A scatter plot of $M(\mu\mu K)$ versus $M(\mu\mu\pi)$ . The lines shown represent the $2.5\sigma$ around $M(B^+)$ . . . . .	80
4.10	The $M(\mu\mu\pi)$ versus the third track’s invariant mass. This mass is calculated by constraining the three tracks to form a $B^+$ . . . . .	82
4.11	$dE/dx$ ID distribution for (a) pion and (b) kaon. . . . .	83
4.12	Fitting results projected onto the invariant mass distribution of data. . . . .	85
4.13	Fitting results projected onto the $\alpha$ distribution of data. . . . .	86
4.14	Fitting results projected onto the $dE/dx$ ID distribution of data. . . . .	87
5.1	The pull distributions of each fitting parameter from the toy MC test. . . . .	90
5.2	Fitted ratio versus input ratio from the toy MC test. The slope of dashed line is 1. . . . .	91



# List of Tables

2.1	The description of different parts of Figure 2.6. . . . .	27
2.2	The summary of SVX mechanical parameters. . . . .	27
2.3	The technical specifications of the CDF muon systems. . . . .	35
2.4	The basic properties of the calorimeters at CDF. . . . .	44
3.1	The $J/\psi$ selection cuts. . . . .	61
4.1	The fitted parameters used in $h_{sig}(\alpha)$ for each decay mode and $h_{bkg}(\alpha)$ for the background events, where $f_1 = 1 - f_2 - f_3$ to normalize the functions. . . . .	69
4.2	The value of the fitted parameters that best represent data. . .	79
4.3	The value of the fitted parameters that best represent data when the $dE/dx$ information is used. . . . .	84
5.1	Input values for fitting test. . . . .	92
5.2	The values of the fitted parameters that best represent the data with a $2^{nd}$ polynomial background. . . . .	92
5.3	The results of fitting the data for different fitting ranges . . . .	93
5.4	Probability of hadronic interaction on single kaons and pions. . .	94
5.5	Systematic sources and their values. . . . .	94



# Chapter 1

## Introduction

Studies of non-leptonic decays of  $B$  mesons are very useful to gain a better understanding of the dynamics of strong interactions, which are responsible for the bounding of quarks and gluons into hadrons. The complexity of the processes involved in non-leptonic decays is illustrated in Fig. 1.1, where it is shown how strong interactions of quarks can affect a simple  $b \rightarrow c\bar{u}d$  tree diagram. Several approaches have been developed by theorists in order to obtain reliable predictions for these decays. In particular, a factorization prescription allows us to write the decay amplitude in terms of a product of hadronic current matrix elements.

This chapter represents a brief theoretical introduction to the study of the  $B^+ \rightarrow J/\psi\pi^+$  decay mode. The principles and the limits of the factorization-based approach, widely used for the treatment of non-leptonic decays, are described, and the properties of the  $B^+ \rightarrow J/\psi\pi^+$  channel are then discussed.

### 1.1 The effective Hamiltonian

Let us consider, as an example of two-body non-leptonic decay, the mode  $\bar{B}^0 \rightarrow D^+\pi^-$ . The basic diagram for this process is shown in Fig. 1.1, in which we can distinguish a tree diagram  $b \rightarrow c\bar{u}d$  and a spectator quark  $\bar{d}$ . Strong interactions affect this simple  $W$ -exchange in different ways, according

to the energy of the exchanged gluons. Short-range interactions, characterized by energy scales  $> \Lambda_{QCD}$ , can be described by perturbative QCD, while long-range interactions, characterized by energy scale  $\leq \Lambda_{QCD}$ , can not be treated perturbatively.

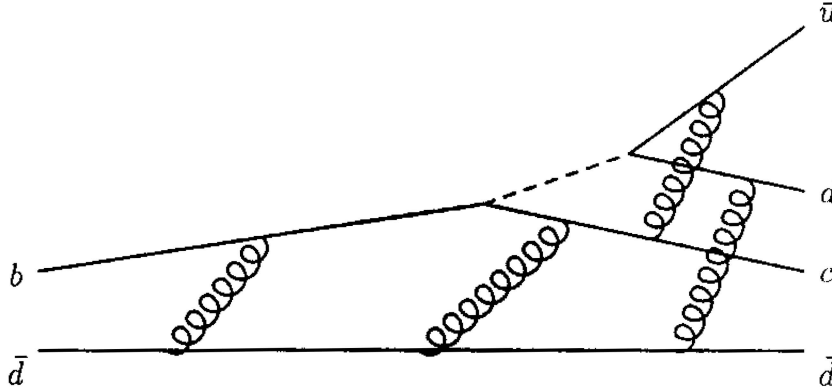


Figure 1.1: Tree diagram  $b \rightarrow c\bar{u}d$ , with a spectator quark  $\bar{d}$ , affected by gluon exchanges.

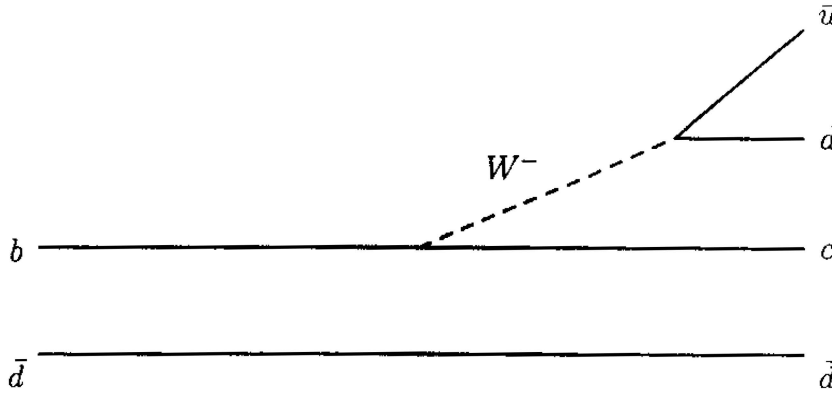


Figure 1.2: The tree diagram for the decay  $\bar{B}^0 \rightarrow D^+\pi^-$ .

In order to manage these complicate effects, the technique known as the *Operator Product Expansion* [1] is used to write the amplitude of a generic decay  $B \rightarrow f$  as:

$$A = -\frac{G_F}{\sqrt{2}} V_{CKM} \sum_j C_j \cdot \langle f | O_j | B \rangle \left[ 1 + O\left(\frac{m_b^2}{M_W^2}\right) \right], \quad (1.1)$$

where the *Wilson* coefficients  $C_j$  are independent of the final state  $f$ , the  $O_j$  are local four-quarks operators and  $V_{CKM}$  represents the product of the *CKM* matrix elements for the decay considered. The coefficients  $C_j$  can be interpreted as the “universal” coupling constants of the following effective Hamiltonian:

$$H_{eff} = \frac{G_F}{\sqrt{2}} V_{CKM} \sum_j C_j(\mu) O_j(\mu) + h.c. \quad , \quad (1.2)$$

where we have shown explicitly that the operators  $O_j$  are renormalized at the energy scale  $\mu$ . The  $\mu$ -dependence of the Wilson coefficients assures that the physics is independent of the renormalization scale. However, an appropriate choice of  $\mu$  permits to disentangle the physics of hard QCD interaction from the physics of soft gluon exchanges. Indeed, the effects of the heavy degrees of freedom, which have been integrated out of the theory, are included in the coefficients  $C_j$ . They therefore need to be evaluated at a scale  $\mu$  where a perturbative expansion is possible. The effects of long-distance interactions, instead, are included in the hadronic matrix elements  $\langle f|O_j|B \rangle$  and cannot be evaluated by perturbative methods.

The structure of the relevant operators  $O_j$  depends on the particular process. For  $b \rightarrow c\bar{u}d$  transitions the effective Hamiltonian is:

$$H_{eff} = \frac{4G_F}{\sqrt{2}} V_{cb} V_{ud}^* [C_1(\mu) O_1(\mu) + C_2(\mu) O_2(\mu)] \quad , \quad (1.3)$$

with:

$$O_1 = (\bar{c}_j \gamma_\mu \frac{1-\gamma_5}{2} b_i) (\bar{d}_j \gamma^\mu \frac{1-\gamma_5}{2} u_j) \quad (1.4)$$

$$O_2 = (\bar{c}_j \gamma_\mu \frac{1-\gamma_5}{2} b_j) (\bar{d}_j \gamma^\mu \frac{1-\gamma_5}{2} u_j) \quad , \quad (1.5)$$

where the Roman indices give the explicit color structure of the quarks. For  $B$  mesons decays, a reasonable choice of the scale is  $\mu \sim m_b$ . The coefficients  $C_{1,2}$  evaluated at this scale have values  $C_1 \approx 1.13$ ,  $C_2 \approx -0.29$  (while in the limit of no QCD corrections:  $C_1 = 1$ ,  $C_2 = 0$ ).

## 1.2 The factorization prescription

From Eq. 1.1 we see that the amplitude for a non-leptonic decay depends on complicate hadronic matrix elements  $\langle f|O_j|B\rangle$ , whose evaluation is not trivial. The factorization hypothesis overcomes these difficulties by replacing the hadronic matrix elements with more manageable products of current matrix elements. In the following we illustrate how factorization works considering three types of decays.

### 1.2.1 Type-I decays

In the decay  $\bar{B}^0 \rightarrow D^+\pi^-$  the  $(\bar{u})d$  quark pair is produced as a point-like, color-singlet state. Since the energy released to the pair is quite high, it can escape from the quark-gluon cloud before it reaches the size of a meson and the corresponding color dipole becomes relevant. This *color transparency* argument[2] allows us to neglect the interactions of the light meson with the rest of the quark-gluon system and to factorize the hadronic matrix elements:

$$\langle D\pi|O_{1,2}|B\rangle = \langle D|\bar{c}\gamma_\mu\frac{1-\gamma_5}{2}b|B\rangle\langle\pi|\bar{d}\gamma_\mu\frac{1-\gamma_5}{2}u|0\rangle \quad (1.6)$$

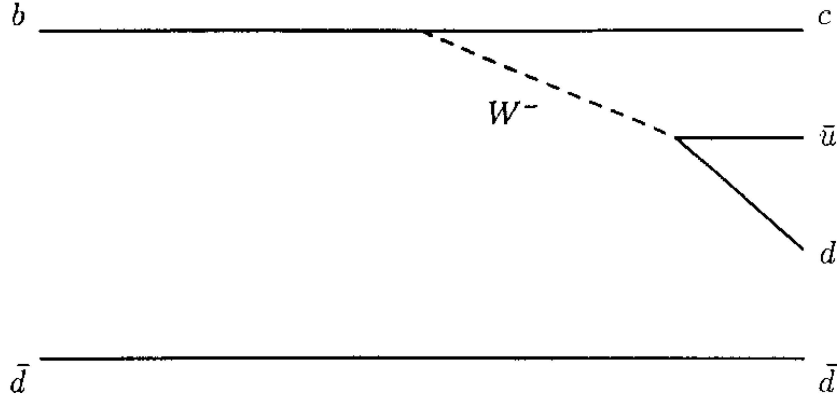
where the color structures of  $O_{1,2}$  have been omitted. Considering also the color structures, we can expect a suppression factor of  $1/N_c$  for the  $O_2$  amplitude, where  $N_c = 3$  is the number of colors. Therefore we can write the amplitude of the decay as:

$$A = -i\frac{4G_F}{\sqrt{2}}V_{cb}V_{ud}^*a_1\langle D|\bar{c}\gamma_\mu\frac{1-\gamma_5}{2}b|B\rangle\langle\pi|\bar{d}\gamma_\mu\frac{1-\gamma_5}{2}u|0\rangle \quad (1.7)$$

where:

$$a_1 = C_1 + \frac{1}{N_c}C_2 \sim 1. \quad (1.8)$$

The current matrix elements are parameterized with the use of form factors

Figure 1.3: The tree diagram for the decay  $\bar{B}^0 \rightarrow D^0 \pi^0$ .

and decay constants:

$$\langle \pi | \bar{d} \gamma_\mu \frac{1 - \gamma_5}{2} u | 0 \rangle = i f_\pi q_\mu \quad (1.9)$$

$$\begin{aligned} \langle D | \bar{c} \gamma_\mu \frac{1 - \gamma_5}{2} b | B \rangle &= F_1(q^2) \left[ (p_B + p_D)_\mu - \frac{M_B^2 - M_D^2}{q^2} q_\mu \right] \\ &+ F_0(q^2) \frac{M_B^2 - M_D^2}{q^2} q_\mu \quad , \end{aligned} \quad (1.10)$$

where  $q_\mu$  is the four-momentum transferred to the pion ( $q^2 = m_\pi^2$ ). The pion decay constant  $f_\pi \approx 131$  MeV is obtained from the leptonic decay  $\pi^+ \rightarrow \mu^+ \nu_\mu$  and it is known with good accuracy. The form factors of the heavy-to-heavy transition  $B \rightarrow D$  come from the covariant decomposition of the current matrix element. In general, there are two form factors ( $F_0, F_1$ ) if the daughter meson is pseudoscalar, while four form factors ( $V, A_0, A_1, A_2$ ) are defined for a vector meson. Large theoretical uncertainties and model dependencies can affect the knowledge of these form factors.

For heavy-to-heavy transitions, heavy-quark symmetry [3] implies constraints on the form factors. For instance, in the case of a pseudoscalar daughter meson:

$$F_1(q^2) = \frac{m_B + m_D}{2\sqrt{m_B m_D}} \cdot \xi(\omega) \quad (1.11)$$

$$F_0(q^2) = \frac{2\sqrt{m_B m_D}}{m_B + m_D} \cdot \frac{\omega + 1}{2} \cdot \xi(\omega) \quad (1.12)$$

where  $\omega = v_B \cdot v_D$  is the product of the four-velocities of the two mesons, and  $\xi(\omega)$  is the Isgur-Wise function [4, 5]. The deviations due to the finite masses of the heavy quarks can be analyzed in detail with the use of the *Heavy Quark Effective Theory* [3]. Finally, from the study of semileptonic decays it is possible to extract reliable predictions for these form factors.

Decays that are described by a tree diagram as in Fig. 1.1 are denoted as Type-I (or color-allowed) transitions. For energetic decays, color transparency suggests that factorization works properly and they are well described by a “universal” coefficient  $a_1 \sim 1$ .

### 1.2.2 Type-II decays

The decay  $\bar{B}^0 \rightarrow D^0 \pi^0$ , described by the tree diagram in Fig. 1.2.1, is allowed if the quark pair ( $\bar{u}c$ ) has the right color structure to form a meson. This is equivalent, as the color structure of the operators  $O_{1,2}$  suggests, to a suppression factor of  $1/N_c$  for the  $O_1$  amplitude. Therefore we can write the decay amplitude as:

$$A = -i \frac{4G_F}{\sqrt{2}} V_{cb} V_{ud}^* a_2 \langle \pi | \bar{d} \gamma_\mu \frac{1 - \gamma_5}{2} b | B \rangle \langle D | \bar{u} \gamma_\mu \frac{1 - \gamma_5}{2} c | 0 \rangle, \quad (1.13)$$

where:

$$a_2 = C_2 + \frac{1}{N_c} C_1 \sim 1. \quad (1.14)$$

The current matrix elements are again parameterized with the use of form factors and decay constants as in Eq. 1.9 and Eq. 1.10, with  $q_\mu$  that now represents the four-momentum transferred to the  $D$  meson ( $q^2 = m_D^2$ ). For heavy-to-light transitions like  $B \rightarrow \pi$  the constraints from heavy-quark sym-

metry cannot be exploited. Usually, phenomenological models based on several assumptions are used to evaluate these form factors, and factorization-based predictions are therefore affected by large theoretical uncertainties and model dependencies.

Decays described by a tree diagram as in Fig. 1.2.1 are denoted as Type-II (or color-suppressed) transitions. Two-body decays with a charmonium resonance in the final state, like  $B^+ \rightarrow J/\psi\pi^+$  or  $B^+ \rightarrow J/\psi K^+$ , belong to this category. We point out that in this case there are no color transparency arguments justifying factorization of the hadronic matrix elements: non-factorizable contributions can become dominant and change relevantly the predictions obtained with the factorized amplitudes. There are also experimental results that suggest departure from simple factorization. For instance, measurements of the decay amplitudes in the  $B \rightarrow J/\psi K^*(892)$  mode [6, 7] show discrepancies with the expectations based on the absence of final state interactions (as it is supposed in the simple factorization scheme).

### 1.2.3 Type-III decays

Decays like  $B^- \rightarrow D^0\pi^-$  are described by both color-allowed and color-suppressed diagrams and therefore are sensitive to interference terms between them. In the limit of validity of factorization, the relative sign of  $a_1$  and  $a_2$  suggests that for decays of B mesons that interference is constructive.

## 1.3 Deviations from factorization

Using Fierz identities, it is possible to write the effective Hamiltonian in Eq. 1.3 as the sum of a color-singlet operator  $O_1$  and a color-octet operator  $O^{(8)}$ . This implies also a transformation of the Wilson coefficients; in particular:  $C_1 \rightarrow C_1 + (C_2/N_c)$ . We obtain the following transformed decay amplitude for a type-I decay:

$$A = -i \frac{4G_F}{\sqrt{2}} V_{cb} V_{ud}^* \{ [C_1 + (1/N_c)C_2] \mathcal{M}_1 + 2C_2 \mathcal{M}_8 \}, \quad (1.15)$$

where:

$$\mathcal{M}_1 = \langle \pi D | O_1 | B \rangle \quad (1.16)$$

$$\mathcal{M}_8 = \langle \pi D | O^{(8)} | B \rangle . \quad (1.17)$$

The simple factorization approach described in the previous section is therefore based on the following assumptions:

1. Negligible contribution from the color-octet operator :

$$\mathcal{M}_1 \approx 0 .$$

2. Assumption of factorization for the color-singlet matrix element :

$$\mathcal{M}_1 = \langle D | (\bar{c}b)_{V-A} | B \rangle \langle \pi | (\bar{d}u)_{V-A} | 0 \rangle ,$$

where  $(\bar{c}b)_{V-A}$  is a simplified notation for  $\bar{c}\gamma_\mu[(1 - \gamma_5)/2]b$ .

In order to describe deviations from factorization, the following parameters are introduced:

$$\epsilon_1 = \frac{\mathcal{M}_1}{\langle D | (\bar{c}b)_{V-A} | B \rangle \langle \pi | (\bar{d}u)_{V-A} | 0 \rangle} - 1 \quad (1.18)$$

$$\epsilon_8 = \frac{\mathcal{M}_8}{\langle D | (\bar{c}b)_{V-A} | B \rangle \langle \pi | (\bar{d}u)_{V-A} | 0 \rangle} . \quad (1.19)$$

The parameter  $\epsilon_1$  measures the deviation of  $\mathcal{M}_1$  from the factorized form, while  $\epsilon_8$  measures the contribution from the octet-operator. Thus, the decay amplitude can be written in the general form:

$$A = -i \frac{4G_F}{\sqrt{2}} V_{cb} V_{ud}^* a_1^{eff} \langle D | \bar{c}\gamma_\mu \frac{1 - \gamma_5}{2} b | B \rangle \langle \pi | \bar{d}\gamma_\mu \frac{1 - \gamma_5}{2} u | 0 \rangle , \quad (1.20)$$

where:

$$a_1^{eff} = [C_1 + (C_2/N_c)](1 + \epsilon_1) + 2C_2\epsilon_8 . \quad (1.21)$$

Also for class-II decays it is possible to define a coefficient  $a_2^{eff}$ :

$$a_2^{eff} = [C_2 + (C_1/N_c)](1 + \tilde{\epsilon}_1) + 2C_1\tilde{\epsilon}_8 . \quad (1.22)$$

We can see that, also assuming that factorization of  $\mathcal{M}_1$  is well satisfied ( $\tilde{\epsilon}_1 \approx 1$ ),  $a_2^{eff}$  can be sensitive to octet operator admixture, due to the smallness of the term  $C_2 + (C_1/N_c)$ . In other words, while the simple factorization approach with  $a_1^{eff} \approx 1$  represents a reliable scheme for class-I decays, sizeable deviations from the predicted decay rates are surprising for class-II decays.

## 1.4 Generalized factorization

It is still possible to preserve the factorization-based approach for the treatment of non-leptonic decays, despite significant non-factorizable contributions, if the coefficients  $a_{1,2}^{eff}$  are interpreted as phenomenological parameters to be fitted on data [8, 9]. Sets of theoretically and experimentally clean modes are used to extract  $a_{1,2}^{eff}$ . These fitted values are then employed to obtain predictions for other decays [10]. The underlying assumption is, of course, a weak dependence of the parameters  $a_{1,2}^{eff}$  on the particular process, which is not supported by strong theoretical arguments and needs therefore to be tested on data.

In an equivalent approach, deviations from factorizations are described introducing additional parameters in the factorized amplitude [11]; again, the values of the parameters are derived from data.

For class-I decays, the comparison between the values of  $a_1^{eff}$  extracted from quite different channels supports the validity of simple factorization with  $a_1^{eff} \approx 1$ . For class-II decays, data seem to agree with the assumption of weak dependence of  $a_2^{eff}$  on the particular process. However, the reliability of this conclusion is limited by the not well understood theoretical uncertainties affecting the heavy-to-light form factors used for these channels. It is therefore extremely important that predictions rely on well tested phenomenological models for the form factors.

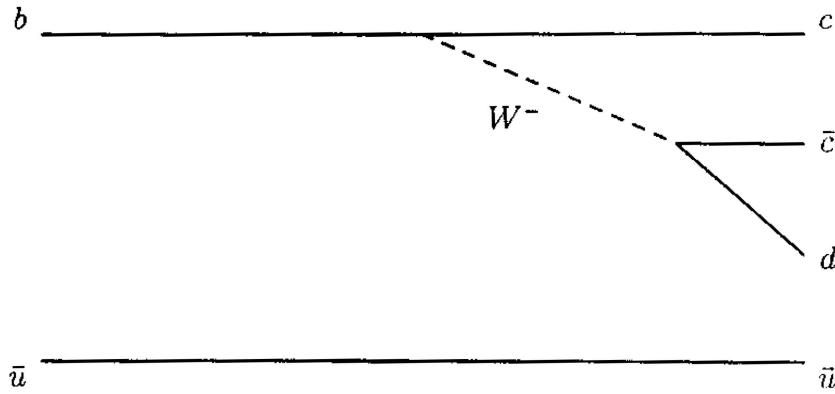


Figure 1.4: The tree diagram for the decay  $B^- \rightarrow J/\psi \pi^-$ .

## 1.5 Generalized factorization

The  $B^\pm \rightarrow J/\psi \pi^\pm$  channel is a class-II decay, described at the leading order by the tree diagram  $b \rightarrow c\bar{c}d$  in Fig. 1.5<sup>1</sup>. According to the scheme outlined in the previous sections, the factorized amplitude is given by:

$$A_{tree}(B^\pm \rightarrow J/\psi \pi^\pm) \sim a_2^{eff} V_{cb}^* V_{cd} f_{J/\psi} F_{b \rightarrow \pi}(q^2 = m_{J/\psi}^2), \quad (1.23)$$

where  $f_{J/\psi}$  is the decay constant of the  $J/\psi$ , and  $F_{B \rightarrow \pi}$  denotes the form factors contribution. Similarly, the Cabibbo-allowed decay  $B^\pm \rightarrow J/\psi K^\pm$  is described by the tree diagram  $b \rightarrow c\bar{c}s$  and the factorized amplitude is:

$$A_{tree}(B^\pm \rightarrow J/\psi K^\pm) \sim a_2^{eff} V_{cb}^* V_{cs} f_{J/\psi} F_{b \rightarrow K}(q^2 = m_{J/\psi}^2). \quad (1.24)$$

If the tree diagram is the dominant contribution for both decays ( $A = A_{tree}$ ), the ratio of the branching fractions is an interesting quantity because it does not depend on the particular value of  $a_2^{eff}$  (sensitive to non-factorizable

<sup>1</sup>Actually the  $b \rightarrow c\bar{c}d$  diagram describes the decay  $B^- \rightarrow J/\psi \pi^-$ . However, in the present chapter, and unless stated explicitly, with this notation we will denote also the  $CP$ -conjugate decay  $B^+ \rightarrow J/\psi \pi^+$ .

contributions):

$$\frac{\mathcal{B}(B^\pm \rightarrow J/\psi\pi^\pm)}{\mathcal{B}(B^\pm \rightarrow J/\psi K^\pm)} = \frac{|V_{cd}|^2}{|V_{cs}|^2} \cdot \frac{|F_{B \rightarrow \pi}|^2}{|F_{B \rightarrow K}|^2} \sim \tan^2 \theta_C \frac{|F_{B \rightarrow \pi}|^2}{|F_{B \rightarrow K}|^2}, \quad (1.25)$$

where  $\theta_C$  is the Cabibbo angle. Therefore we expect for the  $B^\pm \rightarrow J/\psi\pi^\pm$  mode a branching fraction of the order of 5% of  $\mathcal{B}(B^\pm \rightarrow J/\psi K^\pm)$ . In addition, the ratio of the branching fractions is sensitive to the quality of the phenomenological models employed to compute the heavy-to-light form factors in  $F_{B \rightarrow \pi}$  and  $F_{B \rightarrow K}$ . A calculation of the above amplitudes gives [10]:

$$\mathcal{B}(B^\pm \rightarrow J/\psi\pi^\pm) = 0.038(a_2^{eff})^2 \quad (1.26)$$

$$\mathcal{B}(B^\pm \rightarrow J/\psi K^\pm) = 0.852(a_2^{eff})^2, \quad (1.27)$$

and thus:

$$\frac{\mathcal{B}(B^\pm \rightarrow J/\psi\pi^\pm)}{\mathcal{B}(B^\pm \rightarrow J/\psi K^\pm)} = 0.045. \quad (1.28)$$

Because of the simplicity of the phenomenological model used for the determination of the form factors, the theoretical expectation in Eq. 1.28 has to be considered no more than a rough estimate of the ratio, and therefore no uncertainties are provided with the prediction.

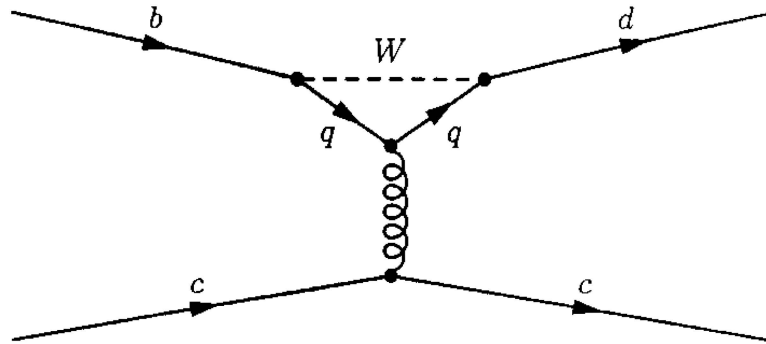


Figure 1.5: The gluonic penguin diagram ( $q = u, c, t$ ).

While the tree diagram dominance is a reliable hypothesis for the  $B^\pm \rightarrow$

$J/\psi K^\pm$  channel, the Cabibbo-suppressed  $B^\pm \rightarrow J/\psi \pi^\pm$  mode may be sensitive to higher order contributions from additional operators in the effective Hamiltonian. They correspond to 1-loop diagrams known as “penguin diagrams”. Figure 1.5 shows a gluonic (or QCD) penguin; we distinguish three possible diagrams, characterized by the identity of the quark in the loop. Electroweak penguins are also possible, characterized by the emission of a photon or a  $Z^0$  (see Fig. 1.5).

penguin diagrams lead to deviations from the simple expectation stated in Eq. 1.25. Furthermore, they weaken the reliability of the theoretical prediction because uncertainties on penguin diagrams calculations sum up with the uncertainties on the form factors. Finally, the interference between the tree diagram and penguin diagrams with different weak and strong phases can produce significant direct  $CP$ -violation in  $B^\pm \rightarrow J/\psi \pi^\pm$  decays.

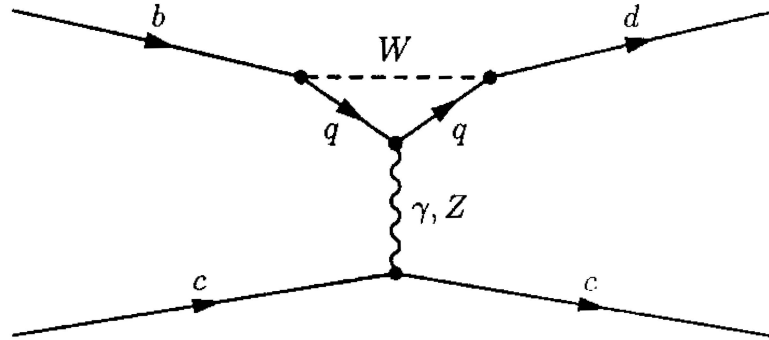


Figure 1.6: The electroweak penguin diagram ( $q = u, c, t$ ).

### 1.5.1 Generalized factorization

Denoting with  $T$  the contribution from the tree diagram and with  $P^q$  the contribution from the penguin diagram with the quark  $q$  in the loop ( $q = u, c, t$ ), the total amplitude for the  $B^- \rightarrow J/\psi \pi^-$  mode can be written as:

$$A(B^- \rightarrow J/\psi \pi^-) = V_{tb}V_{td}^* P^t + V_{cb}V_{cd}^*(T + P^c) + V_{ub}V_{ud}^* P^u, \quad (1.29)$$

Where we have shown explicitly the CKM matrix coefficients. From the unitarity of the CKM matrix we have:

$$V_{tb}V_{td}^* = -V_{cb}V_{cd}^* - V_{ub}V_{ud}^* , \quad (1.30)$$

that, substituted in Eq. 1.29, yields:

$$A(B^- \rightarrow J/\psi\pi^-) = V_{cb}V_{cd}^*(T + P^c - P^t) + V_{ub}V_{ud}^*(P^u - P^t) , \quad (1.31)$$

We note that in the above expression only differences of penguin contributions appear, in which the ultraviolet divergences associated to the quark loop cancel out.

The calculation of the Wilson coefficients for the penguin operators suggests a suppression factor for penguin contributions of the order of  $10^{-2}$ . Thus, neglecting  $P^c - P^t$  we can write the amplitude in the following form:

$$A(B^- \rightarrow J/\psi\pi^-) \approx \xi_c a_2 e^{i\Delta} + \xi_u b , \quad (1.32)$$

where  $\xi_c \equiv V_{cb}V_{cd}^*$ ,  $\xi_u \equiv V_{ub}V_{ud}^*$ ,  $a_2$  and  $b$  are the magnitudes of  $T$  and  $P^u - P^t$  respectively, and  $\Delta$  is the strong phase difference between the two terms in the sum.

The weak structure of the two contributions to the amplitude can be examined from the Wolfenstein parameterization of the CKM matrix(Eq. 1.15):

$$\xi_c \sim A\lambda^3 \quad (1.33)$$

$$\xi_u \sim A\lambda^3(\rho - i\eta) . \quad (1.34)$$

Since the two contributions are characterized by different weak phases, the existence of direct  $CP$ -violation relies on the condition  $\Delta \neq 0$ . Considering also the amplitude for the  $B^+ \rightarrow J/\psi\pi^+$  decay:

$$A(B^+ \rightarrow J/\psi\pi^+) \approx \xi_c^* a_2 e^{i\Delta} + \xi_u^* b , \quad (1.35)$$

the  $CP$ -violation observable will be given by:

$$\begin{aligned} \mathcal{A}_\pi &= \frac{\Gamma(B^- \rightarrow J/\psi\pi^-) - \Gamma(B^+ \rightarrow J/\psi\pi^+)}{\Gamma(B^- \rightarrow J/\psi\pi^-) + \Gamma(B^+ \rightarrow J/\psi\pi^+)} \\ &= \frac{2a_2 b \sin \Delta \sin \gamma \left| \frac{\xi_u}{\xi_c} \right|}{a_2^2 + \left| \frac{\xi_u}{\xi_c} \right|^2 b^2 + 2a_2 b \left| \frac{\xi_u}{\xi_c} \right| \cos \Delta \cos \gamma}, \end{aligned} \quad (1.36)$$

where  $\gamma$  is one of the angles of the Unitarity Triangle:

$$\gamma = \text{Arg} \left[ -\frac{\xi_u^*}{\xi_c^*} \right].$$

Exploiting the dominance of the  $a_2^2$  term in the denominator, we have:

$$\mathcal{A}_\pi = 2 \frac{b}{a_2} \sin \Delta \sin \gamma \left| \frac{V_{ub} V_{ud}}{V_{cb} V_{cd}} \right|. \quad (1.37)$$

it has been shown [12] that values of  $b/a_2 \approx 0.05$  are possible; the calculation for strong penguins is affected by large theoretical uncertainties, but for electroweak penguins it is quite reliable. Furthermore, the strong phase difference  $\Delta$  could be large. This result in a direct  $CP$ -violation for the  $B^\pm \rightarrow J/\psi\pi^\pm$  mode that can be at the percent level. However, since the uncertainty on this prediction is large, the asymmetry could be significantly smaller.

We conclude this discussion showing that no direct  $CP$ -violation is expected in the SM for the  $B^\pm \rightarrow J/\psi\pi^\pm$  channel. Indeed in this case, also including the penguin contributions, we have:

$$A(B^- \rightarrow J/\psi K^-) = V_{cb} V_{cs}^* (T + P^c - P^t) + V_{ub} V_{us}^* (P^u - P^t), \quad (1.38)$$

and since the second term in the sum is both cabibbo-suppressed and penguin coupling constants-suppressed, we have:

$$A(B^- \rightarrow J/\psi K^-) \approx V_{cb} V_{cs}^* (T + P^c - P^t). \quad (1.39)$$

Therefore the decay is approximately characterized by a single weak phase and no CP-violating interference terms are possible.



## Chapter 2

# CDF Experiment

The detector used in this analysis is the Collider Detector at Fermilab (CDF) located at the Fermi National Accelerator Laboratory (Fermilab), in Illinois (USA). CDF uses proton-antiproton collisions generated at the Tevatron Accelerator complex. Until the Large Hadron Collider (LHC) is completed at CERN, the Tevatron is the highest energy collider in the world. In this chapter the Tevatron and CDF are described.

### 2.1 The Accelerator and Collider

The Tevatron is a circular accelerator of about 1 km of radius which collides bunches of protons and antiprotons accelerated in opposite directions with a total center-of-mass energy  $\sqrt{s} = 1.96$  TeV. The acceleration happened in five stages and a schematic of the accelerator is shown in Figure 2.1. The protons used in the collisions start out as hydrogen atoms from a bottle of hydrogen gas. The hydrogen atoms are ionized ( $H^+$ ) and accelerated in the Cockroft-Walton preaccelerator to 750 keV. They are then sent through a linear accelerator (LINAC) which increases their energy to 400 MeV. The electrons are stripped from the hydrogen ions by sending the ions through a carbon foil, resulting in a 400 MeV beam of protons. The beam of protons are sent to a 75 m synchrotron (Booster), which increases their energy to 8 GeV, and separates the protons

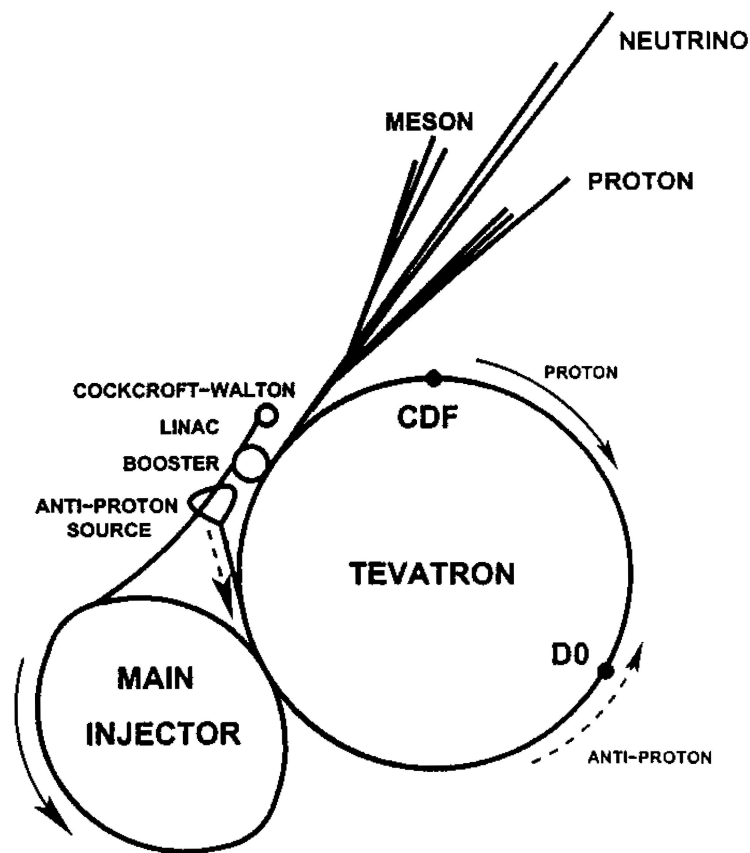


Figure 2.1: Cutaway view of the CDF detector.

into bunches. Finally they are sent through two more synchrotrons called the Main Injector and the Tevatron, where they reach energies of 150 GeV and 980 GeV respectively.

Antiprotons must be created in the lab by colliding protons with a fixed target. Protons exiting the Booster are sent toward a nickel target, and the antiprotons created in this collision are separated from other products. The antiprotons are “cooled” (reducing the phase space occupied), and accelerated so they can be sent to the Main Injector and be accelerated along with the protons.

The proton and antiproton beams are composed of 36 bunches each. The two beams are focused using quadrupole magnets at two points along the cir-

cumference of the ring, where the bunches cross about every 396 ns. These two regions are called D0, where the experiment of the same name is located, and B0, the center of the CDF experiment. The luminous region has a dispersion of about 30 cm in the direction of the beams ( $\sigma_z \simeq 30$  cm) and the profile of the beam in the transverse plane is approximately circular and has a gaussian dispersion  $\sigma_t^{beam} \simeq 30 \mu\text{m}$ .

The Tevatron produced its first  $\bar{p}p$  collisions in October of 1985, and since then has evolved, increasing the instantaneous luminosity. In 1996, after taking data on and off for about ten years (called "Run I"), the Tevatron was closed to undergo technical upgrades to improve both the center of mass energy, from 1.8 to 1.96 TeV, and the delivered luminosity for the new period of data taking called "Run II". At the present, the Tevatron is functioning with an instantaneous luminosity close to  $1 \times 10^{32} \text{ cm}^{-2}\text{s}^{-1}$ .

The accumulation of total integrated luminosity over many stores is shown in Figure 2.2. After selecting data where the detector is running without major problems, there remains  $220 \text{ pb}^{-1}$  of data for this analysis.

## 2.2 The CDF Detector

The CDF detector is a multi-purpose solenoidal detector, which includes a precision tracking system and fine-grained muon detection. These are the parts which are the most important for this analysis. The other parts of the detector include electromagnetic and hadronic calorimeters, a Time-of-Flight system and a Cherenkov Luminosity Counter. They will be described in further section.

The detector's cutaway view is shown in Figure 2.3 and its elevation view in Figure 2.4. They depict the main parts of the detector - the innermost silicon system, surrounded by the central drift chamber, the Time-of-Flight system, the magnetic solenoid, calorimeters and outermost muon detectors.

The niobium-titanium magnetic solenoid has a radius of 1.5 m and a length of 4.8 m. It generates a 1.4 T magnetic field, parallel to the beam axis. The current in the solenoid is 4605 A, which is regulated by a feedback loop moni-

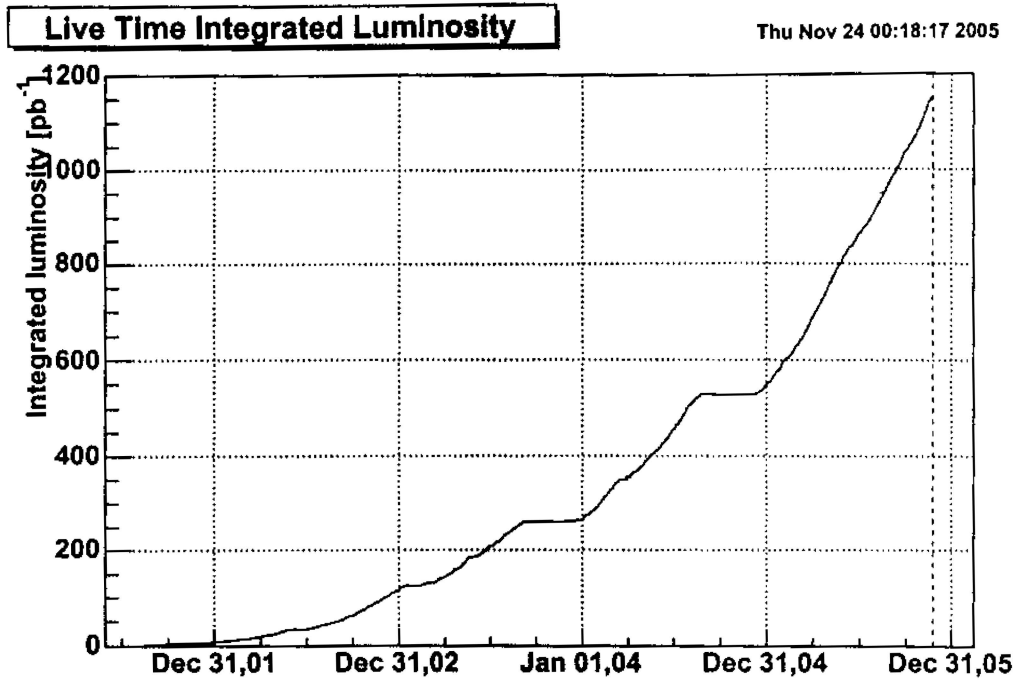


Figure 2.2: Cutaway view of the CDF detector.

toring an NMR probe. The magnetic field curves the charged particles' tracks, and the measured curvature allows us to obtain the tracks' momenta. It is important to know the magnetic field precisely, because the accuracy of the track parameters depends on it.

### 2.2.1 Coordinate System

It is convenient to use cartesian  $(x, y, z)$ , cylindrical  $(r, \phi, z)$  or polar  $(r, \phi, \theta)$  coordinates to describe the detector. The origin of the CDF coordinate system lies in the center of the Central Outer Tracker. the  $z$ - axis is directed horizontally along the beamline, the positive direction is to the east. The protons move in the positive direction, the antiprotons in the negative one. The  $x$ -axis is also directed horizontally, pointing towards the outside of the main ring, and the  $y$ -axis is upwards. The  $\phi$  angle is calculated from the  $x$ -

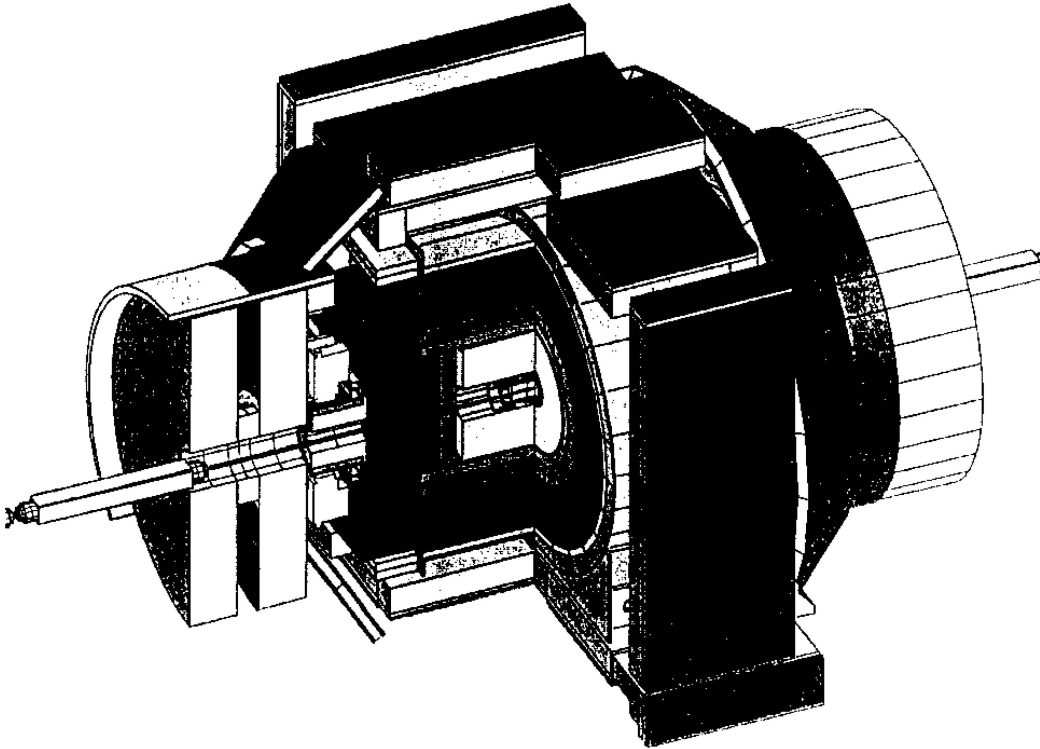


Figure 2.3: Cutaway view of the CDF detector.

axis in the  $x-y$  plane. It ranges from 0 to  $2\pi$ . The azimuthal angle  $\theta$  measured with respect to the positive direction of the  $z$ -axis.

The protons and antiprotons in the detector travel along the  $z$ -axis of the detector's reference frame. It is often convenient to describe their motion in their own reference frame. To do so one should perform a Lorentz boost of the particles momenta and energy along the  $z$ -axis. The  $\theta$  coordinate is not invariant under these boost what makes it somewhat inconvenient to use. The quantity

$$y = \frac{1}{2} \log \frac{E + P_z}{E - P_z}, \quad (2.1)$$

called *rapidity*, is invariant under such boosts. Here  $E$  is the energy of a particle and  $P_z$  is its momentum along the  $z$ -axis. In the ultrarelativistic (massless) limit the energy  $E$  can be replaced with the momentum  $P$  of the particle, and

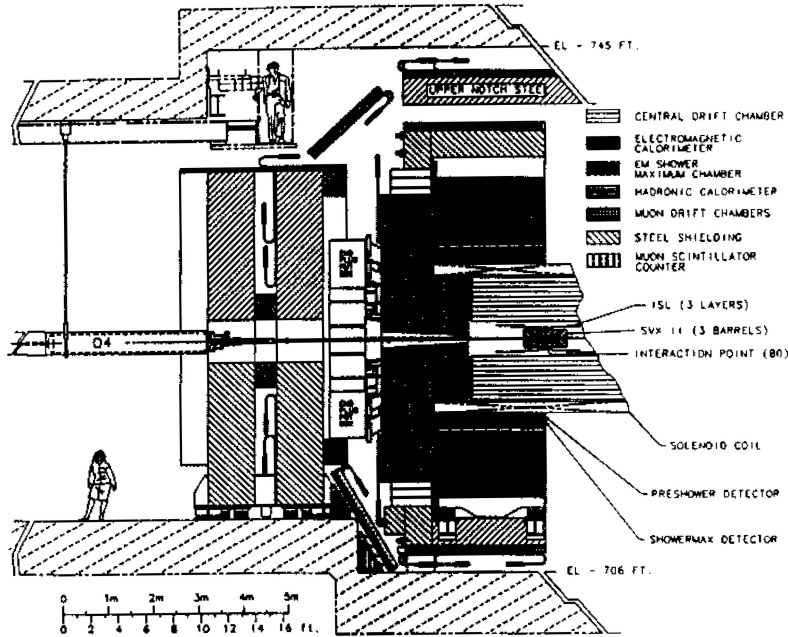


Figure 2.4: Elevation view of the CDF detector.

the rapidity turns into the *pseudorapidity*

$$\eta = \frac{1}{2} \log \frac{P + P_z}{P - P_z} = -\log \tan \frac{\theta}{2}. \quad (2.2)$$

This purely geometrical quantity is used instead of the rapidity  $y$ . The coordinates  $(r, \phi, \eta)$  are usually chosen to describe the detector. The components of the detector are usually partitioned in  $\phi$  and  $\eta$ . In the following sections we will use these coordinates.

With this coordinate system it is often more convenient to express the distance between two different directions (*e.g.* two different tracks) not in terms of an opening angle between them, but in terms of a quantity  $\Delta R = \sqrt{\Delta\phi^2 + \Delta\eta^2}$ . Though, the shape of a surface described by an equation  $\Delta R = \text{const}$  around some direction is not really a cylindrical cone, it is still referred to as a cone.

### 2.2.2 Tracking System

When charged particles pass through matter, they ionize the atoms and molecules of the medium nearby their trajectories. By detecting this ionization the tracks of the particles reconstructed. This process is called *tracking*.

The tracking systems in the CDF are located inside the homogeneous solenoidal magnetic field parallel to the  $z$ -axis. The charged particles inside such a field move along helices with axes parallel to the magnetic field. For this reason the tracks at CDF are described by five parameters: curvature  $C$ , the angle  $\cot \theta$  in the  $r - z$  plane, the coordinates of the point of the closet approach of the track to the primary vertex  $\phi_0$  and  $z_0$ , and the distance from this point to the primary vertex  $d_0$ , called *impact parameter*.

The curvature and the impact parameter can be positive or negative. They are defined by the relation:

$$\begin{aligned} C &= \frac{q}{2R} \\ d_0 &= q \left( \sqrt{x_c^2 + y_c^2} - R \right), \end{aligned} \quad (2.3)$$

where  $q$  is the charge of the particle,  $(x_c, y_c)$  is the center of the projection of the helix onto the  $r - \phi$  plane,  $R$  is the radius of the helix.

The momentum components of the track are expressed in terms of the five track parameters as follows:

$$\begin{aligned} p_t &= \text{const} \cdot \frac{B}{2|C|} \\ p_x &= p_t \cdot \sin \phi_0 \\ p_y &= p_t \cdot \cos \phi_0 \\ p_z &= p_t \cdot \cot \theta \end{aligned} \quad (2.4)$$

The particle's production point cannot be determined from only these 5 parameters, because the defined helix extends to infinity in both directions. We only can say that the particle was created somewhere on the helix. To determine the place of the particle production more precisely we need to find

### CDF Tracking Volume

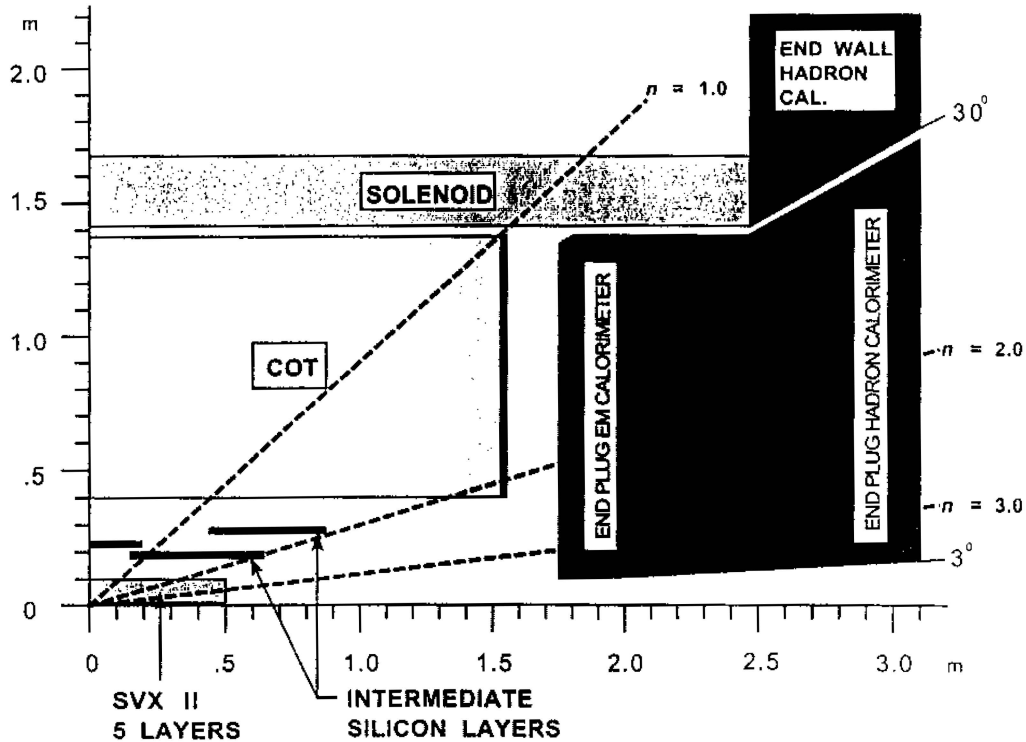


Figure 2.5: The schematic view of the CDF tracking system.

another particle which, presumably, originated from the same space point. Generally more than two particles come from the same place. The point of intersection in space of the particles' tracks gives us the *vertex* for all of them. The process of finding this point is called *vertexing*. The determination of the vertex coordinates with good precision is very important for this analysis.

The tracking system in CDF consists of two main parts: the Silicon Vertex detector (SVX) and the Central Outer Tracker (COT). There are two additional parts: the Intermediate Silicon Layer (ISL) and Layer 00 (L00). Figure 2.5 gives the schematic view of the CDF tracking volume. The calorimeters are also shown in this figure.

Below is a short description of all of the tracking systems.

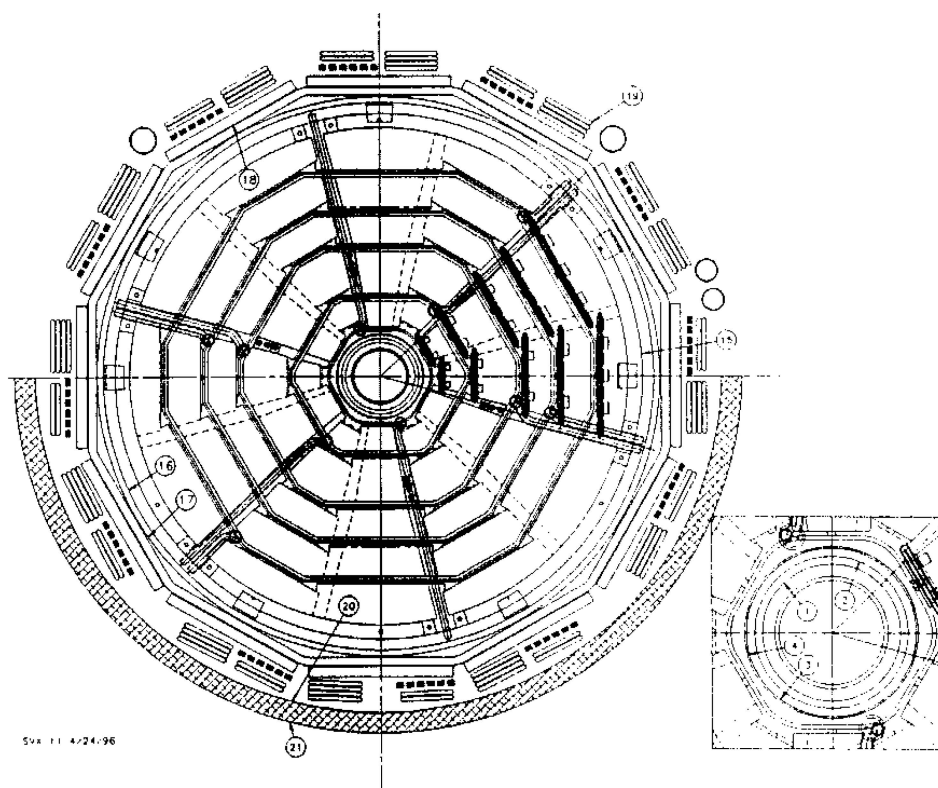


Figure 2.6: The end view of the SVX system.

### Silicon Vertex Detector

The Silicon Vertex detector (SVX) is the innermost part of the CDF serving for a precise determination of the position of the secondary vertex. SVX consists of 720 silicon microstrip detector, also called *wafers*. The microstrip detectors are assembled in so-called *ladders*, 4 wafers in each ladder. Twelve ladders in  $\phi$  comprise a layer. Five layers of radii from 2.5 cm to an outer radius of 10.7 cm make a *barrel*. SVX consists of 3 such barrels, each is 29 cm long, oriented coaxially. The ladders in the barrels are mounted on beryllium bulkheads, together with the water channels necessary to cool the readout electronics. The side view of a bulkhead is shown in Figure 2.6, and the description of different parts of the figure is given in Table 2.1.

The silicon microstrip detector consists of strips of strongly  $p$ -doped silicon ( $p_+$ ) which are implanted on a lightly  $n$ -doped silicon ( $n^-$ ) substrate of about  $300\ \mu\text{m}$  thick. The opposite side of the substrate is covered with the strips of strongly  $n$ -doped silicon ( $n^+$ ). The  $n^+$  strips are oriented at some angle with respect to the  $p^+$  strips. A positive voltage, applied to the  $n^+$  side, takes away the free electrons from the  $n^-$  volume and creates an electric field in it. A charged particle traversing the  $n^-$  volume creates the electron-hole pairs along its track. The hole drift toward the  $p^+$  strips and produce a signal. The electrons drift toward the  $n^+$ , also producing a signal. The position of the hit on  $p^+$  side gives us an  $r - \phi$  coordinate of the hit, while the  $n^-$  side is used to measure the stereo coordinate.

Usually, the signal is found on several strips rather than just one. In this case the exact position of the hit is calculated as an average position of all the hit strips, weighted by the amount of charge on them. The precision achieved in CDF with this method is  $12\ \mu\text{m}$ .

The SVX layers are numbered from 0 (innermost) to 4. In the layers 0, 1 and 3 the  $n^+$  strips are oriented at  $90^\circ$  angle with respect to the axis of the detector (stereo angle), and in the layers 2 and 4 the strips are oriented at the stereo angle  $1.2^\circ$  (Table 2.2). Perspective views of  $\phi$ -side and  $z$ -side of a Layer 0 ladders are shown in Figure 2.7.

The SVX barrels are placed as coaxially, as possible. The remaining alignment shifts are taken into account when we assemble hits into a track. It is more important that the axis of the SVX would coincide with the beam axis, rather than with the axis of the detector. The SVT trigger relies on the impact parameter of the track,  $d_0$ , measured by SVX, and it must be measured with respect to the beamline. It turns out to be more convenient to store the locations of the primary vertices throughout the run, then fit all these locations with a straight line and use this fitted beamline rather than the primary vertices in the physics analyses. Actually, due to misalignment the beamline in the CDF is a few millimeters away from the geometrical central line of the detector. This shift is taken into account in the SVT trigger and in the track

#	Description	Radius, cm
1	Beam pipe outer radius	1.6700
2	Beam pipe flange outer radius	1.8542
3	Inner screen inner radius	2.0500
4	Bulkhead inner radius	2.0000
15	Bulkhead outer radius	12.9000
16	Outer screen inner radius	12.9000
17	Outer screen outer radius	13.2500
18	Port card inner radius	14.1000
19	Cables	16.1000
20	Half cylinder inner radius	16.3000
21	Half cylinder outer radius	17.3000

Table 2.1: The description of different parts of Figure 2.6.

Layer	Radius, cm		# of strips		stereo angle	Ladder active, mm		strip Pitch, $\mu\text{m}$	
	stereo	$r - \phi$	stereo	$r - \phi$		width	length	stereo	$r - \phi$
0	2.55	3.00	256	256	$90^\circ$	15.30	$4 \times 72.43$	60	141
1	4.12	4.57	567	384	$90^\circ$	23.75	$4 \times 72.43$	62	125.5
2	6.52	7.02	640	640	$+1.2^\circ$	38.34	$4 \times 72.38$	60	60
3	8.22	8.72	512	786	$90^\circ$	46.02	$4 \times 72.43$	60	141
4	10.10	10.65	896	896	$-1.2^\circ$	58.18	$4 \times 72.38$	65	65

Table 2.2: The summary of SVX mechanical parameters.

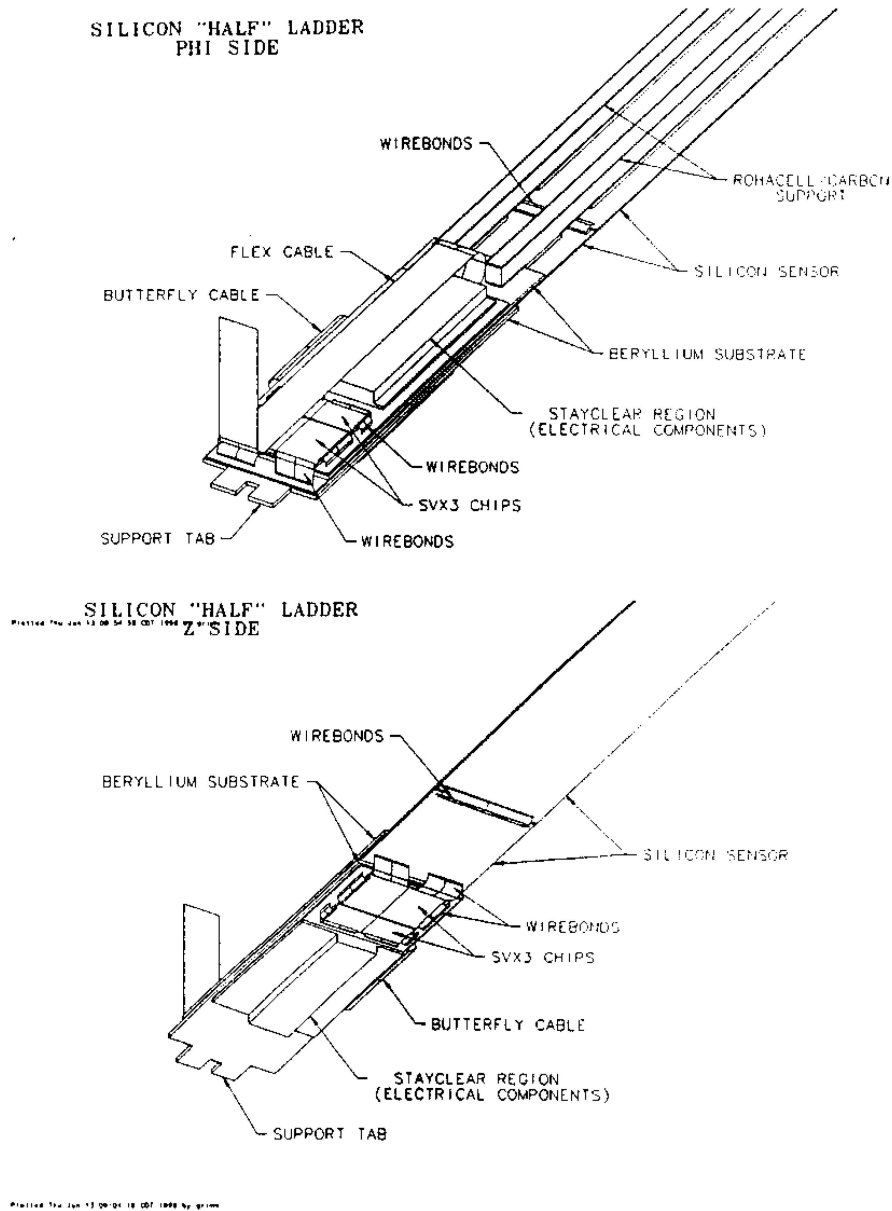


Figure 2.7: Side perspective views of  $r - \phi$  side (top) and  $r - z$  side (bottom) of Layer 0 ladder in the SVX system.

reconstruction.

### Intermediate Silicon Layer and Layer 00

The Intermediate Silicon Layer (ISL) and Layer 00 (L00) were introduced in Run II. Together with the SVX they comprise the CDF silicon tracking system. The ISL and L00 were integrated into the detector system relatively late and the latter did not become fully operational for the data in this analysis.

The **L00** is a silicon detector inside the SVX. It consists of 6 narrow and 6 wide groups of the microstrip detectors, called *wedge*. Six of them are placed at radius 1.35 cm and the other six at the radius 1.62 cm. There are 6 modules in  $z$  of a total length of 95 cm. The sensors in L00 are single-sided and made of more light-weight and radiation-hard silicon than the SVX. They are mounted on a carbon-fiber support structure, which also provides cooling. L00 helps to overcome the multiple scattering effects for tracks passing through the high-density SVX material. This results in the  $d_0$  resolution being as small as 25  $\mu\text{m}$ .

The **ISL** consists of three layers of silicon placed outside of SVX. The region  $0 < |\eta| < 1$  is covered by a single layer of radius 22 cm, and the region  $1 < |\eta| < 2$  is covered by two layers at the radii 20 and 28 cm. The layers consist of the double-sided silicon microstrip detectors, similar to that of SVX, with 55  $\mu\text{m}$  strip pitch on the axial side and 73  $\mu\text{m}$  strip pitch on the stereo side with a  $1.2^\circ$  stereo angle. Only every other strip is readout, which makes the single hit resolution about 26  $\mu\text{m}$  on the axial side and 23  $\mu\text{m}$  on the stereo side. ISL improves the tracking in the central region and allows (together with SVX) for the silicon standalone tracking in the region  $1 < |\eta| < 2$ .

### Central Outer Tracker

The Central Outer Tracker (COT) is a cylindrical drift chamber with inner radius of 40.6 cm, and outer radius of 137.99 cm, and length of 310 cm. It is filled with a 50:50 mixture of Argon and Ethane plus trace amounts of alcohol. The information about the particle tracks is obtained from the wires. The wires

are subdivided into two classes: sense wires, which are actually used to collect the information about the particle tracks, and the potential wires, configuring the electric field in the COT. When an energetic particle passed through the gas, it excites and ionizes gas molecules. Under the influence of the electric field the released electrons start drifting towards the sense wires. In close vicinity of the wire the electric field accelerates the electrons, causing them to produce more electrons when hitting the gas molecules. These secondary electrons form an “avalanche”, which is registered by the sense wire. The time difference between the original  $p\bar{p}$  collision and the occurrence of the hit gives us  $r - \phi$  position of the track with respect to the sense wire.

The electrons in the COT do not drift along the electric field direction because of the presence of the magnetic field. In such crossed fields, a charge particle, initially at rest, moves at an angle  $\alpha$  with respect to the electric field lines. At COT this angle is  $\alpha = 35^\circ$  [13].

The sense wires are subdivided into 96 layers, which are organized into 8 *superlayers*, containing 12 wire layers each. The view of a quarter of the COT is shown in Figure 2.8. One can see the 8 superlayers and the end slots for the potential wires and for the sense wires. Four superlayers have the wires parallel to the axis of the detector. They are called *axial* superlayers and give us the information about  $r - \phi$  position of the track. The hits in them are called *axial hits*. The other four superlayers are tilted with respect to the axis of the detector and are called *stereo* superlayers and they provide *stereo hits*. The tilt angle of the stereo wires,  $35^\circ$ , is chosen so that the drift of the ions would be in the direction perpendicular to the wire, which ensures the best resolution. The sense wire planes are separated by gold-plated Mylar cathode field sheets. Two such sheets together with a sense wire plane in the middle are called a drift cell. The cell layout for superlayer 2 is shown in Figure 2.9. Other superlayers have similar layout.

The relative precision with which the COT determines the transverse mo-

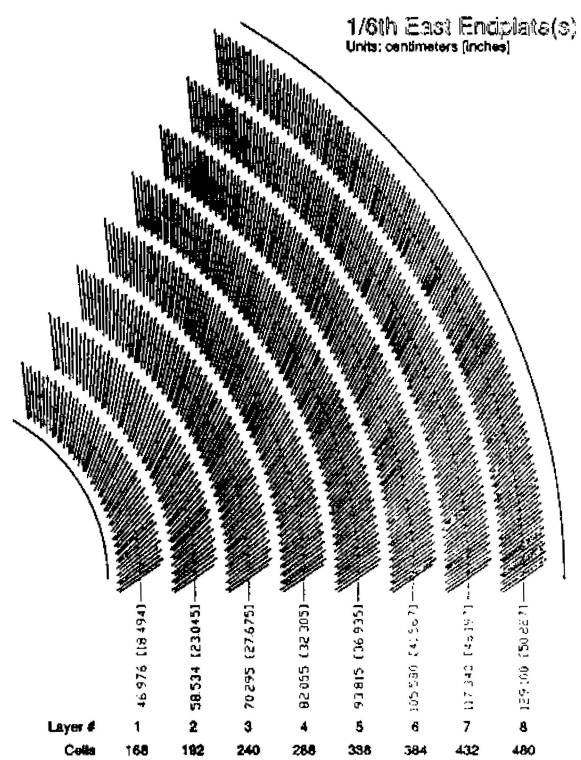


Figure 2.8: A quarter of the COT sense wires.

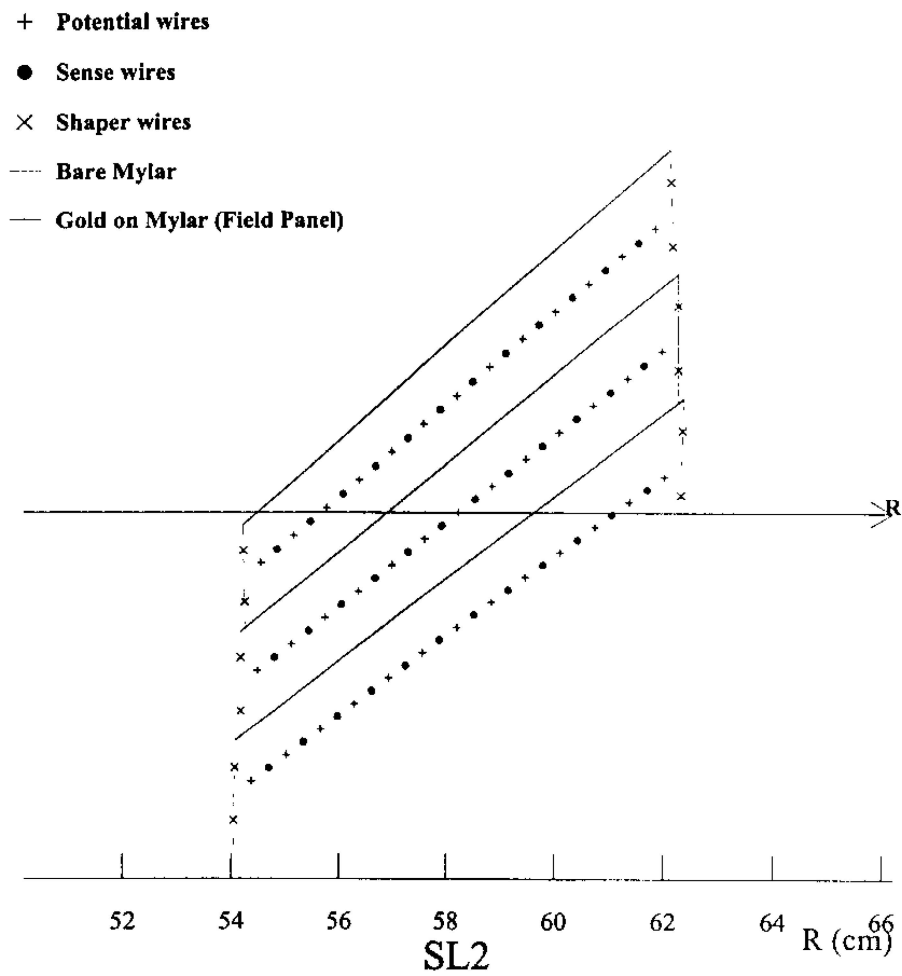


Figure 2.9: The cell layout for superlayer 2 at COT.

menta of the tracks, *i.e.* the raw momentum resolution, is given by:

$$\frac{\sigma(p_T)}{p_T} = 0.7 \oplus 0.1 \frac{p_T}{\text{GeV}/c} \%$$

### Track Reconstruction

Two different algorithms are used to reconstruct the tracks from the hits in the COT - segment linking and histogram linking. The first one looks for 3-hit seeds in each axial superlayer. The hits are fit with a straight line and all the other hits within a given distance from this line are added to the segment. The segments are linked to each other by a simple circle fit. After the  $r - \phi$  projection of the track is found, the stereo information is added, and then the final helix fit is performed.

The histogram linking algorithm also uses the 3-hit seeds. For each new hit we determine the radius of a potential track from the positions of the 3-hit seeds, the new hit itself, and the beamline. All these radii for all the hits are histogrammed and the position of the highest bin in the histogram is taken as the radius of the track helix.

The hits from the SVX are added to the tracks, found in the COT by using the so-called "Outside-In" procedure [14]. The COT track is extrapolated inside the SVX and all the silicon  $r - \phi$  hits found within the cone of a given size around the track are progressively added to the track. Every time a new hit is found, the covariance matrix of the track is updated. After all the  $r - \phi$  silicon layers are taken into account, the  $z$  information from the silicon stereo layers is added.

If there is more than one track candidate found, with different combinations of SVX hits attached to the same set of COT hits, then the track candidate with the largest number of SVX layers is chosen.

Because the energy losses are not accounted for in the tracking algorithm we have to re-fit the reconstructed tracks during the analysis with the particle hypothesis of interest. During the re-fit we drop the hits found by L00, because this system has not been fully calibrated yet.

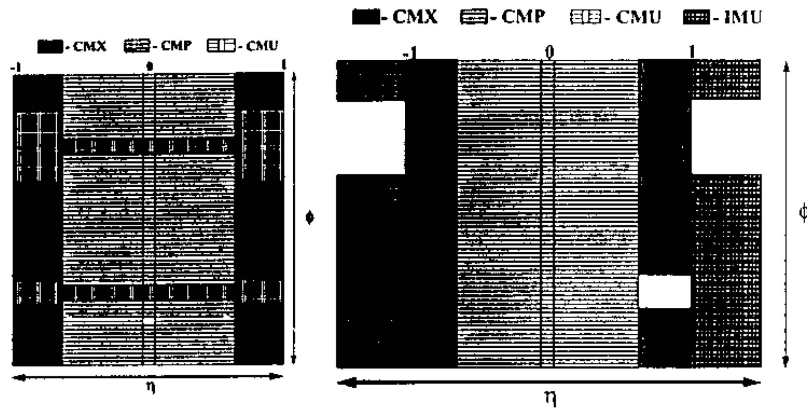


Figure 2.10: Muon coverage for Run I (left) and Run II (right).

### 2.2.3 Muon System

Muons do not interact hadronically so that they do not have to lose their energy interacting with nuclei. Muons are about 200 times heavier than electrons and their bremsstrahlung radiation is therefore about 40000 times smaller. Thus, muons can travel inside material further than any other charged particle and the muon chambers can be placed in the outermost location of the detector.

There are four systems of scintillators and proportional chambers used in CDF for muon detection: the Central MUon detector (CMU), the Central Muon uPgrade (CMP), the Central Muon eXtension (CMX) and the Intermediate MUon detector (IMU). They cover the region  $|\eta| < 2.0$ . The muon chambers in the CMP and CMX are placed together with scintillators, which are used to suppress the backgrounds coming from the interactions in the beampipe material. The scintillator systems are called CSP and CSX, correspondingly. The technical specifications of all these systems are given in Table 2.3. The pion interaction lengths and multiple scattering are quoted for a reference angle of  $\theta = 90^\circ$  in CMU and CMP/CSP, for an angle of  $\theta = 55^\circ$  in CMX/CSX and show the range of values for IMU. The Figure 2.10 displays how the coverage of the muon detectors was extended from Run I to Run II.

	CMU	CMP/CSP	CMX/CSX	IMU
Pseudorapidity coverage	$ \eta  < 0.6$	$ \eta  < 0.6$	$0.6 <  \eta  < 1.0$	$0.6 <  \eta  < 1.0$
Drift tube cross-section	$2.7 \times 6.4 \text{ cm}^2$	$2.5 \text{ cm}^2$	$2.5 \text{ cm}^2$	$2.5 \text{ cm}^2$
Drift tube length	226 cm	640 cm	180 cm	363 cm
Maximum drift time	800 ns	$1.4 \mu\text{m}$	$1.4 \mu\text{m}$	800 ns
# of drift tubes	2304	1076	2208	1728
Scint. counter thickness		2.5 cm	1.5 cm	2.5 cm
Scint. counter width		30 cm	30-40 cm	17 cm
Scint. counter length		320 cm	180 cm	180 cm
# of counters		269	324	864
Pion interaction length		7.8	6.2	6.2-20
Minimum muon $p_T$	1.4 GeV/c	2.2 GeV/c	1.4 GeV/c	1.4-2.0 GeV/c
Multiple scat. resolution	12 cm/ $p_T$	15 cm/ $p_T$	13 cm/ $p_T$	13-25 cm/ $p_T$

Table 2.3: The technical specifications of the CDF muon systems.

Muons are detected in the muon chambers by leaving small track segments, called *muon stubs*. Not all the stubs actually come from muons, some may be due to hadronic punch-throughs (hadrons getting beyond the hadronic calorimeter) or because of the noise of electronics. The stubs found are matched to the tracks previously found in the COT. To do so for each stub we extrapolate the track and the stub in the CMU or CMP is smaller than 30 cm (50 cm for CMX), this track is added to the candidate list for the stub. Then, the stub-track pair with the smallest relative distance is chosen as a muon candidate, and this track is removed from the candidate lists for all other stubs. The procedure is repeated while the stub-track pairs are available.

The shielding, provided by the parts of the detector on the way of the muons, play both positive and negative roles. The positive effect is that it gives us “clean” muons, removing all the other particles coming from the primary vertex. Among the negative effects is the fact that it does not allow muons below certain  $p_T$  threshold to reach the muon chambers. But this not a big problem, because the interesting muons, *i.e.* the muons which we are triggering upon, should have a large  $p_T$  anyway. Another negative issue is the multiple Coulomb scattering which may randomly deflect the muons from their initial trajectory. It complicates a little the procedure of stub-track matching, but the roughly gaussian and narrow mismatch can be taken into account.

Below, each of the muon systems described in more detail.

## CMU

The Central MUon detector (CMU) is placed at the radius 347 cm around the hadron calorimeter. Only muons with  $p_T$  greater than about 1.4 GeV/ $c$  can reach it. The CMU is divided into 24  $\phi$  wedges covering 15° each. The working part of the wedge covers only 12.6°, so that the CMU has 24 gaps, 2.4° each. Also, there is about an 18 cm gap between the East and the West halves of the CMU.

A wedge consists of three chambers of angular coverage 4.2°. Each of them has 16 rectangular drift cells, arranged into 4 layers, as shown in Figure X. The cells are filled with same Argon-Ethane gas mixture as the COT. The voltage on the aluminum cathodes of the cells is -2500 V, while the stainless steel sense wires are kept at +2325 V. Two of the four cell layers are oriented along a radial plane passing through the  $z$ -axis, while the other two are laid along the parallel plane, offsetted by 2 mm from the first one. The offset is measured at the midpoint of the chamber. This arrangement allows us to know on which side of the sense wires a track is, by looking at which sense wire got the signal first.

The  $z$  position of the hit on a sense wire is determined from the charge division between the ends of the wire. The resolution in the CMU chambers is about 250  $\mu\text{m}$  in the  $r - \phi$  plane and about 1 mm in  $z$ .

Reference [15] has a more detailed description of the CMU system.

## CMP

The Central Muon uPgrade (CMP) also covers the central region of the detector. It is shielded by an additional steel absorber to reduce hadronic punch-through contamination which the CMU suffers from. The path of the muons is effectively increased by the absorber to 7.8 interaction lengths. Only muons with  $p_T$  above 2.2 GeV/ $c$  can get to CMP.

The CMP approximately has a shape of a rectangular box with the walls of equal lengths in  $z$ . The  $r - \phi$  view of the CMP system is shown in Figure 2.11. Due to such shape the CMP covers the CMU's gap in  $\phi$ . For Run II the

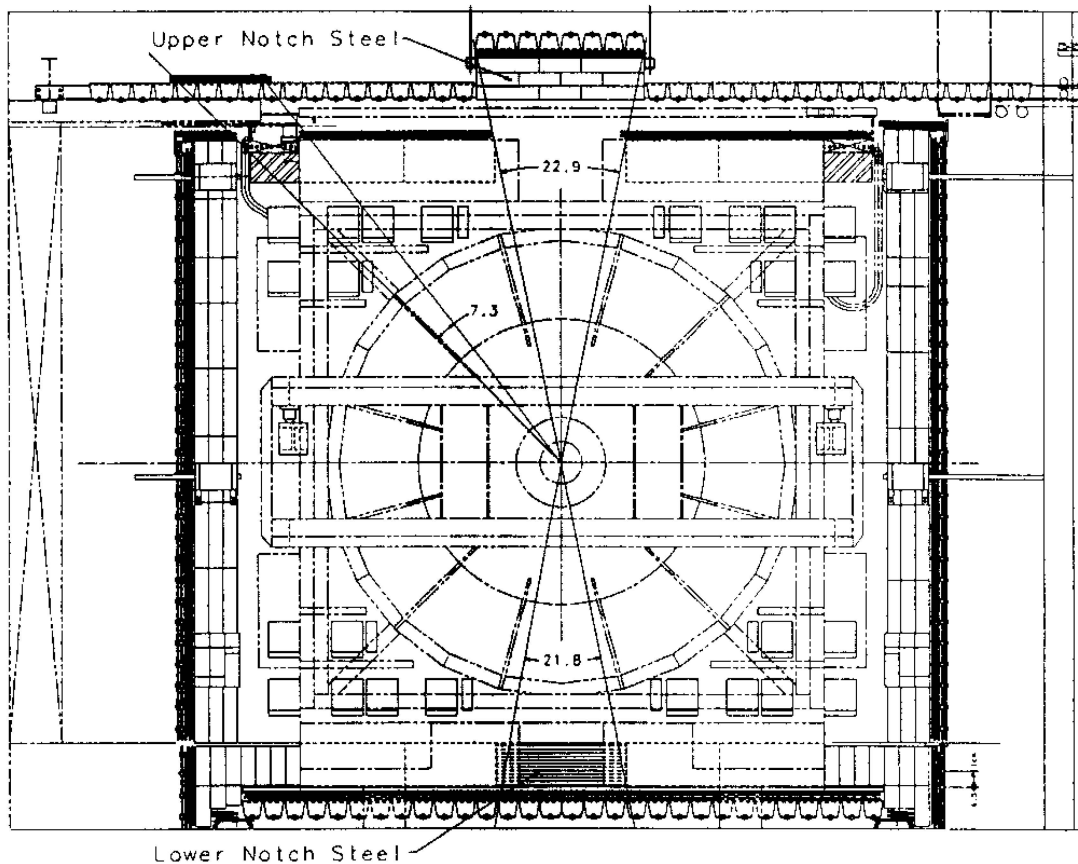


Figure 2.11: The  $r - \phi$  view of the CMP system looking at the end of the CDF detector.

CMP coverage in  $\phi$  was extended, as shown in Figure X. Both systems - CMU and CMP - help us to obtain clean muon selection in the central region of the detector.

The CMP chambers are mounted directly on the absorber. They consist of single-wire tubes  $2.5 \text{ cm} \times 15 \text{ cm} \times 640 \text{ cm}$ . Some of them are a little bit shorter to allow the cables from the inner parts of the detector go outside. The drift tubes are organized into four layers with each layer being shifted by a half-size of the tube with respect to the neighboring layers.

The CMP is described more detail in Reference [16].

## CMX

The Central Muon eXtension (CMX) consists of the wedges, forming a conical shapes on both ends of the detectors. Each wedge covers  $15^\circ$  in  $\phi$  and the range  $0.6 < |\eta| < 1.0$ . The (mentally extrapolated) apexes of the cones lie on the  $z$ -axis of the detector and the opening angle of all the cones is about  $45^\circ$ . The elevation view of the CMX system is displayed in Figure 2.12. The IMU barrel chambers and scintillation counters, the toroid counters, and the endwall counters are also shown. In the Run I CMX had a  $30^\circ$  gap at the top on the West end and  $90^\circ$  gap at the bottom in both East and West ends. The first gap was created to make space for the liquid helium lines and the second gap was due to intersection of the conical section with the collision hall floor. For Run II both these gaps are covered by KeyStone and MiniSkirt additions to CMX. The KeyStone consists of two more CMX wedges, while the MiniSkirt has a little bit different geometry, shown in Figure 2.13.

The CMX chambers consist of the same tubes as in CMP with only the length of the tubes being different: 180 cm. Each wedge in the CMX has 48 tubes arranged in 8 layers, each layer has 6 tubes. The layers are staggered so that there are at least 4 tubes in any coverage in  $\phi$ . Figure X shows the arrangement of the CMX tubes. The layers are placed at a slight stereo angle, which allows for the measurement for the  $z$  coordinate.

More information on the CMX can be found in Reference [16].

## IMU

The Intermediate MUon detector (IMU) covers the region  $1.0 < |\eta| < 2.0$  with fine granularity. It was introduced to complement ISL in the reconstruction of the tracks with  $|\eta| > 1.0$ .

The IMU's drift chambers and counters are placed around the steel toroids on the both ends of the CDF. There are additional counters between the toroids. The detailed section in the IMU Barrel is shown in Figure 2.14 and the complete elevation by view of the IMU system - in Figure 2.15. The IMU chambers and scintillators are represented by the outer circle around the

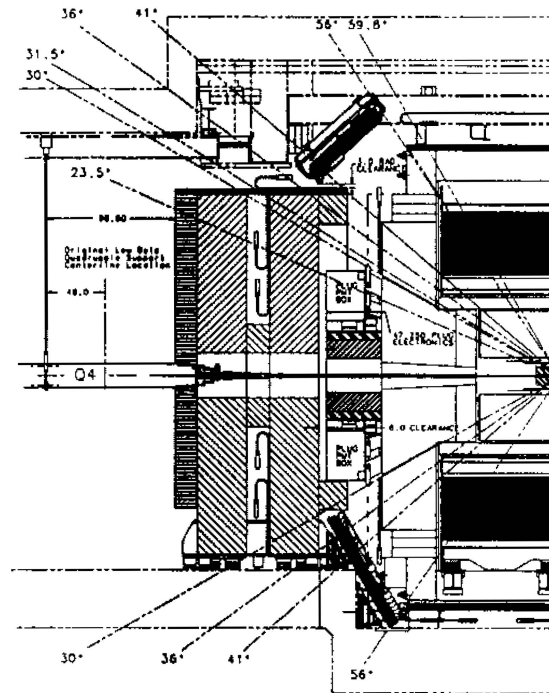


Figure 2.12: The side view of the CDF showing the CMX coverage. The dark blocks spanning between  $30^\circ - 40^\circ$  and  $56^\circ$  are the CMX wedges.

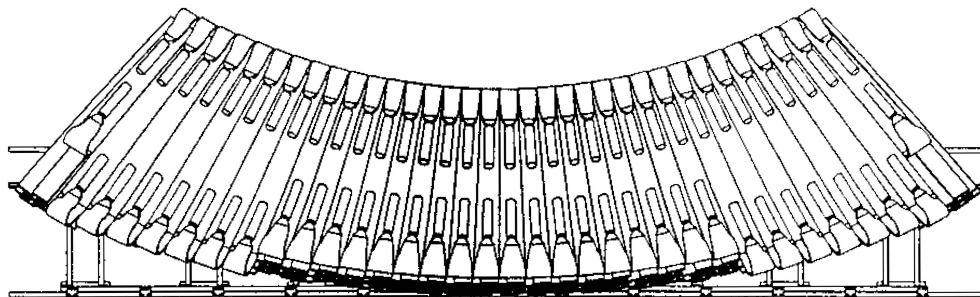


Figure 2.13: The MiniSkirt portion of the CMX system.

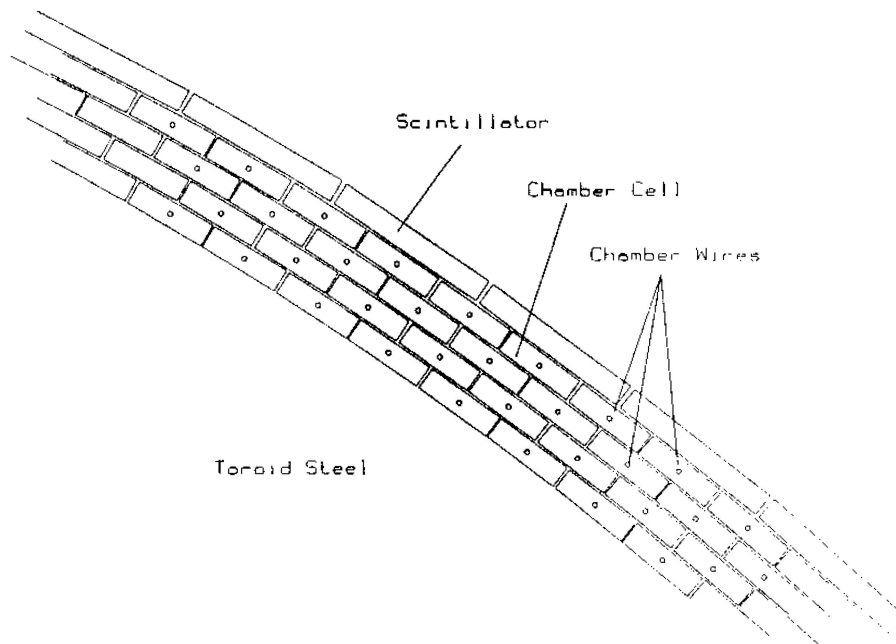


Figure 2.14: A detailed section of the IMU Barrel.

toroids. The CMX lower  $90^\circ$  section is also shown. The chambers and counters used in the IMU are the same as those in CMX and CMP, and the electronics is the same too. Reference [17] provides further information on the IMU.

The dimuon trigger was not available for this system at the time when the data for this thesis was collected. For this reason, the IMU is not used in our analysis.

#### 2.2.4 Other Systems

The other systems in the CDF include the Time-of-Flight (TOF), the calorimetry and the Cherenkov Luminosity Counters (CLC). They are not used in this analysis, so we will present only a short description.

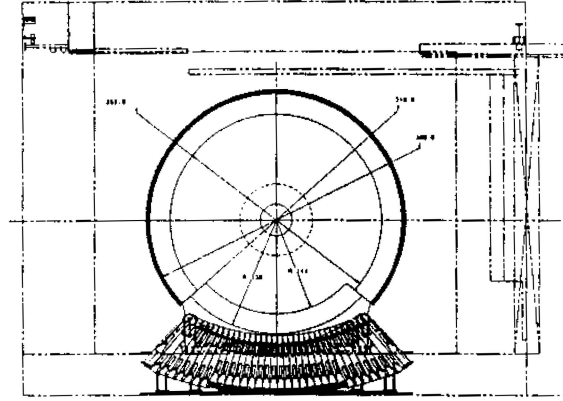


Figure 2.15: The elevation view of the Imu Barrel (thick dark line). The Miniskirt part of the CMX is shown too.

### Time-of-Flight

The Time-of-Flight (TOF) system surrounds the COT. It serves to determine the masses  $m$  of particles, and thus identify it, with the formula:

$$m = \frac{P}{\gamma\beta c} = \frac{P}{\beta c} \sqrt{1 - \beta^2} = \frac{P}{c} \sqrt{\frac{1}{\beta^2} - 1} = \frac{P}{c} \sqrt{\frac{(ct)^2}{L^2} - 1}, \quad (2.5)$$

where  $t$  is the time passed from the collision moment,  $L$  is the path length and  $P$  is the momentum of the particle.

The TOF system is located between the COT and the solenoid magnet. at a radius of 138 cm. It consists of 216 scintillator bars  $4 \text{ cm} \times 4 \text{ cm} \times 279 \text{ cm}$ . These bars cover the region  $|\eta| < 1.0$ . When a particle passes through a bar, the photons from ionized molecules travel to both ends of the bar, where they are detected by fine-mesh photomultiplier tubes. The travel time of the photons determines the position at which particle crossed the tube. These tubes can operate inside the magnetic field of 1.4 T, created by the solenoid.

The ability of the TOF system to distinguish particles of different mass

(*separation power*) is illustrated in Figure 2.16. The time difference between kaons, pions and protons over path of 140 cm as a function of momentum, expressed in terms of picoseconds (left scale) and the separation power  $\sigma$  (right scale) assuming a time resolution 100 ps. This is close to the real value of  $\sim 120$  ps. The dashed line show the separation between kaons and pions obtained from the energy loss measurements ( $dE/dx$ ) in the COT.

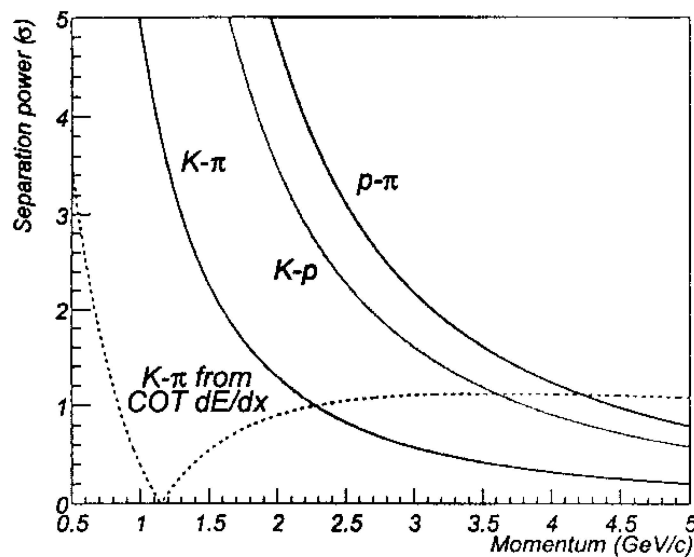


Figure 2.16: The Time-of-Flight performance.

## Calorimetry

The TOF system is surrounded by an electromagnetic calorimeter, which, in turn, is surrounded by a thicker hadron calorimeter. Geometrically the calorimeters are divided into central, wall and plug parts. They are called, correspondingly: the Central ElectroMagnetic (CEM), the Central HAdron (CHA), the Wall HAdron (WHA), the Plug ElectroMagnetic (PEM) and Plug HAdron (PHA) calorimeters.

All the calorimeters in CDF are *sampling* calorimeters, which means that

they consist of alternating layers of absorber and scintillator. The absorber is necessary to make the passing particle create a shower, while the scintillator gives us the signal, read out by phototubes. The CEM and PEM use lead as the absorber.

The central parts cover the region  $|\eta| < 1.1$  for EM and  $|\eta| < 1.3$  for hadron calorimeters. They are divided into towers of equal size:  $15^\circ$  in  $\phi$  and 0.1 in  $\eta$ . The plug calorimeters extend down to  $\eta = 3.6$  and have variable segmentation. The schematic view of the plug calorimeters is shown in Figure 2.5. and the cross-section in Figure 2.17.

Both the CEM and PEM have electromagnetic strips called CES and PES, respectively. These are gas proportional chambers with the wires inside being perpendicular to the strips outside. This configuration allows us to measure both  $\phi$  and  $z$  coordinates of the particle shower. The spatial resolution is about 2 mm in both direction for the CES and about 1 mm for the PES.

The CES and PES are located inside the calorimeters, to give us the transverse shower profile measurement at the plane where it is the largest, *i.e.* at the depth of about 6 radiation lengths  $X_0$ . They measure the position of the shower, so that it could be matched to the COT tracks. This way electrons can be distinguished from photons and neutral pions.

The CEM is preceded by a Central Preshower (CPR) multiwire proportional chamber. It was introduced because of the delayed initiation of  $\gamma$ -showers. The PEM has no such chamber, only its first scintillator layer, called PPR, is much thicker than the others, and has an individual read out.

The hadron calorimeters are located after the electromagnetic calorimeters. They use iron as the absorber which makes the incident hadrons create showers. The hadron and electromagnetic calorimeters are similar, differing from each other mainly by the depths. The basic properties of the calorimeters are given in the Table 2.4.

More information about calorimetry in CDF can be found in Reference [17] and [18].



### Luminosity Counters

The Cherenkov Luminosity Counter (CLC) serves to determine the instantaneous luminosity  $\mathcal{L}$  of the Tevatron at the CDF interaction point by the formula:

$$\mathcal{L} = \frac{\mu \cdot f_{bc}}{\sigma_{p\bar{p}}}, \quad (2.6)$$

where  $\mu$  is the average number of interactions per bunch crossing,  $f_{bc}$  is the rate of the bunch crossing at the Tevatron and  $\sigma_{p\bar{p}}$  is the total  $p\bar{p}$  cross-section at  $\sqrt{s} = 1.96$  TeV, scaled to this energy from the results of the previous measurements [19].

According to Poisson statistics, the probability to have an empty bunch crossing, *i.e.* a bunch crossing with no  $p\bar{p}$  collisions, is  $P = e^{-\mu}$ . The CLC actually measure the number of such empty bunch crossings. This measurement is based on the well-known Cherenkov effect: a charged particle traveling in some media with a speed higher than the speed of light in this media radiates light in a narrow cone around its direction. If the total amount of the collected light is below a threshold, the CLC counts it as an empty crossing. The measured fraction of these crossings, corrected for the CLC acceptance, is used to calculate  $\mu$ .

The Cherenkov counters are located in the gaps of the Plug Calorimeter, between the Plug Calorimeter and the beamline. They are directed towards the interaction point, so that the particles coming from this point would generate the largest amount of light into the counters. The time resolution of the CLC system is about 50 ps, which makes it possible to distinguish between particles coming from different interaction. The precision of the luminosity measurement at CDF is about 5%.

More details about the CLC may be found in Reference [20].

#### 2.2.5 General Triggering

The proton and antiproton bunches cross in the Tevatron every 396 ns at CDF. At the current luminosity of about  $10^{31} \text{ cm}^{-2}\text{s}^{-1}$  we have approximately

one  $p\bar{p}$  interaction per bunch crossing. This means that 2.5 million events are produced at CDF every second. Recording all of these events would require an enormous data throughput of 250 GBytes/sec (assuming an average size of an event of 100 KB). It is not only not possible to achieve this rate with existing technology, but it is also not desirable to do so. Even if we managed to record all these data, it would take a very long time to analyze it afterwards. To make the data throughput and the size of the data samples reasonable, we have to somehow select and write to tape only the most interesting events, letting all the others go unrecorded. To decide which events are the most interesting, we look for the specific signatures, such as high  $p_T$  tracks, leptons, jets etc. To do so on-the-fly, a special trigger system was built. Ideally this system has no deadtime, which means that there is no situation when an event can not be recorded because the previous one is still being processed. This is achieved by having three trigger levels (Level-1, Level-2, Level-3), connected with buffered pipelines. The block scheme of the data acquisition (DAQ) and trigger system at CDF is shown in Figure 2.18.

The Level-1 trigger has only  $5.5 \mu\text{s}$  to make a decision about each event. On average, it accepts only one event out of 250, bringing the event rate down to about 10 KHz. The accepted events go further to Level-2. Level-2 has a little bit more time to decide, about  $20\text{-}30 \mu\text{s}$  per event. If Level-2 accepts the event, the whole detector is read out, and the event goes further, to the Event Builder and Level-3. The event rate at this point is about 200-300 Hz. In the Event Builder the data fragments from the different parts of the detector are collected into a single event record, which is submitted to the Level-3. At Level-3, the event is reconstructed and, again, is considered for possible rejection. Level-3 accepts about one event out of 4. The accepted events are transmitted to the mass storage devices at a rate of approximately 75 Hz and get written on a tape.

Below all three levels of the CDF trigger discussed in more detail. Even more information can be found in Reference [17] and [21].

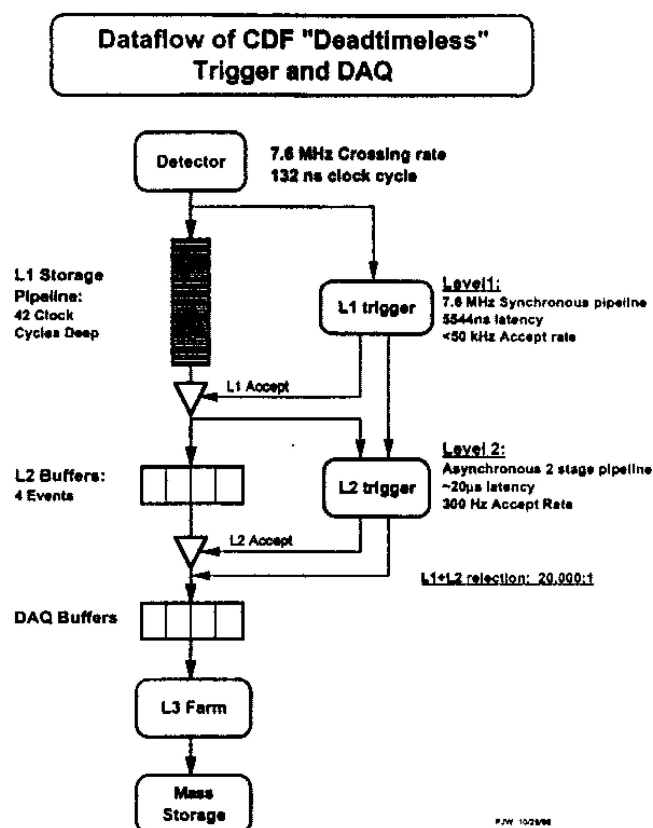


Figure 2.18: The trigger and DAQ system functional block diagram.

### Level-1

As was mentioned earlier, Level-1 trigger has only  $5.5 \mu\text{s}$  to accept or reject an event. Therefore, it can not do the detailed reconstruction of COT tracks and muon stubs or obtain the details of showers in the calorimeters. Instead, it uses some very crudely reconstructed versions, which are called *primitives*. For example, for the muon stubs we only know which muon chamber has the stub, the stub position and slop are not measured. The moun or calorimeter primitives, being combined with the track primitives give us electrons, muons and jets, which we can trigger upon.

The full list of trigger algorithm can be found in Reference [22]. The most important trigger for this analysis is so-called dimuon trigger based on

detecting two muons in the event.

### XFT and XTRP

The eXtremely Fast Tracker (XFT) uses information from only 4 axial superlayers of the COT to identify high- $p_T$  track primitives in the  $r - \phi$  plane. To do so the hits from the COT are separated into two classes, according to their drift time: *prompt* hits with the drift time less than 44 ns and *delayed* hits with longer drift time. Then the hit pattern in the event is compared to a predefined set of patterns for both prompt and delayed hits. This predefined set of patterns helps to find the segments of high- $p_T$  tracks coming from the beamline very fast. For all the found segments the information about the charge, curvature and the  $\phi$  position at the COT superlayer 6 is kept. Then the segments which look like they came from the same track are linked together into the track primitive. Of course, the parameters of the track primitive are estimated very crudely, given the short time which XFT has for this. The information about the found track primitives is given to the eXTRaPolator unit (XTRP) and Level-2.

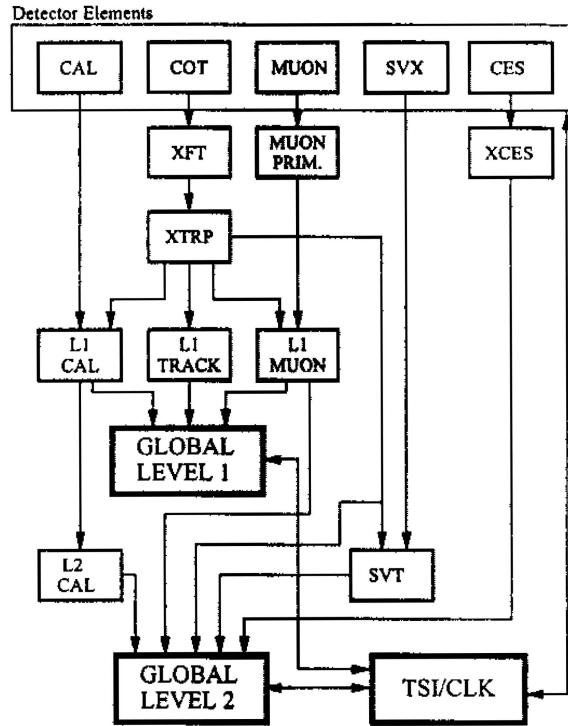
The XTRP matches the track primitives from XFT with the muon and calorimeter primitives. A detailed description of this matching utilized in dimuon trigger is given in Section S. XTRP also uses a predefined set of patterns to speed up the matching.

The detailed information about XFT and XTRP logic is available in Reference [23] and [24].

### Level-2

The event accepted by Level-1 go to Level-2 for the further processing. The Level-2 uses the primitives from the Level-1 plus some additional information from the calorimetry and from the SVX (see Figure 2.19). The information about  $r - \phi$  hits from the SVX is used to extrapolate the SFT track primitives inside SVX and to determine the tracks impact parameter,  $d_0$ . Some triggers look for tracks with high  $d_0$ , *i.e.* for the events with *displaced vertex*. This

### RUN II TRIGGER SYSTEM



P/W 9/23/96

Figure 2.19: The CDF trigger-system block diagram.

capability was introduced in Run II.

If the event is accepted, the primitives, constructed at Level-2 are submitted further, to the Event Builder and Level-3.

#### Event Builder and Level-3

In the Event Builder system the event fragments from the different parts of the detectors are put together and go further as one whole piece. This is done with the aid of an Asynchronous Transfer Mode (ATM) network switch, which takes the event fragments from Level-2 VME crates, puts them in the proper places and then feeds them to the Level-3 (see Figure 2.20).

The Level-3 consists of 292 computers. They are subdivided into 16 groups (subfarms) of 16-18 computers in each. One computer in each subfarm serves as a *converter node*, accepting the data from the Event Builder and directing it to one of the other computers in the subfarm (*processor node*) for the analysis. The accepted events go to the *output node* and then further to the mass storage device. Each output node is shared by two subfarms.

The processor nodes transform the event fragments into a united event record, which has all the information about the event from all the parts of the detector. The Level-1 and Level-2 have to deal with crudely reconstructed primitives because of lack of time. The Level-3 has enough time to fully reconstruct tracks, muons, electrons, jets, *etc.* and to apply the final trigger decision about each event.

More information about the Event Builder and Level-3 is available in Reference [25].

## 2.2.6 Dimuon Trigger

The dimuon trigger at CDF looks for events with two muons. One of the muons should be from the CMU, another can be either from the CMU or from the CMX. Let us first consider the case when the second muon also comes from the CMU. For this scenario the trigger is called "L1\_TWO\_CMU\_PT1.5", because only muons with  $p_T > 1.5 \text{ GeV}/c$  can get to the CMU.

The muon chambers in the CMU are organized in stacks of four. Each end of the detector has 288 such stacks. The stack may have a stub - a track segment in which the hits in the cells 1 & 3 or cells 2 & 4 are separated in time by no more than 396 ns. The adjacent stacks are logically assembled into pairs, called *towers*. If at least one stack in the tower has a stub, the tower has fired. Otherwise, the tower is empty.

The information from muon chambers is linked to the tracking information as follows. First, the XFT reports the charge,  $p_T$  and  $\phi$  (measured at the 6th COT superlayer) of the tracks to the XTRP. The latter extrapolates the tracks (assuming they came from the beam line) to the inner radius of the

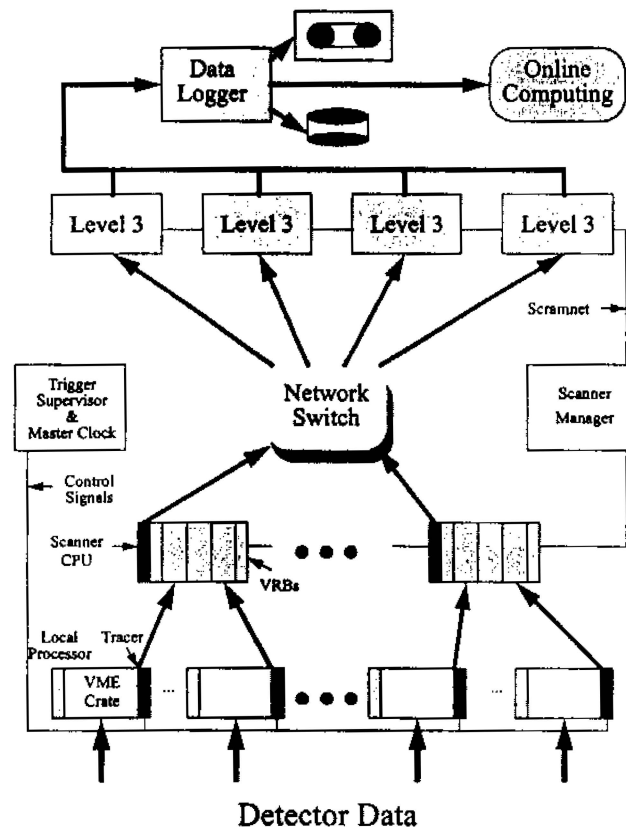


Figure 2.20: The block scheme of the Event Builder and Level-3 system.

CMU - 347.8 cm. The multiple scattering in the detector material leads to an uncertainty in the determination of the position of the track at this radius. So that, for each track a  $\phi$  window is determined, where the track could end up with 99.5 % ( $3\sigma$ ) probability. This window in  $\phi$  is called a *footprint*.

If a fired CMU tower is covered by at least one track footprint, it is called *muon tower*. The event gets accepted by Level-1 dimuon trigger if it has at least two muon towers. These towers, though, must be separated by at least two other towers (which may or may not be empty), or to be on the different ends of the detector. If the muon towers are separated by a  $2.4^\circ$  gap between CMU wedges, this is also counted as a tower. This requirement ensures that there is a separation in  $\phi$  between the two muons.

If one muon in the event comes from the CMU while another muon comes from the CMX, the trigger has a different name, “L1\_CMU\_PT1.5\_CMX\_PT2.2”, which reflects the fact that only muon with  $p_T > 2.2 \text{ GeV}/c$  can reach CMX. Another different is that the CMU and CMX muon towers require no separation in  $\phi$ . There is no requirement for the muons to be of the opposite charge at Level-1.

Reference [26] gives more information about the Level-1 dimuon trigger. Figure 2.21 shows the mass spectrum of the muon pair obtained with different triggers in CDF. The described here dimuon trigger is called “JPsi” on this plot.

Level-2 does not imposed any additional cuts on the dimuons, and the events accepted by Level-1 trigger proceed directly to Level-3. At Level-3 the muons are required to have opposite charge. The invariant mass of both muons should be between  $2.7 \text{ GeV}/c^2$  and  $4.0 \text{ GeV}/c^2$  (selecting  $J/\psi$  and  $\psi(2S)$ ), the difference in  $z_0$  should be smaller than 5 cm and the opening angle between them less than  $130^\circ$ .

## 2.3 Offline Data Handling

The data obtained from the Level-3 are split into ten “streams” which are called by first ten letters of the alphabet: “A”, “B”... “J”. The events passing the requirements of the dimuon trigger go into the stream “J”. These events are written to tape in real time mode, *i.e.* online. Further manipulations of the data are performed offline. The data on the tape is written in the form of the raw data banks from different parts of the detector. One needs to unpack these banks and produce the objects for actual physics analysis, such as tracks, muons, electrons, etc. This procedure is called *production*. The data for this analysis was produced with a production version 5.3.1. The data after the production is split into so-called *datasets*, containing the events satisfying a particular set of trigger requirements. These datasets are given to the end users to do the physics analysis. There are 35 datasets in CDF. This analysis is done

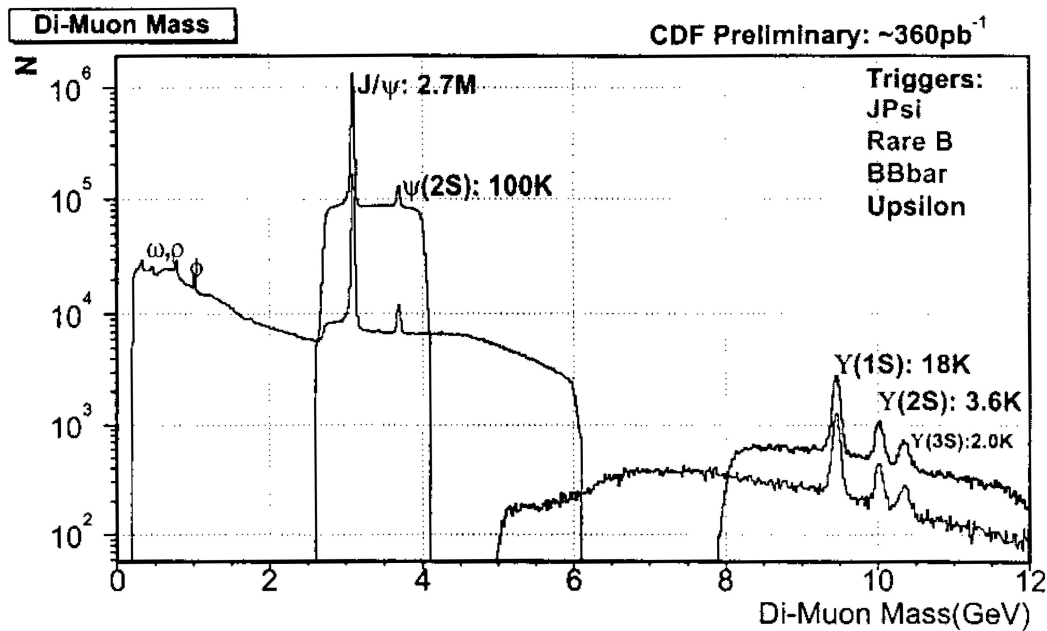


Figure 2.21: The mass spectrum of muon pairs obtained via different triggers at CDF. The dimuon trigger used in this analysis is called “JPsi”.

with `jpm0c` dataset, which contained the events with dimuon candidates found by the detector. The events in this dataset are “stripped” by removing the banks and objects not needed for the further analysis. The compressed version of our dataset is called `xpm0c`. The stripping greatly speeds up the analysis, because much of the time is usually taken reading the data files, rather than actually processing the data. The stripped data is subject to a further reduction by applying some loose cuts. This called *skimming*. The skimmed data files contain mostly the interesting events and it takes quite a short time to apply tighter cuts to them and extract the final results.

The amount of data in the final datasets is usually measured not in the number of events, but rather in the inverse units of the cross-section. In this way the users can multiply the size of the dataset by the cross-section of the process they are interested in to obtain the expected number of the events of this type in the dataset. The total size of the dataset used for this analysis is

about  $220 \text{ pb}^{-1}$ .

## Chapter 3

# Data Sample and Signal Selection

In order to conduct the desired studies of  $B$  mesons we need to isolate the events of interest, *i.e.* *signal*, from the multitude of other events occurring in the detector, commonly referred to as *background*. Unfortunately, such isolation cannot be perfect and a certain amount of background makes its way into the sample. The primary implication is that we have to find an appropriate description (in terms of mass, momentum and signed decay length, etc.) of the background, which is necessary to prevent the background from affecting the extraction of the signal properties.

Having accepted the inevitable presence of the background in the sample, one needs to choose optimal selection, usually in terms of boundaries, also known as *cuts*, on certain quantities characterizing the events, such that the uncertainty on the extracted parameters of interest is minimized. Often making optimal selection does not translate into minimizing the amount of background, because of the two facts: first, once there is some background it may be beneficial to have a substantial amount of it such that its properties can be adequately modeled; second, using cuts to reduce the amount of background also reduces the amount of signal, such that the overall statistical power is diminished.

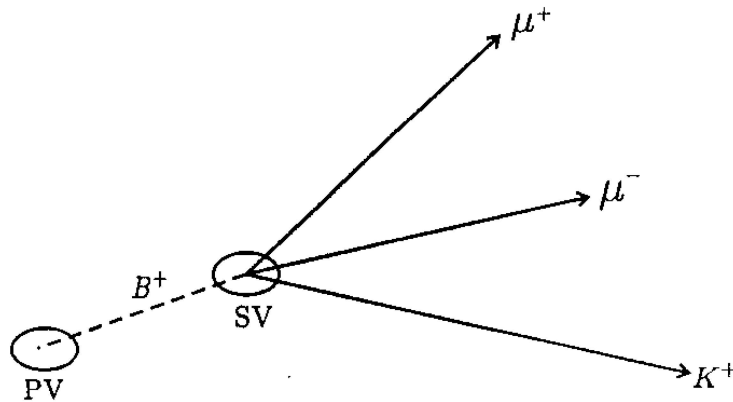


Figure 3.1: The topological  $B^+ \rightarrow J/\psi K^+$  diagram of decay.

Another general analysis issue is related to the fact that all events (signal and background) are observed through a detector. A relevant analogy here would be looking at some small extra-terrestrial object of unknown nature with a lens that has spherical, chromatic and all other known aberrations plus, perhaps, some unknown ones instead of an ideal aberration-free lens. This is to say that not only detectors have a finite resolution, but also they give a distorted view of events they register. One of the major goals of the analysis is to unfold these distortions and/or minimize them. The remaining distortions need to be quantified and included into the uncertainty on the measured quantities.

To measure the ratio of branching fractions,  $\mathcal{B}(B^+ \rightarrow J/\psi\pi^+)/\mathcal{B}(B^+ \rightarrow J/\psi K^+)$ , we reconstruct  $B^+ \rightarrow J/\psi K^+$  decays where  $J/\psi$  decays to  $\mu^+\mu^-$ . The topological diagram of these decay modes is shown in Fig 3.1. In this chapter we present the data sample we use and the reconstruction procedures of  $B^+ \rightarrow J/\psi K^+$ .

### 3.1 Data Sample

The particular decay channel we are looking at is  $B^+ \rightarrow J/\psi K^+$ , where  $J/\psi$  decays to  $\mu^+\mu^-$ . It is reconstructed from the `xpmm0c` data set explained in Section 2.3. This analysis is limited to the inclusive run range 138809-168889.

These runs were recorded in the period from February 9, 2002 to September 6, 2003. Only “good runs” have been selected. A run is considered to be good for a particular analysis if all relevant detector systems operated normally during this run as determined by the experts. The particular good run definition used in the current analysis, although not extremely meaningful for people outside of the CDF Collaboration, is given in Appendix X. The data samples considered in this analysis correspond to the total integrated luminosity of  $220 \text{ pb}^{-1}$ .

In  $p\bar{p}$  collisions at  $\sqrt{s} = 1.96 \text{ TeV}$  with the trigger requirements we have, at least 80% of the  $J/\psi$  are from prompt  $c\bar{c}$  production, while not more than 20% are coming from  $B$  decays [27]. This is main reason why the `xpmm0c` data set, though compressed, is still rather bulky to deal with on a daily basis. To overcome this hurdle we have created skimmed sample of interest candidate. In preparing a skim the selection code is run without the most detailed calibrations, but with loose requirements, such that nothing that can potentially pass the subsequent strict analysis cuts is excluded. In preparing the skimmed sample, we use the following requirements:

- $p_T(\mu) > 1.4 \text{ GeV}/c$
- $2.8 < M(\mu^+\mu^-) < 3.4 \text{ GeV}/c^2$

After the skimmed sample is prepared the most complete and accurate version of the selection code is run. This final version of the analysis code uses the best available calibrations. It also has the most detailed and accurate procedures, such as those described in the followed sections, tuned on.

## 3.2 Track Preparation

After the basic algorithm of the track reconstruction has been performed there are a number of additional refinements to the track parameters introduced for the analysis. Some of them are perform during the production stage. Others, are done in a special module called `TrackRefitter` [28, 29] which is applied

during the analysis stage. This module takes the raw tracks from COT and refits them introducing the necessary changes.

During the track reconstruction at the production stage, the hits coming from the L00 are not included in the fit, because this tracking subsystem was not yet completely calibrated at the time when this analysis was performed. The **TrackRefitter** also excludes the L00 hits from the fit. Though this is not a change with respect to the production stage, it is an important part of the track treatment at CDF, and we mention it here.

Another feature of the track reconstruction at CDF is the correction of the track parameters for the small non-uniformities in the magnetic field produced by CDF solenoid, which were well known from Run I [30]. Another effect, related to the magnetic field, is the correction for the nominal value of the field. To take these effects into account, the magnetic field was measured in different places in the solenoid and the data was fit with smooth functions to provide the field map for the whole CDF detector. The full magnetic map is taken into account during the track reconstruction. This correction is performed for all the tracks during production stage.

The parameters of the tracks in CDF are calculated with respect to the detector coordinate system with the origin in the center of the COT (Section 2.2.1). To obtain a consistent picture from both the COT and the SVX, one needs to take into account possible angular and translational misalignments between the COT and the SVX coordinate systems. These misalignments are found empirically and are corrected for during the track reconstruction. This is mostly done during the production stage and after this we only introduce small corrections for the refinements obtained after the production has run.

And the last, but probably the most important, correction is the correction for the energy loss in the detector material. The CDF detector appears to have more material than it should according to *a priori* tabulations. To obtain the correct parameters of the track one needs to take into account all this material. This is achieved by introducing into GEANT simulation of the detector a number of special cylindrical layers of silicon, so that the integrated effects of

the additional detector material on the passing particles would be simulated [28, 29, 30]. The widths of these layers are tuned, so that the Monte Carlo track parameter distributions correspond to that of the tracks in the data. During the production stage the parameters of the tracks are corrected for the presence of these layers, assuming the mass of a charged pion for these corrections for other mass assignments - charged kaon, proton, muon *etc.*

To select only good quality tracks for the analysis we require each track to have  $r - \phi$  hits at least three distinct SVX layers. As for the COT we require each track to have at least 20 and 16 hits at the axial superlayer and the stereo superlayer each. These cuts are summarized in Table 3.1.

### 3.3 Muon Preparation

The muons in CDF consist of muon stubs from the muon system (CMU, CMP *etc*) matched to COT tracks. These tracks must be the trigger tracks, *i.e.*, the XFT must have found them. Though, in our analysis we do not verify explicitly that the muons in the sample satisfy the trigger. Also these tracks must be good tracks described above.

We require that in the muons reported by the CMU the stub and the COT track have the matching  $\chi^2 < 9$ . The muons found in CMP and CMX do not have this requirement, because of the much lower level of noise. Also, there is a cut on the offline  $p_T$  of the muons, reconfirming the cut imposed by the XFT,  $p_T > 1.5 \text{ GeV}/c$ . These cuts are summarized in Table 3.1.

### 3.4 $J/\psi$ Reconstruction

In our dataset only those events are present which have been collected via the dimuon trigger, *i.e.* which have two muons of the opposite charge satisfying the trigger cuts. These two muons are required to form a  $J/\psi$  candidate. The muon tracks in this candidate are forced to come from a common vertex in three dimensions. The parameters of these tracks are adjusted accordingly.

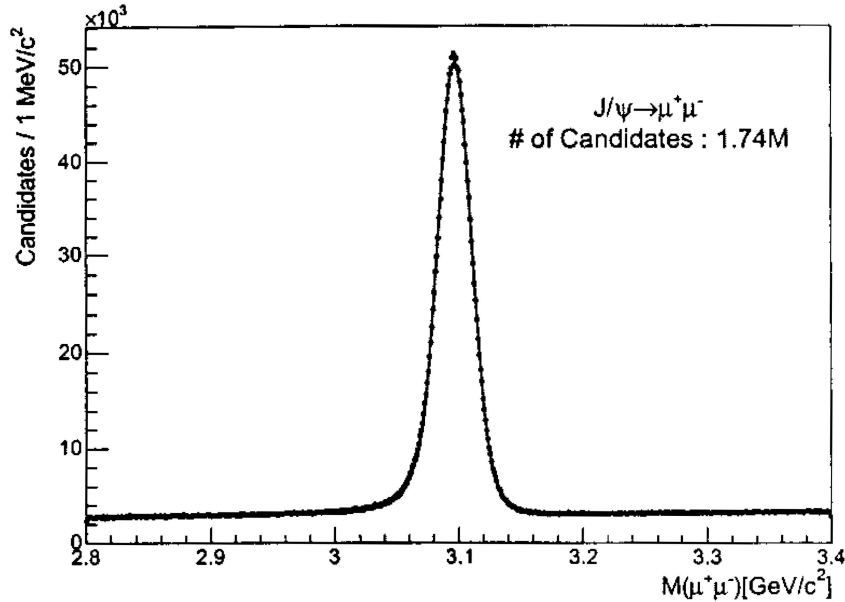


Figure 3.2: The invariant mass distribution of  $J/\psi \rightarrow \mu^+\mu^-$  with likelihood projection overlaid. Signal is modeled with two Gaussians and background is modeled with a 1st order polynomial function.

The mass of the  $J/\psi$  candidate is required to be within a window of  $\pm 80 \text{ MeV}/c^2$  around the nominal  $J/\psi$  mass  $3096.87 \text{ MeV}$  from the PDG [31]. To have a high-quality  $\mu^+\mu^-$  vertex we reject the track combinations which failed the vertex fit. The full list of cuts applied to the  $J/\psi$  candidates is given in Table 3.1 and the mass distribution is shown in Figure 3.2.

### 3.5 $B^+$ Reconstruction and Selection

$B^+$  meson reconstruction is founded on the successful reconstruction of  $J/\psi$  mesons. The  $B^+$  meson of interest for this analysis is found through  $B^+ \rightarrow J/\psi K^+$  decay mode. The  $J/\psi$  mesons are reconstructed from oppositely charged muon pairs (see above section). Since CDF does not have particle identification in our momentum range, we consider all other charged tracks to

Cut	Description	Value
Track quality	Number of SVX layers with a hit in $r - \phi$ plane	$\geq 3$
	Number of hit in COT axial SL	$\geq 20$
	Number of hit in COT stereo SL	$\geq 16$
Muon quality	$\chi^2$ for track-stub match (CMU only)	$< 9.0$
	$p_T(\mu)$	$> 1.5 \text{ GeV}/c$
$J/\psi$	Mass window, $ M(\mu^+\mu^-) - M_{J/\psi}^{PDG} $	$< 80 \text{ MeV}/c^2$

Table 3.1: The  $J/\psi$  selection cuts.

be kaons for  $B^+ \rightarrow J/\psi K^+$  reconstruction. Then, kaon and two muons are constraint to a 3-D vertex point using CTVMFT [32]. A mass constraint to the known  $J/\psi$  mass value [31] is also imposed on the dimuon pair.

Several requirements (*i.e.* cuts) are placed on the three-track combination, which is a  $B^+$  meson candidate. These requirements are imposed to enhance the statistical significance of the signal compared with background, mostly composed of prompt  $J/\psi$  mesons and  $J/\psi$  mesons from  $B$  decays. The cuts are take advantage of two natural difference between actual  $B$  mesons and backgrounds. The first difference which we exploit is the “harder” production of  $B$  mesons.  $B$  mesons tend to have larger transverse momentum than backgrounds. We therefore require

- $p_T(B^+) > 6.5 \text{ GeV}/c$

The second difference we exploit is the long lifetime ( $\sim 1.5 \text{ ps}$ ) of the  $B^+$  relative to the most prompt (short-lived) background. We take advantage of this by requiring that the two-dimensional displacement between the primary and secondary vertices, projected along the  $B^+$  meson’s momentum,  $L_{xy}$ , be larger than  $200 \mu\text{m}$ .

- $L_{xy} > 200 \mu\text{m}$

Generally the tracks originated from  $B$  meson decay have harder transverse momentum than that of combinatorial background. So we require the  $p_T$  of kaon to be greater than  $2.0 \text{ GeV}/c$ .

- $p_T(K^+) > 2.0 \text{ GeV}/c$

To ensure good vertex quality, we require the probability of  $\chi^2$  at  $r - \phi$  plane, which is calculated at CTVMFT, should be greater than 0.1%.

- $\text{prob}(\chi_{r\phi}^2) > 0.1\%$

Figure 3.3 shows the invariant mass distributions of  $M(\mu^+\mu^-K^+)$  and  $M(\mu^+\mu^-\pi^+)$ . Especially, pion hypothesis is assigned to the third track in bottom plot. It shows the large reflection from  $B^+ \rightarrow J/\psi K^+$  signals caused by misassignment of mass to the third track.

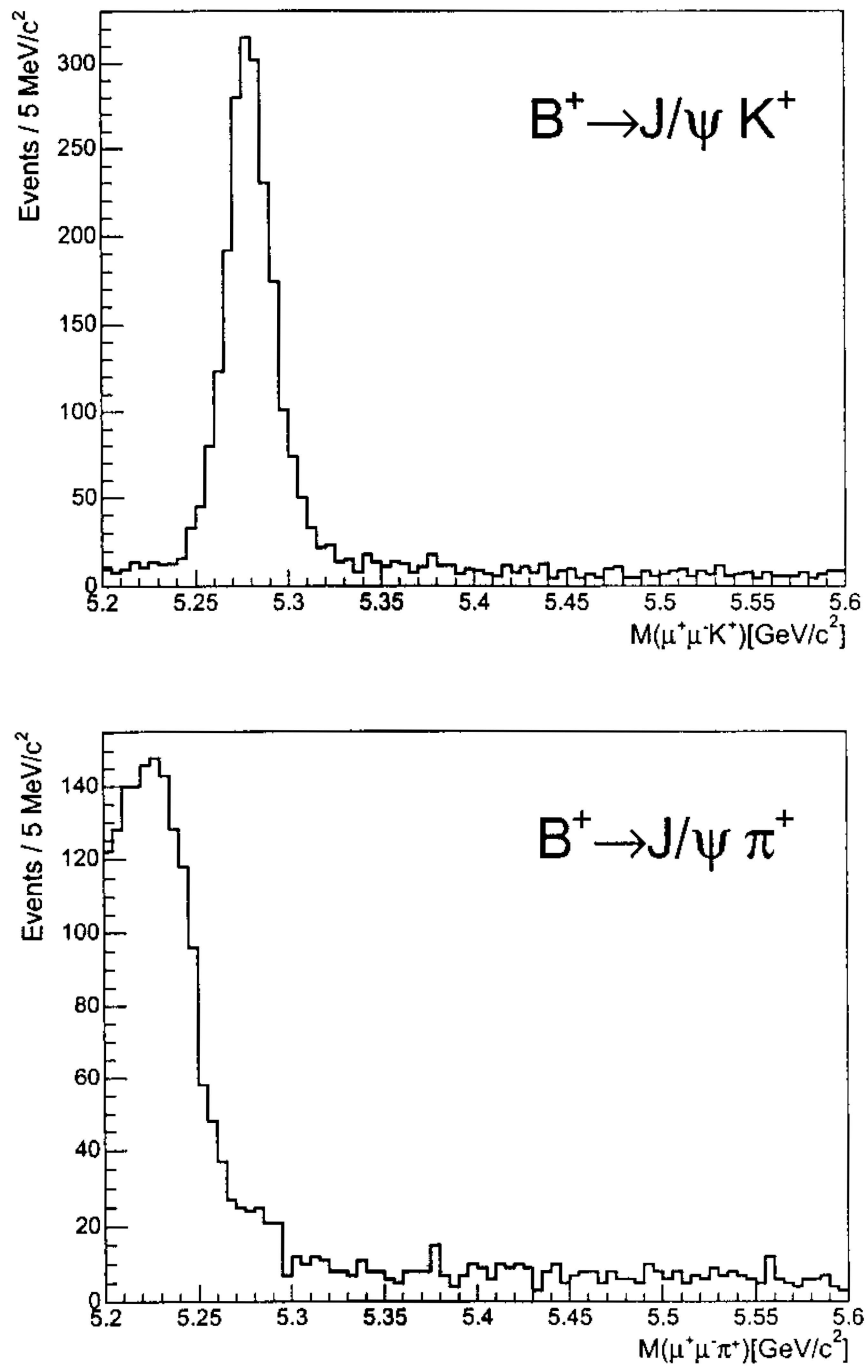


Figure 3.3: The invariant mass distributions of  $M(\mu^+\mu^-K^+)$  (top) and  $M(\mu^+\mu^-\pi^+)$  (bottom). The bottom plot is the invariant mass distribution when the third track is assumed as pion.



## Chapter 4

# Measurement of the Ratio of Branching Fractions

The absolute branching fraction for  $B^+ \rightarrow J/\psi\pi^+$  is given by

$$\mathcal{B}(B^+ \rightarrow J/\psi\pi^+) = \frac{\mathcal{N}_{obs}(B^+ \rightarrow J/\psi\pi^+)}{\epsilon_{trig} \cdot \epsilon_{recon} \cdot \epsilon_{cuts} \cdot \mathcal{N}_{prod}(B^+)}, \quad (4.1)$$

where

- $\mathcal{N}_{obs}(B^+ \rightarrow J/\psi\pi^+)$  is the number of observed  $B^+ \rightarrow J/\psi\pi^+$  decay,
- $\epsilon_{trig}$  is the trigger, especially  $J/\psi$  trigger, efficiency,
- $\epsilon_{recon}$  is the reconstruction efficiency,
- $\epsilon_{cuts}$  is the cuts efficiency,
- $\mathcal{N}_{prod}(B^+)$  is the number of produced  $B^+$  meson.

To compare this with  $B^+ \rightarrow J/\psi K^+$ , we use the similar formula

$$\mathcal{B}(B^+ \rightarrow J/\psi K^+) = \frac{\mathcal{N}_{obs}(B^+ \rightarrow J/\psi K^+)}{\epsilon_{trig} \cdot \epsilon_{recon} \cdot \epsilon_{cuts} \cdot \mathcal{N}_{prod}(B^+)}. \quad (4.2)$$

For the ratio of  $B^+ \rightarrow J/\psi\pi^+$  to  $B^+ \rightarrow J/\psi K^+$ , we divide the above two equation 4.1 and 4.2 to get

$$\begin{aligned} \frac{\mathcal{B}(B^+ \rightarrow J/\psi\pi^+)}{\mathcal{B}(B^+ \rightarrow J/\psi K^+)} &= \frac{\mathcal{N}_{obs}(B^+ \rightarrow J/\psi\pi^+)}{\mathcal{N}_{obs}(B^+ \rightarrow J/\psi K^+)} \cdot \frac{\epsilon_{trig}^{J/\psi K} \cdot \epsilon_{recon}^{J/\psi K} \cdot \epsilon_{cuts}^{J/\psi K}}{\epsilon_{trig}^{J/\psi\pi} \cdot \epsilon_{recon}^{J/\psi\pi} \cdot \epsilon_{cuts}^{J/\psi\pi}} \\ &= \frac{r_{obs}}{\epsilon_{rel}}. \end{aligned} \quad (4.3)$$

where

- $r_{obs}$  is the observed raw ratio  $r_{obs} = \frac{\mathcal{N}_{obs}(B^+ \rightarrow J/\psi\pi^+)}{\mathcal{N}_{obs}(B^+ \rightarrow J/\psi K^+)}$ ,
- $\epsilon_{rel}$  is the relative reconstruction efficiency,  $\epsilon_{rel} = \frac{\epsilon_{trig}^{J/\psi\pi} \cdot \epsilon_{recon}^{J/\psi\pi} \cdot \epsilon_{cuts}^{J/\psi\pi}}{\epsilon_{trig}^{J/\psi K} \cdot \epsilon_{recon}^{J/\psi K} \cdot \epsilon_{cuts}^{J/\psi K}}$ .

By determining the above quantities, the ratio of branching fractions can be computed.

As shown in Figure 4.1, the invariant mass distribution of  $B^+ \rightarrow J/\psi\pi^+$  signal, when the kaon mass hypothesis is assigned to the third track of  $B^+ \rightarrow J/\psi\pi^+$  decay, is slightly shifted to higher value from its nominal value. This mass shift makes some overlap of two mass distributions,  $M(B^+ \rightarrow J/\psi K^+)$  and  $M(B^+ \rightarrow J/\psi\pi^+)$ , in  $M(\mu^+\mu^-K^+)$  space. To separate these two overlapped signals and background for obtaining the raw ratio we use the likelihood method. The relative reconstruction efficiency for two decay is calculated by Monte Carlo simulation. In this chapter we discuss these methods in detail.

## 4.1 Mass Shift Calculation

The mass shifts apparent in Figure X can be written down in a simple form for the generic decay of a heavy particle into two daughters. Consider  $B^+ \rightarrow J/\psi X^+$  decay with 3-dimensional momenta  $\vec{p}_{J/\psi}$  and  $\vec{p}_X$ . We define  $M_{J/\psi X}$  as the invariant mass of 2-body system when we assign masses  $M_{J/\psi}$  and  $M_X$  respectively to  $J/\psi$  and  $X$ :

$$M_{J/\psi X}^2 = \left( \sqrt{M_{J/\psi}^2 + p_{J/\psi}^2} + \sqrt{M_X^2 + p_X^2} \right)^2 - (\vec{p}_{J/\psi} + \vec{p}_X)^2. \quad (4.4)$$

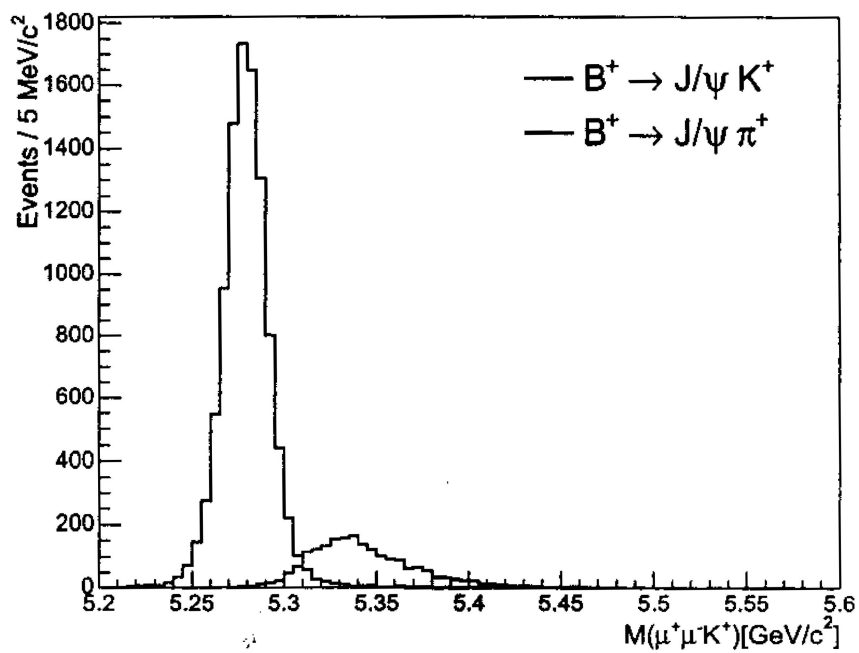


Figure 4.1: The invariant mass distributions of  $B^+ \rightarrow J/\psi K^+$  (blue) and  $B^+ \rightarrow J/\psi \pi^+$  (Red) when the kaon mass is assigned to the third track. These distributions are generated by Monte Carlo.

If mass  $M_{X'}$  is assigned to particle  $X$ , the invariant mass  $M_{J/\psi X'}$  is given by

$$M_{J/\psi X'}^2 = \left( \sqrt{M_{J/\psi}^2 + p_{J/\psi}^2} + \sqrt{M_{X'}^2 + p_X^2} \right)^2 - (\vec{p}_{J/\psi} + \vec{p}_X)^2. \quad (4.5)$$

The difference between the squared invariant masses reconstructed with two different mass assignments is given by

$$\begin{aligned} & M_{J/\psi X'}^2 - M_{J/\psi X}^2 \\ &= \left( \sqrt{M_{J/\psi}^2 + p_{J/\psi}^2} + \sqrt{M_{X'}^2 + p_X^2} \right)^2 - \left( \sqrt{M_{J/\psi}^2 + p_{J/\psi}^2} + \sqrt{M_X^2 + p_X^2} \right)^2 \\ &= 2E_{J/\psi} \left( \sqrt{M_{X'}^2 + p_X^2} - \sqrt{M_X^2 + p_X^2} \right) + M_{X'}^2 - M_X^2 \\ &\cong \left( 1 + \frac{E_{J/\psi}}{p_X} \right) \cdot (M_{X'}^2 - M_X^2), \end{aligned} \quad (4.6)$$

where  $E_{J/\psi}$  is the energy of the  $J/\psi$ . Since the transverse momentum of  $X$  should be greater than 2.0 GeV/c and the pion and kaon masses are respectively 0.139 and 0.493 GeV/c<sup>2</sup>, equation 4.6 is approximated at first order in  $\mathcal{O}((m_{J/\psi}/p_X)^2)$ . Equation 4.6 shows that, given the invariant mass reconstructed with a particular mass assignments to the decay products, the mass difference can be expressed as a function of just one additional quantity,  $\frac{E_{J/\psi}}{p_X}$ . The invariant mass of true  $B^+ \rightarrow J/\psi\pi^+$  events, when the kaon mass is assigned to the pion, can be computed easily by substituting  $X \rightarrow \pi$  and  $X' \rightarrow K$

$$\mathcal{M}_{J/\psi\pi}^2(\alpha) = M_{B^+}^2 + (1 + \alpha) \cdot (M_K^2 - M_\pi^2), \quad (4.7)$$

where the parameter  $\alpha$  is given by  $\alpha \equiv \frac{E_{J/\psi}}{p_K}$ . In the case of  $B^+ \rightarrow J/\psi K^+$  decay the invariant mass is merely given by

$$\mathcal{M}_{J/\psi K}^2 = M_{B^+}^2. \quad (4.8)$$

Figure 4.2 shows the distributions of mass difference,  $M(\mu\mu K) - \mathcal{M}(\alpha)$ , in each case of  $B^+ \rightarrow J/\psi K^+$  and  $B^+ \rightarrow J/\psi\pi^+$  signals generated by Monte

Carlo. These distributions are followed by Gaussians because of the detector resolution. We fit them with a Gaussian and know their widths have almost same value.

## 4.2 Likelihood

Two signal distributions are modeled with a 2D distribution,  $P_{sig}(M_{\mu\mu K}, \alpha)$ ,

$$P_{sig}(M_{\mu\mu K}, \alpha) = G(M_{\mu\mu K} - \mathcal{M}(\alpha), \sigma) \cdot h_{sig}(\alpha), \quad (4.9)$$

where  $G(M_{\mu\mu K} - \mathcal{M}(\alpha), \sigma)$  is a Gaussian with width  $\sigma$  and  $h(\alpha)$  is the  $\alpha$  distribution for each signal. This probability distribution function (PDF) for signals requires some input parameters to parameterize  $\alpha$  distributions for each decay mode and we obtain these information from Monte Carlo. To parameterize the  $\alpha$  distributions for each signal, we use a function,

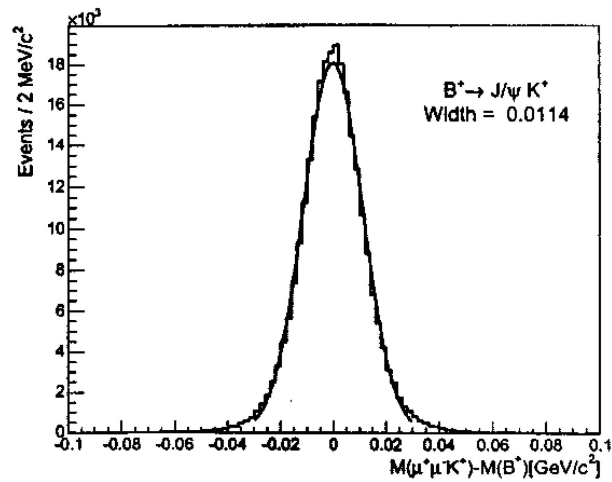
$$h_{sig}(\alpha; f_i, \lambda_i, a) = \sum_{i=1}^3 f_i(\alpha - a)e^{-\lambda_i \alpha}. \quad (4.10)$$

The  $\alpha$  distributions for each decay mode from Monte Carlo with the parameterizing function overlaid are shown in Figure 4.3 and their parameters is in Table 4.1.

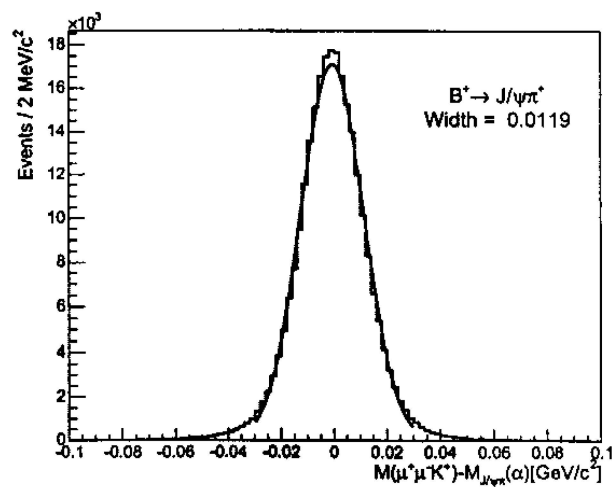
mode	a	$\lambda_1$	$\lambda_2$	$\lambda_3$	$f_2$	$f_3$
$B^+ \rightarrow J/\psi K^+$	0.527	<b>0.600</b>	<b>4.629</b>	1.275	0.149	0.774
$B^+ \rightarrow J/\psi \pi^+$	0.522	<b>0.631</b>	5.013	1.230	0.134	0.772
background	0.398	<b>0.726</b>	<b>6.540</b>	1.978	0.130	0.846

Table 4.1: The fitted parameters used in  $h_{sig}(\alpha)$  for each decay mode and  $h_{bkg}(\alpha)$  for the background events, where  $f_1 = 1 - f_2 - f_3$  to normalize the functions.

With all the information described above, the total signal PDF for  $i$ th event

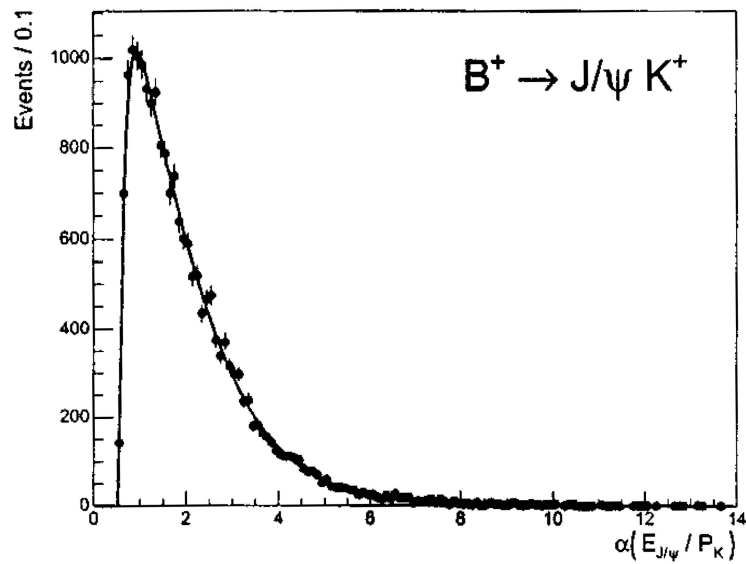


(a)

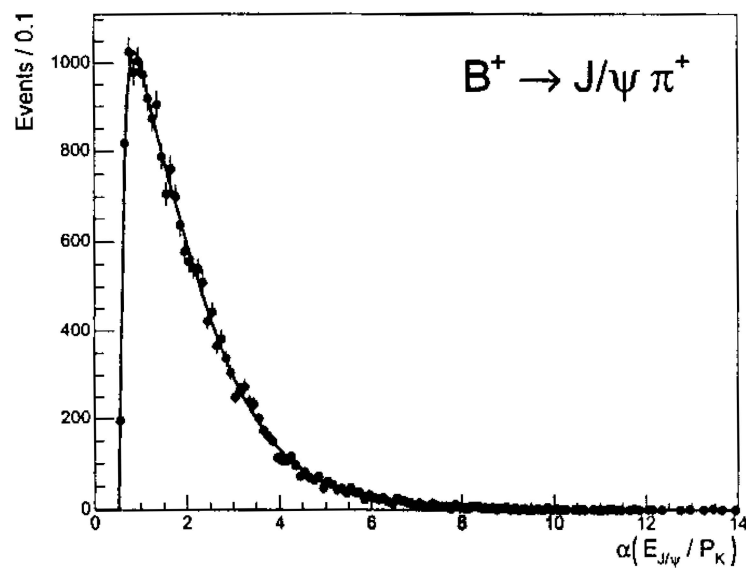


(b)

Figure 4.2: The distributions of mass difference,  $M(\mu\mu K) - \mathcal{M}(\alpha)$ , in the cases of (a)  $B^+ \rightarrow J/\psi K^+$  and (b)  $B^+ \rightarrow J/\psi\pi^+$  signals which are generated by Monte Carlo.



(a)



(b)

Figure 4.3: The  $\alpha$  distributions with the parameterizing function overlaid for (a)  $B^+ \rightarrow J/\psi K^+$  and (b)  $B^+ \rightarrow J/\psi \pi^+$  signals which are generated by Monte Carlo

is written by

$$P_{sig}^i = \frac{1}{1+r} G(M_{\mu\mu K}^i - M_{B^+}, \sigma) \cdot h_{J/\psi K}(\alpha^i) + \frac{r}{1+r} G(M_{\mu\mu K}^i - \mathcal{M}_{J/\psi\pi}(\alpha^i), \sigma) \cdot h_{J/\psi\pi}(\alpha^i), \quad (4.11)$$

where we introduce a parameter  $r$  to extract the raw ratio.

The background is modeled with a 2D distribution,  $P_{bkg}(M_{\mu\mu K}, \alpha)$ , the background PDF for  $i$ th event is written by

$$P_{bkg}^i = p_1(M_{\mu\mu K}^i) \cdot h_{bkg}(\alpha^i), \quad (4.12)$$

where  $p_1(M_{\mu\mu K}^i)$  is a 1st order polynomial function defined as

$$p_1(M_{\mu\mu K}) = s \cdot \left( M_{\mu\mu K} - \frac{up + ll}{2} \right) + \frac{1}{up - ll} \quad (4.13)$$

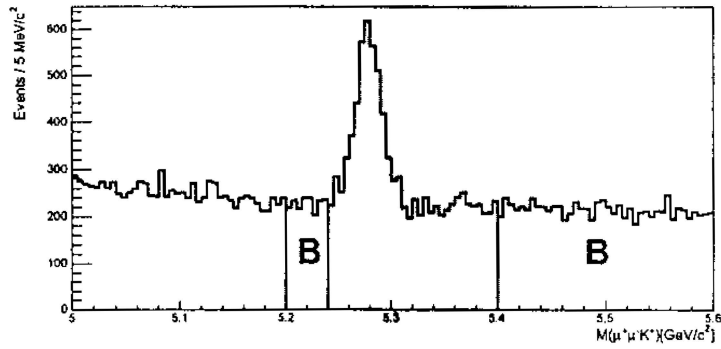
where  $s$  is the slope of the linear background,  $ll$  and  $up$  are the lower and upper limits to normalize  $p_1$  to unit area.  $h_{bkg}(\alpha)$  is the  $\alpha$  distribution for the background events. This distribution is obtained from the sidebands of data. We select two sidebands,  $5.2 < M(\mu\mu K) < 5.24$  and  $5.4 < M(\mu\mu K) < 5.6$  GeV/ $c^2$  (Figure 4.4(a)). These regions are almost free from the signal contamination. Since we don't ask  $L_{xy}$  requirement to get more background events. To parameterize the  $\alpha$  distributions for background, we use a function,

$$h_{bkg}(\alpha; f_i, \lambda_i, a) = \sum_{i=1}^3 f_i (\alpha - a)^3 e^{-\lambda_i \alpha}. \quad (4.14)$$

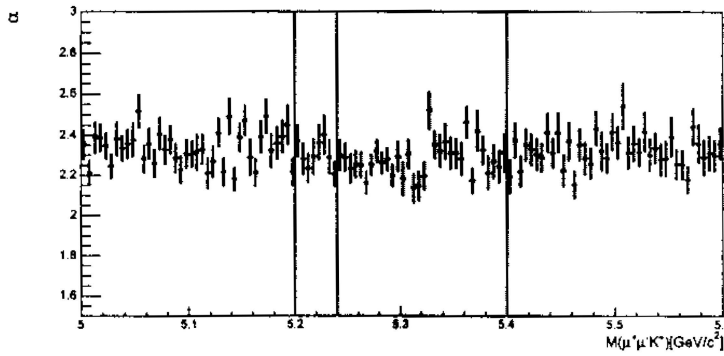
The  $\alpha$  distributions for the background events with the parameterizing function overlaid are shown in Figure 4.5 and their parameters are in Table 4.1.

With the signal and background PDFs, the likelihood is written by

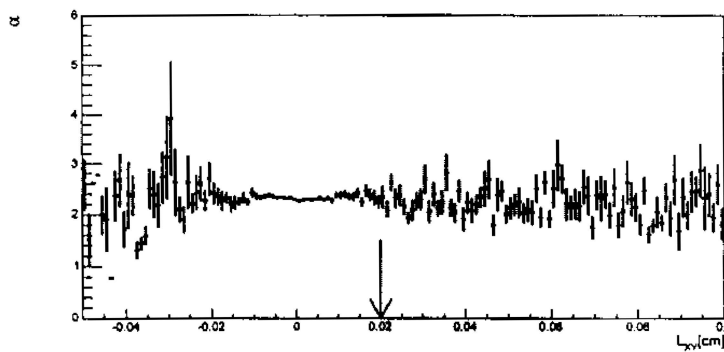
$$\mathcal{L} = \prod_i^{N_{events}} [f_{sig} \cdot P_{sig}^i(M_{\mu\mu K}^i, \alpha^i; M_{B^+}, \sigma, r) + (1 - f_{sig}) \cdot P_{bkg}^i(M_{\mu\mu K}^i, \alpha^i; s)] \quad (4.15)$$



(a)



(b)



(c)

Figure 4.4: (a) The invariant mass distribution of  $M(\mu\mu K)$  without  $L_{xy}$  cut. The sidebands are marked as “B”. (b) The profile histogram of  $M(\mu\mu K)$  versus  $\alpha$ . (c) The profile histogram of  $L_{xy}$  versus  $\alpha$ . The red arrow represents  $L_{xy}$  cut value.

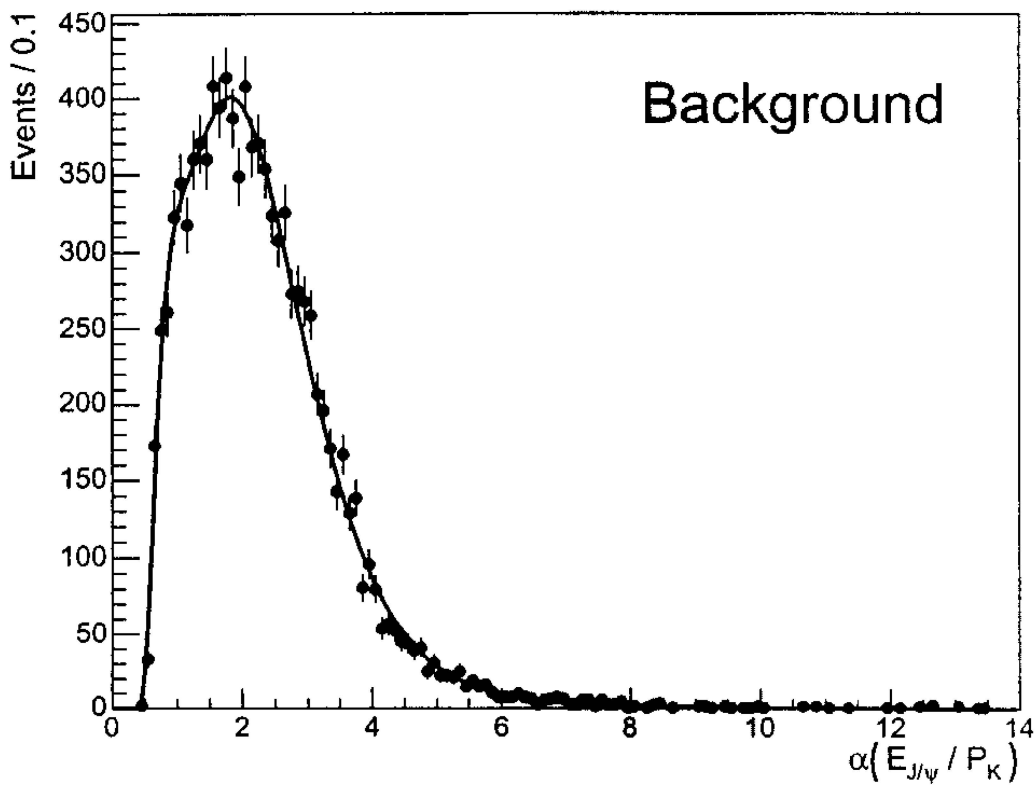


Figure 4.5: The  $\alpha$  distributions for the background events with the parameterizing function overlaid.

where  $f_{sig}$  is the signal fraction in data. We have all 5 fitting parameters in fit,  $M_{B^+}$ ,  $\sigma$ ,  $r$ ,  $f_{sig}$  and  $s$ .

## 4.3 Fitting Range

There are three components which consist of all entry in data;  $B^+ \rightarrow J/\psi K^+$  signals, reflections from  $B^+ \rightarrow J/\psi \pi^+$  signal and backgrounds. Since the reflections should be carefully counted to get the raw, we have to choose the fitting range not to lose them. We check almost all reflections lies in  $5.3 < M(\mu\mu K) < 5.4 \text{ GeV}/c^2$  using Monte Carlo. Then, we consider the combinatorial background shape in  $5.4 < M(\mu\mu K) < 5.6 \text{ GeV}/c^2$ . From these considerations, we decide the upper limit to be  $M(\mu\mu K) < 5.6 \text{ GeV}/c^2$  for fit.

We choose the lower limit for fit to be  $M(\mu\mu K) > 5.2 \text{ GeV}/c^2$  to avoid long-lived backgrounds from partially reconstructed  $B$  mesons, such as  $B^0 \rightarrow J/\psi K^{0*}$ , which can fall below the  $B$  meson's mass. Figure 4.6 shows the invariant mass distribution of  $B^+ \rightarrow J/\psi K^+$  decay overlaid with the reflections from  $B^+ \rightarrow J/\psi \pi^+$  and backgrounds from partially reconstructed  $B$  mesons.

We choose the the fitting range to be  $5.2 < M(\mu\mu K) < 5.6 \text{ GeV}/c^2$ . We apply all cuts described section X on  $B^+$  candidates and select the entries falling in the fitting range. We have 2683 entries in this range.

## 4.4 Fitting Results

The maximum likelihood method is applied to data. We determine a signal fraction of  $0.736 \pm 0.012$  and the raw ratio of  $4.82 \pm 0.81\%$ . This gives us  $1883.1 \pm 33.5$  signal events in the  $B^+ \rightarrow J/\psi K^+$  decay mode and  $90.8 \pm 14.6$  in the  $B^+ \rightarrow J/\psi \pi^+$  decay mode. The measured  $B^+$  mass is  $5.2792 \pm 0.0003 \text{ GeV}/c^2$ , which is consistent with the measurement of  $B^+$ 's mass in Ref. [34] and the world average value [31]. The results of the fit are summarized in Table 4.2. Figure 4.7 and 4.8 show the fitting results projected on data.

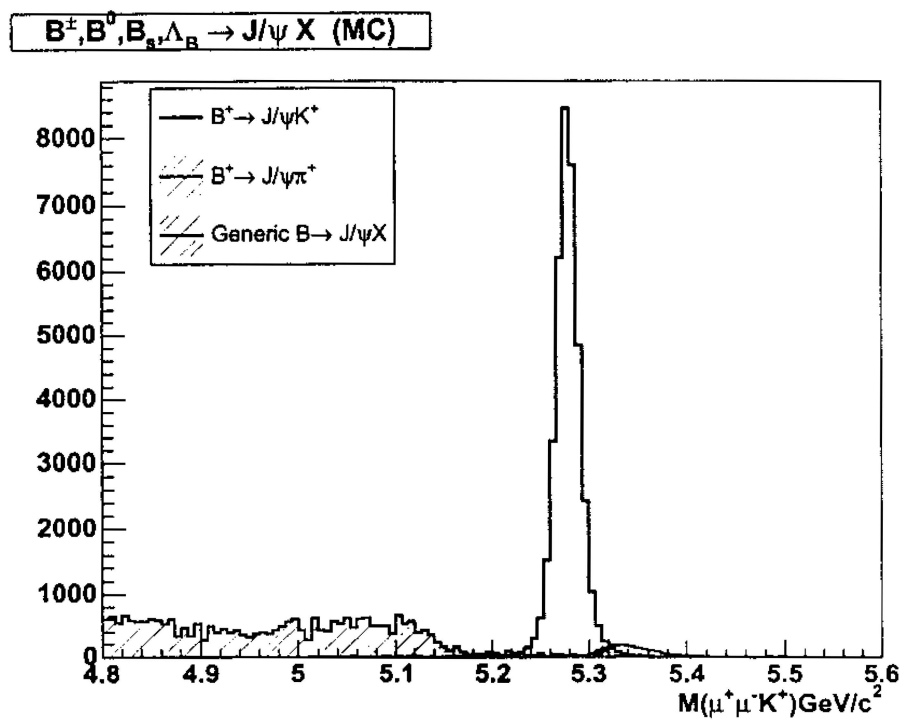


Figure 4.6: Invariant mass of  $B^+ \rightarrow J/\psi K^+$  from realistic Monte Carlo overlaid with the reflection from  $B^+ \rightarrow J/\psi \pi^+$  and partially reconstructed B-mesons.

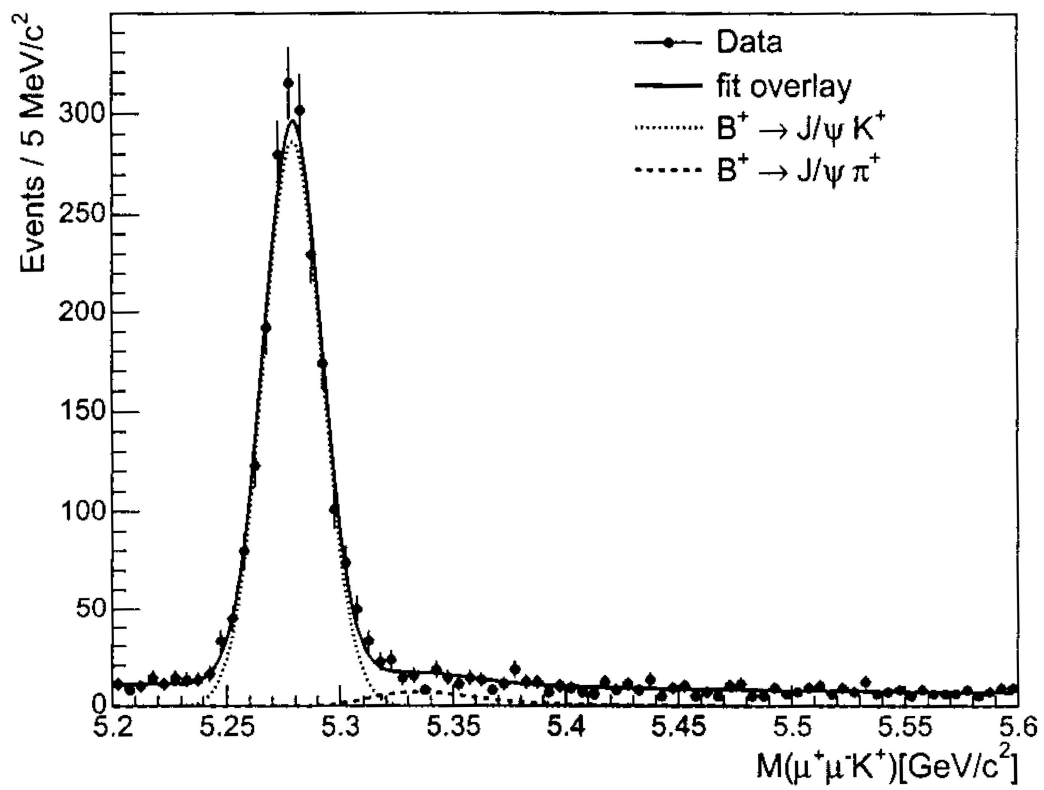


Figure 4.7: Fitting results projected onto the invariant mass distribution of data.

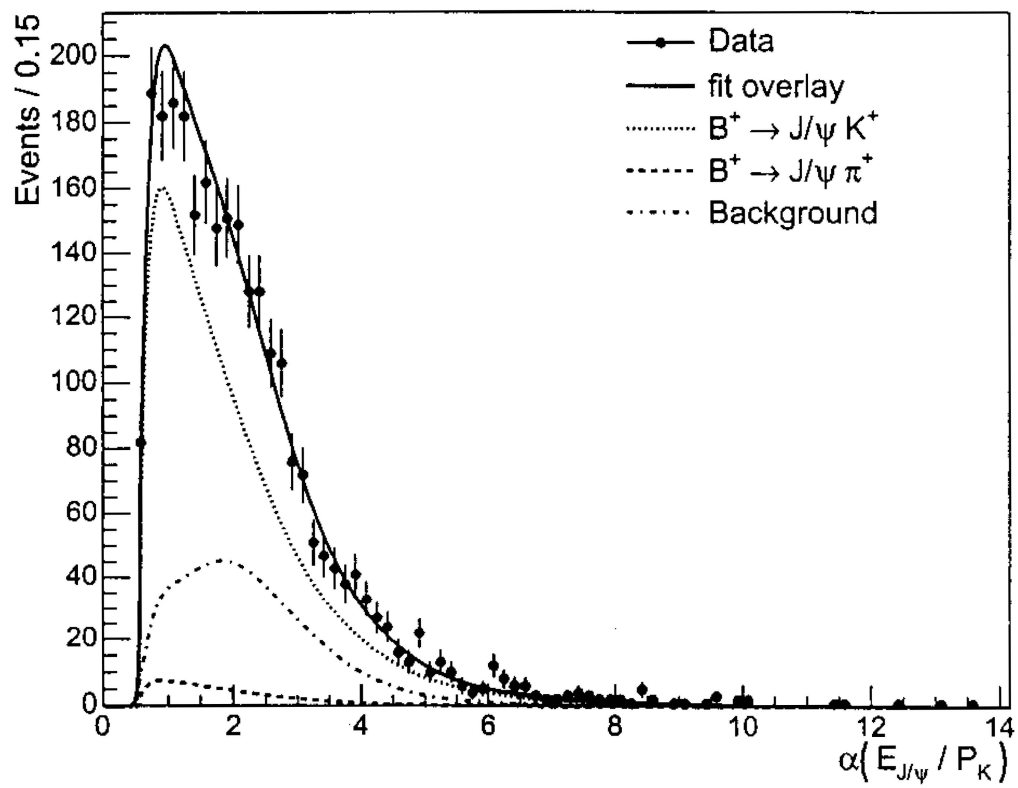


Figure 4.8: Fitting results projected onto the  $\alpha$  distribution of data.

parameter	value
$M_{B^+}$	$5.2792 \pm 0.0003$
$\sigma$	$1.31 \pm 0.0003$
$r$	$0.0482 \pm 0.0081$
$f_{sig}$	$0.736 \pm 0.012$
$s$	$-3.23 \pm 0.93$
$\mathcal{N}(B^+ \rightarrow J/\psi K^+)$	$1883.1 \pm 33.5$
$\mathcal{N}(B^+ \rightarrow J/\psi \pi^+)$	$90.8 \pm 14.6$

Table 4.2: The value of the fitted parameters that best represent data.

## 4.5 Cross Checks

Various cross-checks have been performed on data. They are concerned with checking that  $B^+ \rightarrow J/\psi \pi^+$  signal events are not really  $B^+ \rightarrow J/\psi K^+$  events.

The first cross-check is a scatter plot of  $M(\mu\mu K)$  versus  $M(\mu\mu\pi)$ . This plot is shown in Figure 4.9. The plot shows that, although there is some overlap which is expected, the majority of the events are far from the  $B^+$  mass in  $M(\mu\mu K)$ .

The second check is to consider all the events to be from  $B^+$  decay and to find the mass of the third track. The  $B$  meson's four-momentum is found by adding the  $J/\psi$ 's and the third track's three-momentum and then assuming the  $B^+$  mass

$$\vec{P}_B = \vec{P}_{J/\psi} + \vec{P}_3 \quad (4.16)$$

$$\mathcal{P}_B = \left( \vec{P}_B, \sqrt{|\vec{P}_B|^2 + M_{B^+}^2} \right) \quad (4.17)$$

Then the four-momentum of the third track is determined by subtracting the  $J/\psi$ 's four-momentum from the  $B$ 's.

$$\mathcal{P}_3 = \mathcal{P}_B - \mathcal{P}_{J/\psi}. \quad (4.18)$$

Squaring this recalculated four-momentum gives the third track's mass. A plot

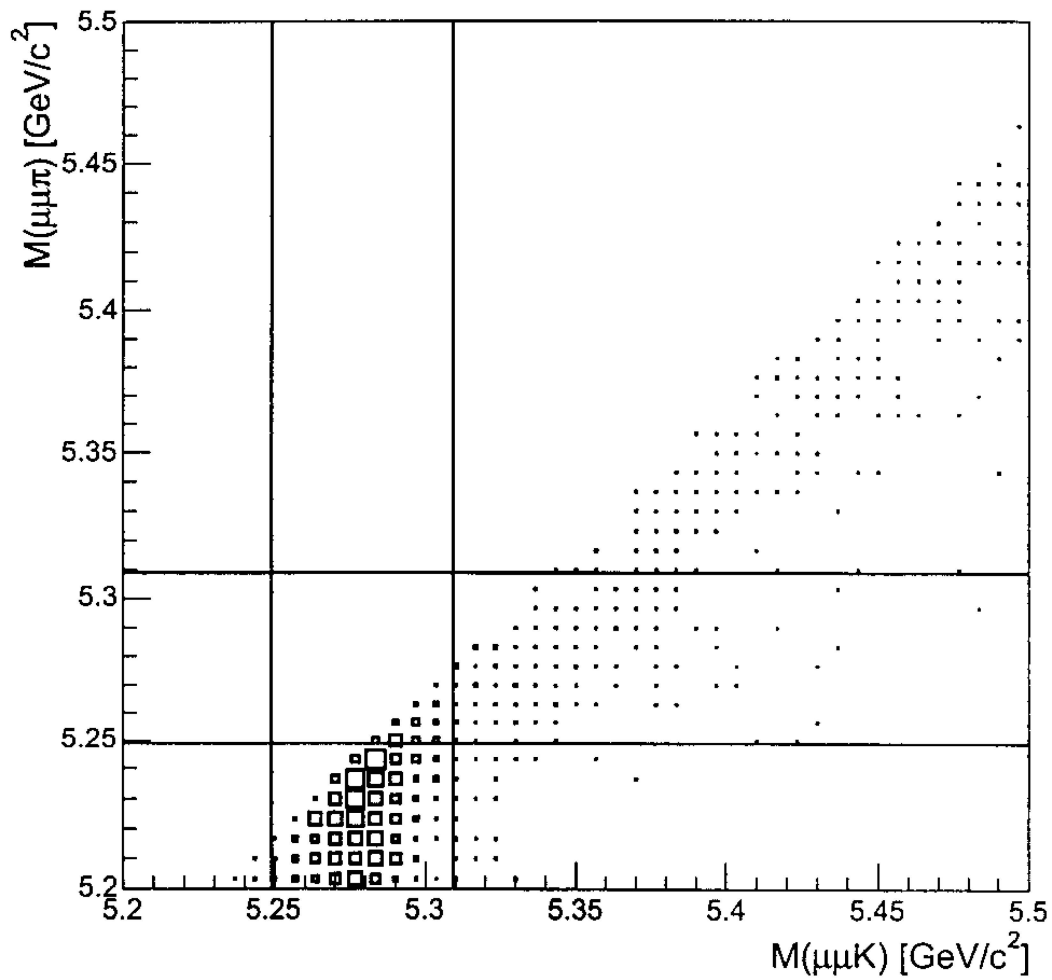


Figure 4.9: A scatter plot of  $M(\mu\mu K)$  versus  $M(\mu\mu\pi)$ . The lines shown represent the  $2.5\sigma$  around  $M(B^+)$ .

of the third track mass versus the  $M(\mu\mu\pi)$  is shown in Figure 4.10.

## 4.6 Likelihood including PID Information

The CDF utilizes two kinds of method for the particle identification, these are  $dE/dx$  and TOF. In this analysis, identifying what the third track is, which may be the kaon or pion, can make it possible to separate  $B^+ \rightarrow J/\psi K^+$  and  $B^+ \rightarrow J/\psi \pi^+$  signals which are overlapped each other. Since TOF gives poor resolution in out momentum region (see section X), we don't use information of TOF. We now focus on the use of  $dE/dx$ .

We use a  $ID$  variable which is a single observable to represent the  $dE/dx$  information of the kaon and pion. The  $ID$  variable is defined as

$$ID = \frac{\left(\frac{dE}{dx}\right)_{measured} - \left(\frac{dE}{dx}\right)_{exp-\pi}}{\left(\frac{dE}{dx}\right)_{exp-K} - \left(\frac{dE}{dx}\right)_{exp-\pi}}, \quad (4.19)$$

where  $\left(\frac{dE}{dx}\right)_{measured}$  is  $dE/dx$  value measured at COT and  $\left(\frac{dE}{dx}\right)_{exp-\pi,K}$  is the expected value with the hypothesis of pion or kaon calculated by Bethe-Bloch Formula. We obtain the distribution of ID for pion and kaon tracks from reconstructed  $D^0 \rightarrow K^+\pi^-$  decay with proper corrections [33]. Figure X shows these distributions. We parameterize these with two Gaussians to obtain the PDFs for the PID.

The signal and background PDFs are modified to include the  $dE/dx$  information. The signal PDF is now changed to

$$P_{sig}(M_{\mu\mu K}, \alpha) = G(M_{\mu\mu K} - \mathcal{M}(\alpha), \sigma) \cdot h_{sig}(\alpha) \cdot D(ID), \quad (4.20)$$

where  $D(ID)$  is the PDF for the  $ID$  of kaon or pion. With this PDF, the

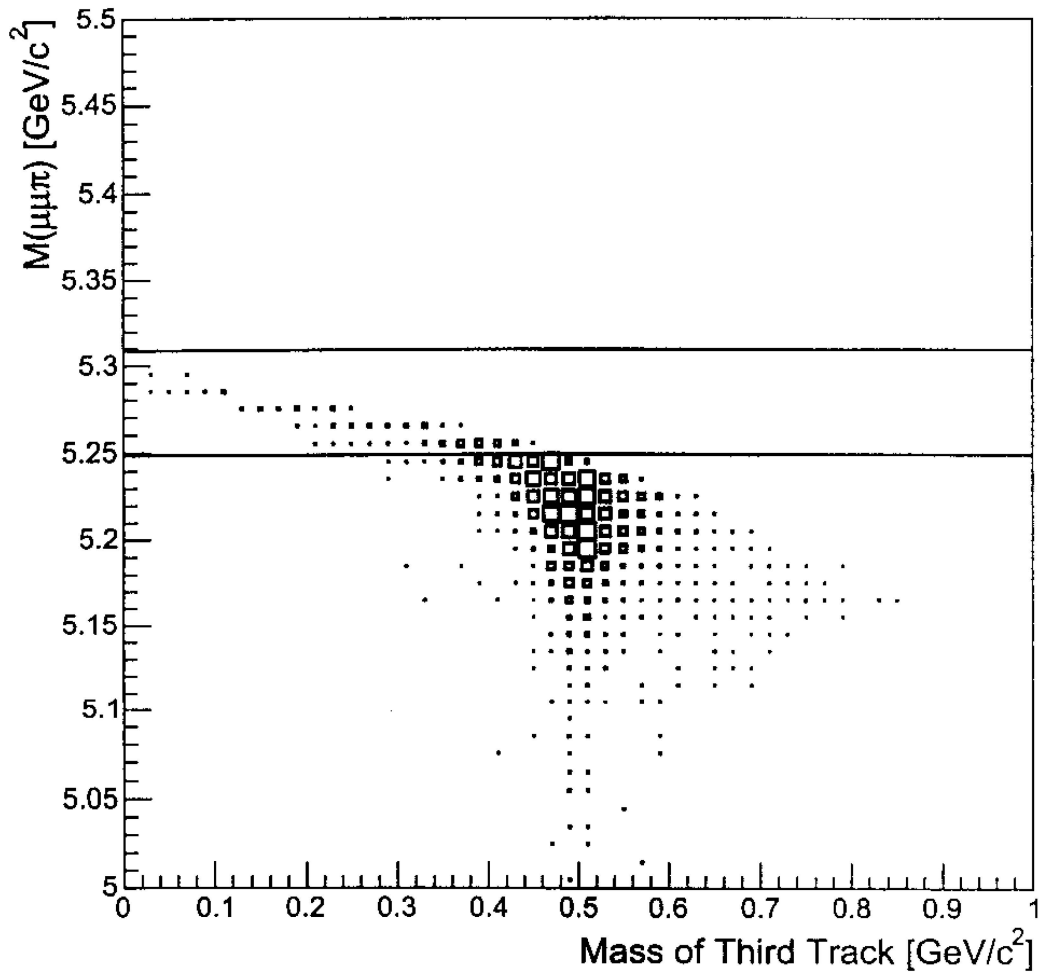
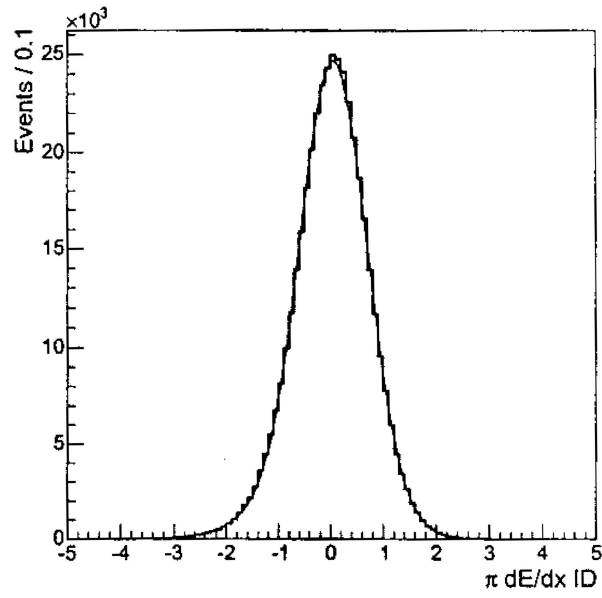
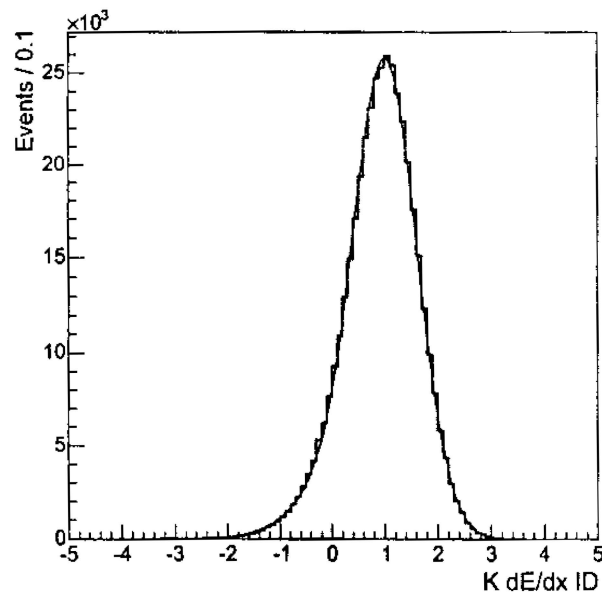


Figure 4.10: The  $M(\mu\mu\pi)$  versus the third track's invariant mass. This mass is calculated by constraining the three tracks to form a  $B^+$



(a)



(b)

Figure 4.11:  $dE/dx$  ID distribution for (a) pion and (b) kaon.

signal PDF is written explicitly by

$$P_{sig}^i = \frac{1}{1+r} G(M_{\mu\mu K}^i - M_{B^+}, \sigma) \cdot h_{J/\psi K}(\alpha^i) \cdot D_{J/\psi K}(ID^i) + \quad (4.21)$$

$$\frac{r}{1+r} G(M_{\mu\mu K}^i - \mathcal{M}_{J/\psi\pi}(\alpha^i), \sigma) \cdot h_{J/\psi\pi}(\alpha^i) \cdot D_{J/\psi\pi}(ID^i). \quad (4.22)$$

And the background PDF is changed to

$$P_{bkg}^i = p_1(M_{\mu\mu K}^i) \cdot h_{bkg}(\alpha^i) \cdot (f_\pi \cdot D_{J/\psi\pi}(ID^i) - (1 - f_\pi) \cdot D_{J/\psi K}(ID^i)), \quad (4.23)$$

where  $f_\pi$  is the fraction of pion in background.

With these modified PDFs, the likelihood with the  $dE/dx$  information is written by

$$\mathcal{L} = \prod_i^{N_{events}} [f_{sig} \cdot P_{sig}^i(M_{\mu\mu K}^i, \alpha^i, ID^i; M_{B^+}, \sigma, r) + (1 - f_{sig}) \cdot P_{bkg}^i(M_{\mu\mu K}^i, \alpha^i, ID^i; s, f_\pi)]. \quad (4.24)$$

We fit data again using above likelihood. The fit result is summarized in Table 4.3. Figure 4.12, 4.13 and 4.14 show the fitting results overlaid onto data.

parameter	value
$M_{B^+}$	$5.2792 \pm 0.0003$
$\sigma$	$1.32 \pm 0.0003$
$r$	$0.0464 \pm 0.0075$
$f_{sig}$	$0.742 \pm 0.011$
$s$	$-2.79 \pm 0.93$
$f_\pi$	$0.57 \pm 0.04$
$\mathcal{N}(B^+ \rightarrow J/\psi K^+)$	$1901.3 \pm 31.8$
$\mathcal{N}(B^+ \rightarrow J/\psi\pi^+)$	$88.2 \pm 13.8$

Table 4.3: The value of the fitted parameters that best represent data when the  $dE/dx$  information is used.

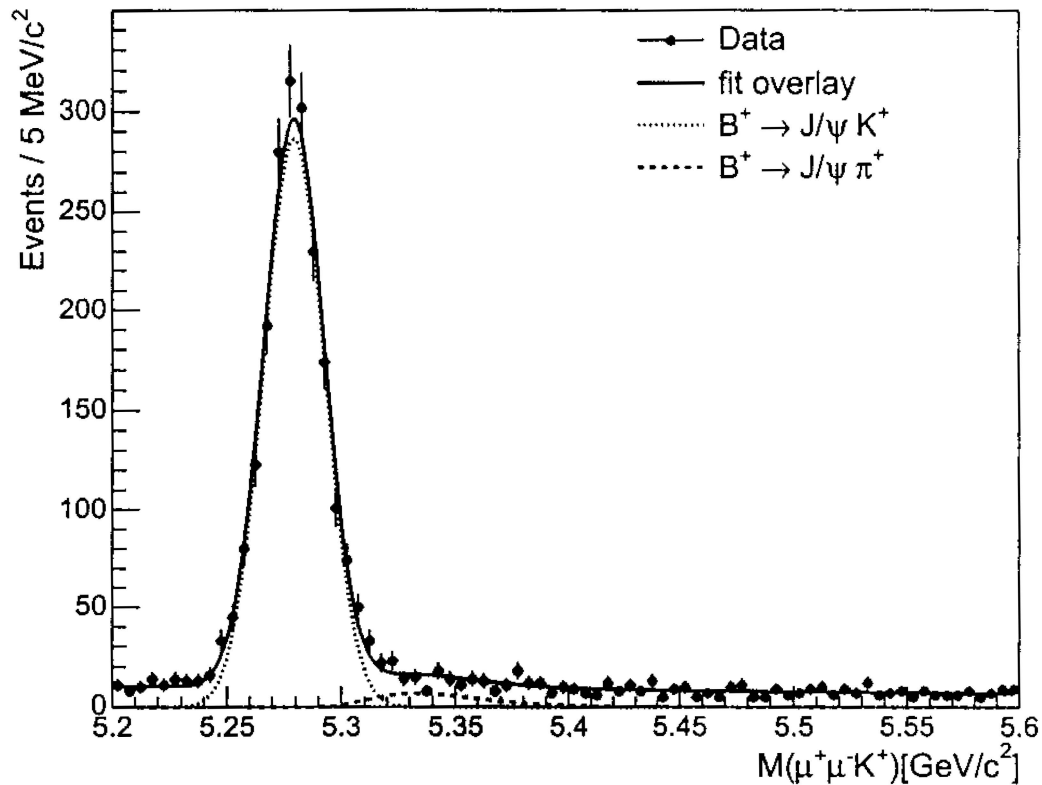


Figure 4.12: Fitting results projected onto the invariant mass distribution of data.

This result shows 3.4% of improvement in the relative statistical uncertainty of the raw ratio. But we expect about 6% of improvement using toy MC test when the  $dE/dx$  information is used.

## 4.7 Calculation of the Relative Reconstruction Efficiency

In order to determine the true ratio of branching fractions, the raw ratio must be corrected for the relative reconstruction efficiency,  $\epsilon_{rel}$ , which depends on the different decay-in-flight and nuclear interaction of kaon and pion from the

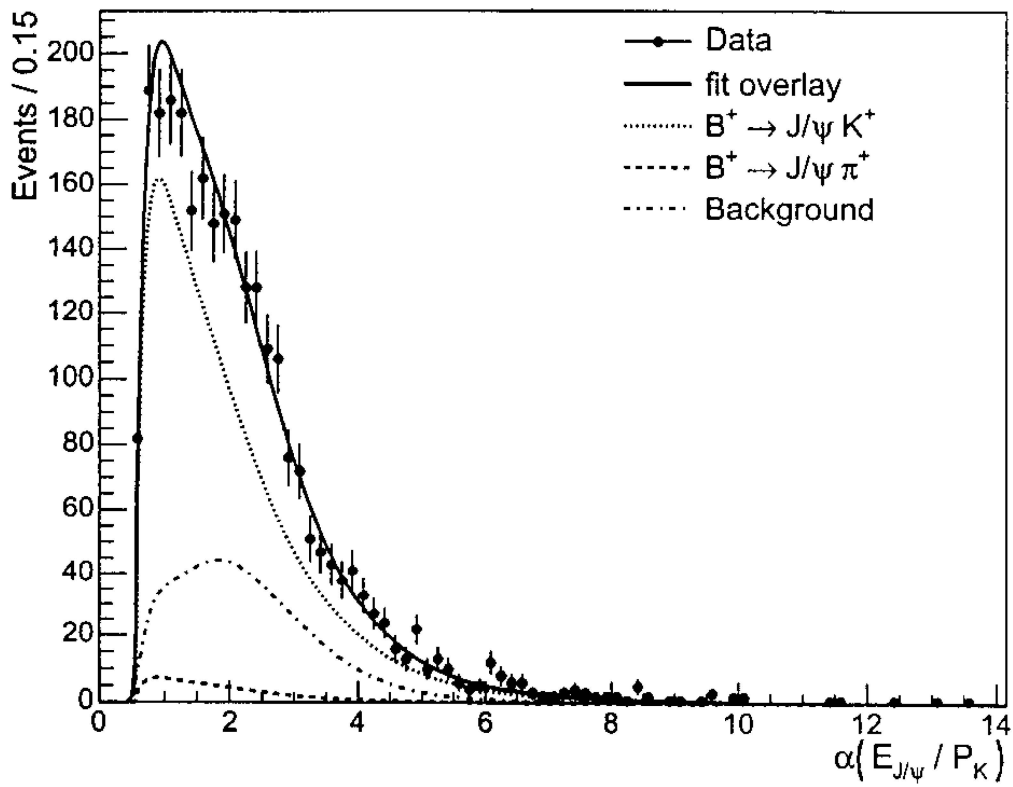


Figure 4.13: Fitting results projected onto the  $\alpha$  distribution of data.

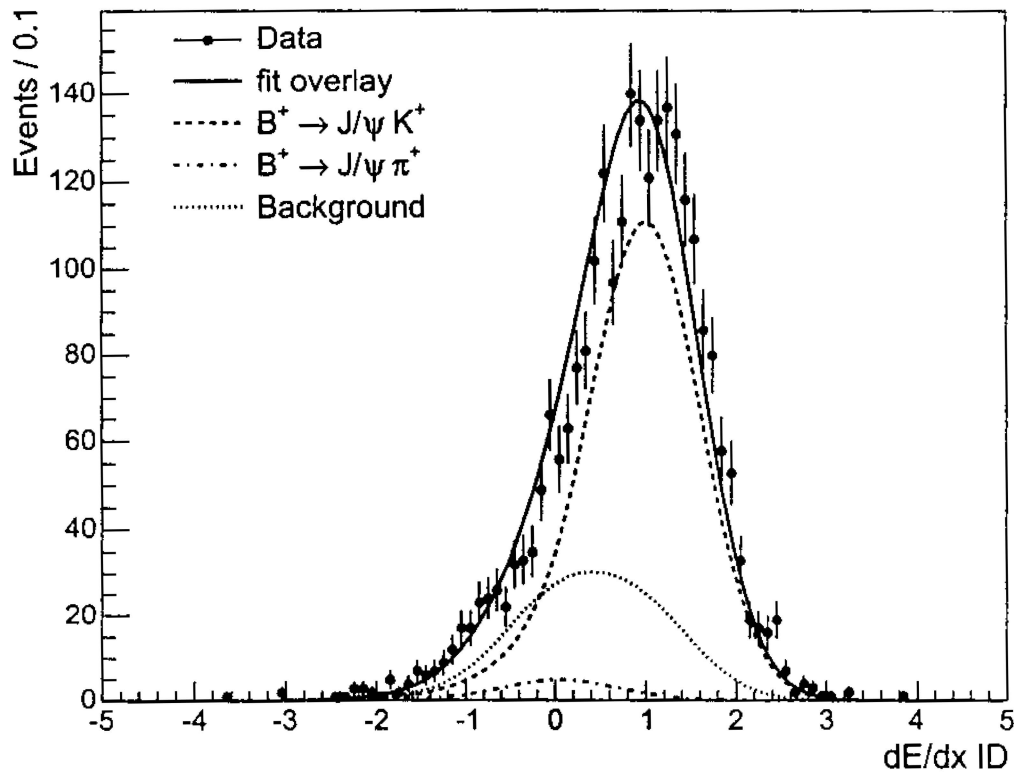


Figure 4.14: Fitting results projected onto the  $dE/dx$  ID distribution of data.

two decay modes and the slightly different track momentum spectra.

In this analysis, a Monte Carlo simulation is used to determine the relative reconstruction efficiency. The Monte Carlo generation proceeds as follows. Transverse momentum and rapidity distribution of single  $b$  quarks are generated based on calculations using next-to-leading order perturbative QCD [35]. B meson kinematic distributions are obtained by simulating Peterson fragmentation [36] on quark-level distributions. Additional fragmentation particles, correlated  $b - \bar{b}$  production and the underlying event structure are not simulated. The simulation of the CDF II detector and trigger is based upon a GEANT [37] description that includes effects of time variation of the beam position and hardware configuration of the SVX II. This gives a relative efficiency,

$$\epsilon_{rel} = \frac{\epsilon_{J/\psi\pi}}{\epsilon_{J/\psi K}} = 0.991 \pm 0.005,$$

for reconstruction of the two decay modes.

Combining the raw ratio and the relative reconstruction efficiency, we determine the ratio of branching fractions as

$$\frac{\mathcal{B}(B^+ \rightarrow J/\psi\pi^+)}{\mathcal{B}(B^+ \rightarrow J/\psi K^+)} = 4.86 \pm 0.82(\text{stat.}).$$

# Chapter 5

## Systematics

The determination of the systematic uncertainty for the ratio of branching fractions is accomplished by estimating the systematic error of the four main sources. The following sections described the possible systematic uncertainties for each sources and estimate their magnitude.

### 5.1 Fitting Procedure

To test the fitting procedure we use toy MC data samples which are generated by following the PDF used in the likelihood fit. We have done two kinds of test. Figure 5.1 shows the pull distributions which are defined by  $(x_{fit} - x_{input})/\sigma$ . To make these distributions we test with 5000 toy MC samples, each of which has the same number of entry as data and is generated following values in Table 5.1. The pull distributions of each parameter have the mean values close to 0 and width close to 1. This mean the likelihood fitting returns unbiased results and well estimates the statistical uncertainties.

Input versus output test is shown in Figure 5.2. Varying the input ratio, 0.02, 0.05, 0.08, 0.15 and 0.3 with fixing other parameters, we compare the values returned by fit and the input ratios. Figure 5.2 shows the excellent agreement between them. So we estimate the systematic uncertainty caused by the fitting procedure is negligible.

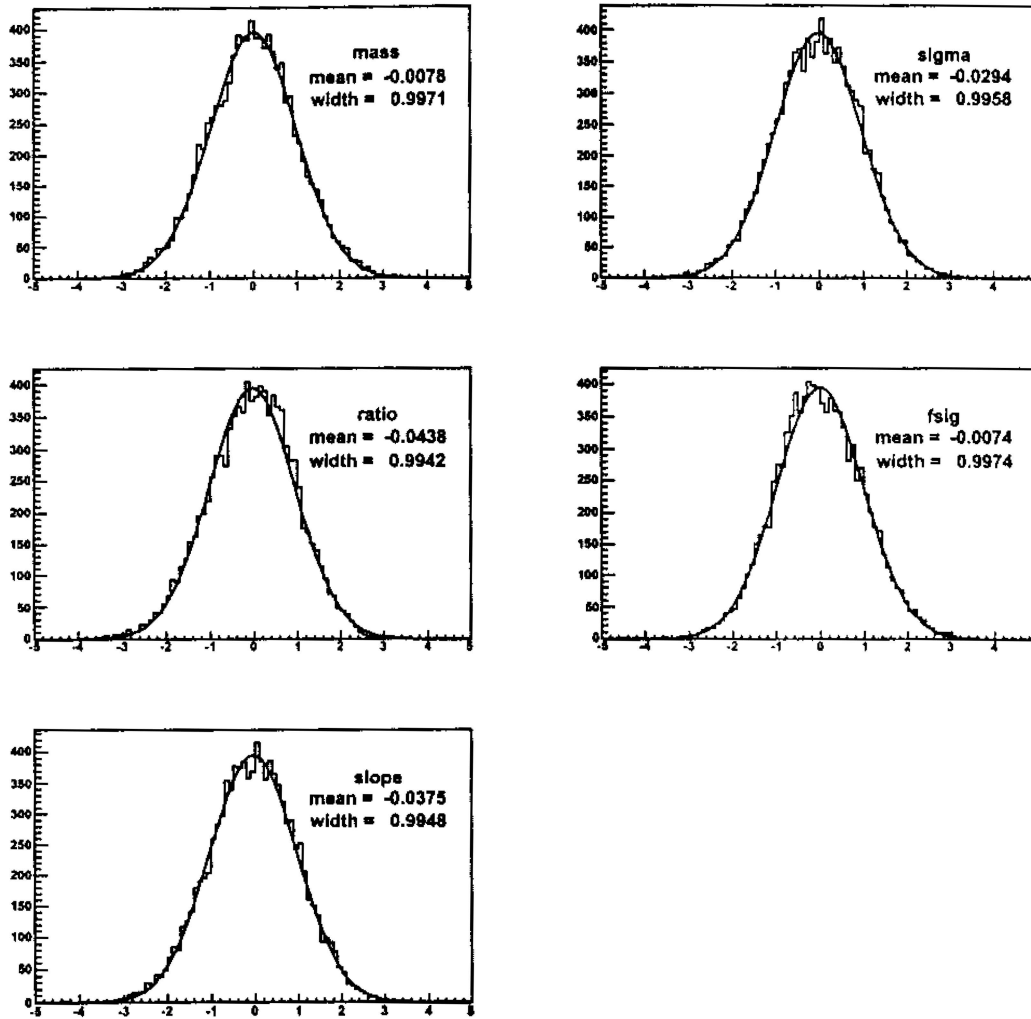


Figure 5.1: The pull distributions of each fitting parameter from the toy MC test.

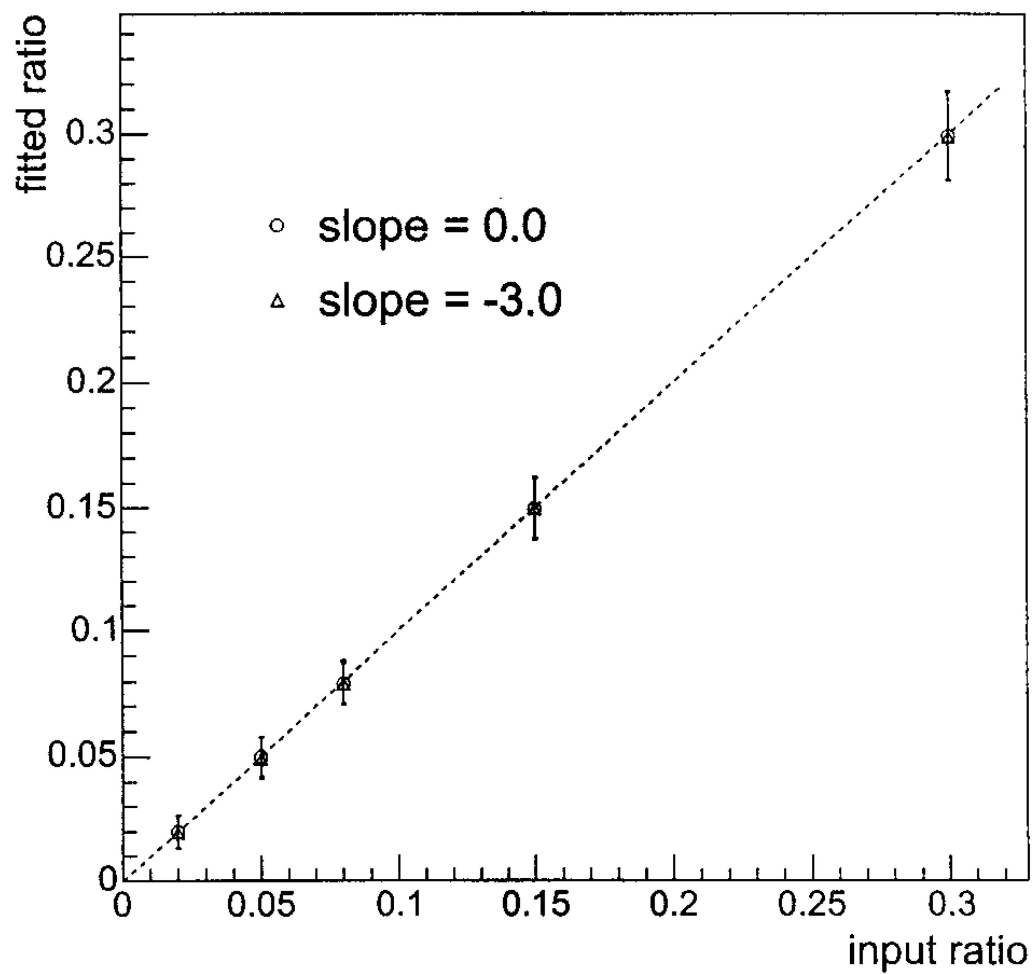


Figure 5.2: Fitted ratio versus input ratio from the toy MC test. The slope of dashed line is 1.

parameter	value
$M_{B^+}$	5.279
$\sigma$	1.3
$r$	0.02,0.05,0.08,0.15,0.3
$f_{sig}$	0.74
$s$	0.0, -3.0

Table 5.1: Input values for fitting test.

parameter	value
$M_{B^+}$	$5.2792 \pm 0.0003$
$\sigma$	$1.31 \pm 0.0003$
$r_{obs}$	$0.0494 \pm 0.0082$
$f_{sig}$	$0.736 \pm 0.012$
$s1$	$-76.8 \pm 39.7$
$s2$	$6.8 \pm 3.7$
$N(B^+ \rightarrow J/\psi K^+)$	$1880.7 \pm 33.6$
$N(B^+ \rightarrow J/\psi \pi^+)$	$92.9 \pm 14.7$

Table 5.2: The values of the fitted parameters that best represent the data with a 2<sup>nd</sup> polynomial background.

## 5.2 Background Model for Mass Distribution

One of possible source of systematic uncertainties is the modeling of the background shape. We refit using a 2<sup>nd</sup> order polynomial function as background instead of a 1<sup>st</sup> order. The new background term is

$$p_2(M_{\mu\mu K}) = s1 \cdot \left( M_{\mu\mu K}^2 - \frac{up^3 - ll^3}{3(up - ll)} \right) + s2 \cdot \left( M_{\mu\mu K} - \frac{up + ll}{2} \right) + \frac{1}{up - ll}, \quad (5.1)$$

where  $s1$  and  $s2$  are the coefficients of the polynomial function.

The result of the fit is shown in Table 5.2. The ratio of branching fractions differs by 2.5% of its values, so we give 2.5% to the systematic uncertainty from background model for mass distribution.

## 5.3 Fitting Range

The reflection of  $B^+ \rightarrow J/\psi\pi^+$  signals goes up to over  $5.4 \text{ GeV}/c^2$ , so we have less than 50% of all fitting range for combinatorial background sideband. To check the uncertainty from this, we vary higher fit range from 5.6 to 5.8. Table 5.3 shows the results of the fit. And we give 1.0% to the systematic uncertainty of fitting range.

fit range [ $\text{GeV}/c^2$ ]	fitted ratio
5.2 - 5.6	$0.0482 \pm 0.0081$
5.2 - 5.7	$0.0483 \pm 0.0081$
5.2 - 5.8	$0.0487 \pm 0.0080$

Table 5.3: The results of fitting the data for different fitting ranges

## 5.4 PDF's parameterization

The uncertainties on the fixed parameters of the PDF of the alpha distributions represent a source of systematic error on the raw ratio. We have varied each of these parameters by  $\pm 1\sigma$ , and have repeated the likelihood fit. For each PDF, the standard deviation of the new result with respect to the raw ratio is assumed as a contribution to the systematic uncertainty on the ratio of the branching fractions. The several contributions have been quadratically added to give the total systematic errors. Propagating these errors, we obtain a contribution of 1% to the systematic uncertainty on the ratio of branching fractions.

## 5.5 $\epsilon_{rel}$

In Ref. X, the nuclear interaction probabilities of the charged  $K$  and  $\pi$  are studied. The results of this study are shown in Table 5.4.

Using this numbers, we estimate the overall effect on the  $\epsilon_{rel}$  due to the nuclear interactions. Following Reference [38], we assume 25% of the overall

	$K^+$ (%)	$K^-$ (%)	$\pi^+$ (%)	$\pi^-$ (%)
Probabilty	$2.8 \pm 0.1$	$4.5 \pm 0.2$	$4.9 \pm 0.2$	$4.6 \pm 0.2$

Table 5.4: Probability of hadronic interaction on single kaons and pions.

effect as the systematic uncertainty associated to the material description and nuclear interactions. We then vary the relative efficiency by plus and minus the quantity determined in this way and take a half of the maximum variation as the final systematic uncertainty. We give 0.5% to the systematic uncertainty associated to  $\epsilon_{rel}$  using this procedure.

## 5.6 Systematics Summary

Table 5.5 summarizes individual systematic uncertainties and their overall value, and we take the overall systematic uncertainty as the quadrature sum of each contribution. We estimate the systematic uncertainty is 2.9% of the value.

Systematics source	value(%)
Fitting procedure	negligible
Background Model	2.5
Fitting Range	1.0
PDFs parameterization	1.0
$\epsilon_{rel}$	0.5
Total	2.9

Table 5.5: Systematic sources and their values.

# Chapter 6

## Conclusion

This thesis reports on the measurement of the ratio of branching fractions for the Cabibbo-suppressed decay mode  $B^+ \rightarrow J/\psi\pi^+$  to  $B^+ \rightarrow J/\psi K^+$ . This analysis is based on data collected at CDF from February 9, 2002 to September 6, 2003, for an equivalent integrated luminosity of  $220 \text{ pb}^{-1}$ .

The ratio of branching fractions,  $\mathcal{B}(B^+ \rightarrow J/\psi\pi^+)/\mathcal{B}(B^+ \rightarrow J/\psi K^+)$ , has been determined with an approach based on a maximum likelihood fit to a reconstructed sample of  $B^+ \rightarrow J/\psi K^+$  decays. A signal of  $90.8 \pm 14.6$   $B^+ \rightarrow J/\psi\pi^+$  events is observed, and the ratio is determined to be

$$\frac{\mathcal{B}(B^+ \rightarrow J/\psi\pi^+)}{\mathcal{B}(B^+ \rightarrow J/\psi K^+)} = 4.86 \pm 0.82(\text{stat.}) \pm 0.14(\text{syst.})\%,$$

which is in agreement with previous measurements and with theoretical expectations.

This analysis supersedes the result of CDF Run I, which was measured using a mathematically wrong likelihood.

The measurement reported here is affected by a systematic uncertainty which is much smaller than the statistical uncertainty, therefore new data being accumulated by CDF will allow further improvement.



# Bibliography

- [1] K.G. Wilson. Phys. Rev., 179 (1969) 1449.
- [2] J.D. Bjorken, in: *New Developments in High Energy Physics*, edited by E.G. Floratos and A. Verganelakis, Nucl. Phys. B Proc. Suppl., 11 (1989) 325.
- [3] M. Neubert, Phys. Rep., 245 (1994) 259.
- [4] N. Isgur and M.B. Wise, Phys. Lett. B, 232 (1989) 113.
- [5] N. Isgur and M.B. Wise, Phys. Lett. B, 237 (1990) 527.
- [6] CDF Collaboration, T. Affolder *et al.*, Phys. Rev. Lett., 85 (2000) 4668.
- [7] BABAR Collaboration, B. Aubert *et al.*, submitted to Phys. Rev. Lett., hep-ex/0107049
- [8] M. Bauer, B. Stech and M. Wirbel, Z. Phys. C, 29 (1985) 637.
- [9] M. Bauer, B. Stech and M. Wirbel. Z. Phys. C, 34 (1987) 103.
- [10] M. Neubert and B. Stech, in: *Heavy Flavours II*, World Scientific, eds. A.J. Buras and M. Linder, hep-ph/9705292.
- [11] Ciuchini *et al.* Eur. Phys. Jour C, 9 (1999) 43
- [12] I. Dunietz, Phys. Lett. B, 316 (1993) 561.
- [13] F. Bedeschi *et al.*, NIM A268, 50-74 (1988)

- [14] W.M Yao and K. Bloom, CDF Note 5591 (2000)
- [15] G. Ascoli *et al.*, NIM **A28**, 63-67 (1988)
- [16] G. Ascoli *et al.*, CDF Note 2858 (1994)
- [17] The CDF Collaboration, FERMILAB-Pub-96/390-E (1996)
- [18] L. Balka *et al.*, Nucl. Instr. & Meth. **A267**, 272 (1988)
- [19] F. Abe *et al.*, Phys. Rev. **D50**, 5550 (1994)  
N. Amos *et al.*, Phys. Rev. Lett. **68**, 2433 (1992)  
C. Avila *et al.*, Phys. Lett. **B445**, 419 (1999)
- [20] S. Klimenko *et al.*, CDF Note 4330 (1998)  
S. Klimenko *et al.*, CDF Note 5119 (1999)  
D. Acosta *et al.*, CDF Note 6052 (2002)
- [21] H. Frisch *et al.*, CDF Note 2038 (1994)
- [22] CDF Collaboration *et al.*, CDF Note 4718 (2001)
- [23] E. Thomson *et al.*, IEEE Transaction on Nuclear Science, Vol. 49, No. 3 (2002)
- [24] L. Holloway and J. strologas, CDF Note 4146 (1997)
- [25] K. Anikeev *et al.*, CDF Note 5793 (2001)
- [26] M. Paulini and B. Wickund, CDF Note 5483 (2000)  
K. Anikeev *et al.*, CDF Note 5796 (2002)  
M. Bishai *et al.*, CDF Note 6004 (2002)
- [27] D. Acosta *et al.*, The CDF Collaboration, Phys. Rev. **D71**, 032001 (2005)
- [28] K. Anikeev *et al.*, CDF Note 5958 (2002);  
G. Bauer, A. Korn and C. Paus, CDF Note 6335 (2003)
- [29] M. Campanelli and E. Gerchtein, CDF Note 6905 (2004)

- [30] L. Vacavant, CDF Note 5852 (2002)
- [31] S. Eidelman *et al.*, Phys. Lett. **B592**, 1 (2004).
- [32] J. Marriner, CDF Note 1996 (1993)
- [33] Saverio D'Auria, *et al.*, CDF Note 6932 (2004)
- [34] D. Acosta *et al.*, The CDF Collaboration, FERMILAB-PUB-05-316-E.  
Submitted to Phys. Rev. Lett. July 13, 2005.
- [35] P. Nason, S. Dawson and R. K. Ellis, Nucl. Phys. **B303**, 607 (1998)
- [36] C. Peterson, *et al.*, Phys. Rev. **D27**, 105 (1983)
- [37] R. Brun, *et al.*, CERN-DD-78-2-REV and CERN-DD-78-2
- [38] S. Giagu *et al.*, CDF Note 6391 (2003)

# 초 록

## CDF 실험에서의 $B(B^+ \rightarrow J/\psi\pi^+)/B(B^+ \rightarrow J/\psi K^+)$ 의 측정

이 재 승

성균관대학교 물리학과

본 논문에서는  $B^+ \rightarrow J/\psi\pi^+$ 와  $B^+ \rightarrow J/\psi K^+$ 의 갈래비의 비를 측정하였다. 본 연구에서 사용된 데이터는  $220 \text{ pb}^{-1}$ 의 크기로 2002년 2월부터 2003년 8월까지 질량중심에너지가  $\sqrt{s} = 1.96 \text{ TeV}$ 인  $p\bar{p}$  충돌로부터 CDF에 의하여 수집되었다. 두 붕괴방식들의 갈래비의 비는

$$\frac{B(B^+ \rightarrow J/\psi\pi^+)}{B(B^+ \rightarrow J/\psi K^+)} = 4.86 \pm 0.82(\text{stat.}) \pm 0.14(\text{syst.})\%$$

로 측정되었다.